DEVELOPMENT OF CARBON NANOTUBES WITH A DIAMOND INTERLAYER FOR FIELD ELECTRON EMISSION AND HEAT TRANSFER APPLICATIONS

A Thesis Submitted to the College of

Graduate Studies and Research

In Partial Fulfillment of the Requirements

For the Degree of Doctor of Philosophy

In the Department of Mechanical Engineering

University of Saskatchewan

Saskatoon

By

LEZHI YANG

PERMISSION TO USE

In presenting this thesis in partial fulfilment of the requirements for a Postgraduate degree from the University of Saskatchewan, I agree that the Libraries of this University may make it freely available for inspection. I further agree that permission for copying of this thesis in any manner, in whole or in part, for scholarly purposes may be granted by the professor Q. Yang, who supervised my thesis work or, in her absence, by the Head of the Department or the Dean of the College in which my thesis work was done. It is understood that any copying or publication or use of this thesis or parts thereof for financial gain shall not be allowed without my written permission. It is also understood that due recognition shall be given to me and to the University of Saskatchewan in any scholarly use which may be made of any material in my thesis.

Requests for permission to copy or to make other use of material in this thesis in whole or part should be addressed to:

Head of the Department of Mechanical Engineering

57 Campus Drive

University of Saskatchewan

Saskatoon, Saskatchewan, Canada

S7N 5A9

ABSTRACT

Carbon Nanotubes (CNTs) have great potentials for Field Electron Emission (FEE) and Flow Boiling Heat Transfer (FBHT) applications. However, their weak adhesion on metallic substrates limits the development of CNTs in both applications. Diamond has high thermal conductivity and develops strong bonding with CNTs. The development of a diamond interlayer between CNTs and substrates is a feasible approach to address the adhesion problems. The purpose of this research was to develop a new CNT-based materials with a diamond interlayer for FEE and FBHT applications by focusing on four objectives: (1) enhancement of diamond thin film adhesion on a Cu substrate, (2) improvement of the CNT FEE stability, (3) reduction of the CNT FEE turn-on field, and (4) investigation of the FBHT performance of CNT based structures.

The CNTs and diamond thin films in this thesis were prepared by Microwave Plasma enhanced Chemical Vapor Deposition (MPCVD) and Hot Filament enhanced Chemical Vapor Deposition (HFCVD). The structure and chemical states of the diamond films and CNTs were characterized by Scanning Electron Microscopy (SEM), cross-sectional Transmission Electron Microscopy (TEM), X-Ray Diffraction (XRD), Raman spectroscopy, synchrotron based X-ray Absorption Spectroscopy (XAS). To deposit diamond thin films on a Cu substrate with sufficient adhesion strength, a sandblasting pretreatment and alloying with a tiny amount of Al were investigated. The adhesion of diamond thin films to substrates was evaluated by Vickers micro-hardness indentation. The FEE stability and turn-on field were measured by a Keithley 237 high voltage measuring unit. The FBHT property of the structures was tested repeatedly at different flow velocities to explore the dependence of heat transfer performance on certain parameters, including the flow patterns, Critical Heat Flux (CHF), and stability.

The results show that sandblasting pretreatment increases the surface roughness and surface defect density, thereby increasing diamond nucleation density and adhesion to the Cu substrate. Al alloying appears to inhibit the formation of graphite at the interface between

diamond and the Cu substrate, which improves the chemical bonding between diamond and the Cu substrate and increases the adhesion strength between them.

The FEE testing results show that ultra-high FEE stability (more than 5000 minutes) was achieved for the CNTs with a diamond interlayer. This is attributed to the good contact at the diamond-CNT and diamond-substrate interfaces. The main factors that affect the CNT FEE turn-on field were also studied. By optimizing the structure, an FEE turn-on field of 5.1 V/μm was achieved and an emission barrier model for CNTs with a diamond interlayer on Cu substrate was used to explain the results. FBHT testing was done on CNTs with different structures and the results show that high heat transfer efficiency can be achieved on CNTs with a diamond interlayer at low mass fluxes.

ACKNOWLEDGEMENTS

This work is sponsored by the Canada Research Chair program, the Natural Sciences and Engineering Research Council of Canada, and China Scholarship Council.

I owe my deepest gratitude to my supervisor Prof. Qiaoqin Yang for her patient guidance and invaluable support during my Ph.D. study. She gave me enormous freedom and trust, which afforded me to be creative in my research. She led me in the right direction when I was confused and hesitating.

I would like to express my gratitude to advisory committee members Prof. Akria Hirose, Prof. Jerzy A. Szpunar, and Prof. Ikechukwuka N. Oguocha for their invaluable support and suggestions in my research and thesis.

I am also grateful to Dr. Yuanshi Li for his assistance in my research and discussion about my thesis. Special thanks is given to Dr. Haidong Wang for his great help with my thesis revisions. I would also like to thank all my colleagues — Chunzi Zhang, Linlin Zhang, Yu Sun, Yongji Tang, Hamid Niakan, Sujith C. S. Kumar, Xiaoyu Sun, Boqian Wan, Fan Ye and others — for helping me in my research work. I would also like to thank Mr. Rob Peace and Nanfang Zhao from the materials lab helping me with the equipment as well as Mr. Jason Maley and Mr. Guosheng Liu for their assistance with Raman spectroscopy and TEM.

I must give special thanks to David McColl, and other colleagues in the Plasma Physics Lab, for their assistance with my experiments.

Finally, I would like to thank my mother for her unconditional support, my beloved wife for her endless love, and all my family for their love and support during my Ph.D. studies.

DEDICATION

To my parents and my wife Longmei Wu

TABLE OF CONTENTS

page

LIST OF TABLES

Table page

LIST OF FIGURES

Figure page

LIST OF ABBREVIATIONS

Abbreviation page

CHAPTER 1

INTRODUCTION

1.1 Overview

Diamond and carbon nanotubes (CNTs) are two different allotropes of carbon. They both exhibit many outstanding physical and chemical characteristics and are promising for a wide range of applications including Field Electron Emission (FEE) and heat transfer [1-10]. Due to its high electrical and thermal conductivity and relatively low cost, copper (Cu) is a choice substrate material to support diamond films and CNTs for FEE and heat transfer applications. However, both diamond and CNTs have poor adhesion to Cu substrates, which represents one of main obstacles for their application.

The major contributor to the poor adherence of diamond films to a Cu substrate is the low affinity of diamond to Cu. Also, there is a considerable coefficients thermal expansion (CTE) mismatch between Cu and diamond. The low affinity, coupled with high interfacial stress induced by the large difference in CTE, makes diamond easily delaminate from Cu substrates during cooling after deposition [11]. A survey of the open literature indicates there is not much information about effective methods to obtain adequate adhesion of diamond films to Cu substrates for FEE and heat transfer applications.

The weak adhesion between CNTs and Cu substrates affects FEE and heat transfer performance of CNTs [12]. It increases interfacial thermal and electrical resistance, which causes heat accumulation at the interface that damages the CNTs and thus decreases their FEE stability [13]. It also decreases the heat transfer efficiency of CNTs in Flow Boiling Heat Transfer (FBHT) applications [14]. To enhance the adhesion of CNTs on substrates, different methods including introduction of interlayers have been investigated [14, 15]. Nevertheless, the enhancement of interfacial adhesion obtained from these studies is still insufficient for FEE and FBHT applications. Therefore, it is important to develop new approaches to enhancing the adhesion of both diamond and CNTs on a Cu substrate.

It is still a challenging task to manipulate the structures of CNTs and diamond to achieve high FEE and heat transfer performance. Previous research has demonstrated that the density

of CNTs is an important factor affecting FEE emission current: low density results in weak emission current due to the lack of effective emitters whereas excessive high density reduces emission current due to a "screen effect" [16]. Equally, the density of CNTs also influences the heat transfer efficiency of CNT arrays. Therefore, it is important to develop an efficient method to control the density of CNTs to achieve high FEE emission current and high heat transfer efficiency. In addition, diamond thin films usually contain a small amount of graphitic (sp^2) carbon at the grain boundaries. The sp^2 carbon plays a key role in electron transport in diamond films. A conduction channel mechanism has been proposed to explain electron transport in diamond films [17]. The mechanism shows that high sp^2 concentration in diamond thin films enhances conduction channels and thus improves the conductivity of diamond thin films. However, it is still unknown how the concentration of sp^2 carbon in diamond thin films affects FEE properties.

1.2 Research Objectives

As mentioned previously, both diamond and CNTs have great potential for use as efficient FEE emitters and heat sinks. However, their poor adhesion to Cu substrates significantly limits their use in these applications. Although some progress has been made to enhance adhesion, the problem still remains unsolved. Therefore, the overall objective of this thesis is to develop novel approaches to solve the adhesion problem in order to significantly improve the FEE and heat transfer performance of CNTs on Cu. Specifically, the research has following objectives:

(1) Develop techniques for depositing diamond films on Cu substrates with high adhesion strength and to understand the adhesion enhancement mechanisms;

(2) Develop CNTs with a diamond thin film interlayer to improve the FEE stability of CNTs;

(3) Optimization of the structure of diamond thin films and CNTs on Cu substrates to achieve superior FEE performance and understand the relationship between the structure and properties of the emitters;

(4) Develop CNTs with a diamond thin film interlayer on Cu substrates to achieve very efficient FBHT.

1.3 Research Contributions

The major contributions of this thesis are as follows:

Two approaches have been developed to enhance diamond film adhesion to Cu substrates and the adhesion enhancement mechanism has been investigated systematically. The results show that the adhesion has been significantly improved for both approaches.

A new approach using CNTs with diamond interlayer material has been developed to improve the FEE stability of CNTs. Microstructural observations show good adhesion between diamond thin films and CNTs due to the formation of direct C-C bonding at the interface.

The factors affecting the FEE performance of the CNTs with a diamond interlayer have been investigated. By controlling the catalyst spinning time, the density of CNTs can be well-controlled to achieve the appropriate density and exhibit a low FEE turn-on field. By increasing the sp^2 carbon concentration in diamond thin films, the FEE turn-on field is further decreased. The FEE emission barrier of CNTs with a diamond interlayer on Cu substrates has been investigated. It shows that electrons emitted from CNTs need to transport through two barriers: The first barrier is between CNTs and substrates and the second one is between CNTs and vacuum.

The FBHT properties of CNTs with a diamond interlayer on Cu substrates have been studied. High heat transfer efficiency has been achieved on CNTs with a diamond interlayer on Cu substrates at low mass flux.

1.4 Organization of the Thesis

This thesis consists of seven chapters. The organization is as follows:

Chapter one gives a brief introduction and the motivation for the research. The objectives, contributions, and organization of the thesis are also defined in this chapter.

Chapter two presents a literature review of diamond, CNTs, and their hybrid materials. Fundamental knowledge of FEE is also provided.

Chapter three gives the experimental details for treatment of substrates and synthesis of diamond thin films and CNTs. The techniques used for characterization of the various structures are described. The device built up for heat transfer is also introduced. Furthermore, the details of FEE and FBHT measurement are presented.

Chapter four reports the enhancement of diamond thin film adhesion on Cu substrates by using sandblasting and Al alloying techniques. Fundamental adhesion enhancement mechanisms are also discussed.

Chapter five presents the FEE stability testing results of CNTs with a diamond interlayer and gives a discussion of the effect of CNT density, substrate material, and sp^2 carbon content in diamond thin films on CNT FEE performance.

Chapter six reports the FBHT testing results of CNTs with a diamond interlayer on Cu substrates. FBHT enhancement mechanisms are also discussed.

The final chapter summarizes and concludes the main results of the thesis and gives recommendations for future work.

CHAPTER 2

LITERATURE REVIEW

In this chapter, the structure, properties, synthesis, and applications of diamond, CNTs, and their hybrids are being introduced. The fundamental knowledge of FEE and its applications are being reviewed. The techniques used for characterizing diamond, CNTs, and their hybrids are also being reviewed.

2.1 Carbon Materials

Carbon is the fifteenth most abundant element in the Earth's crust and is important due to it is the main constituent of organic compounds. All life on earth is based on carbon, and so far it has been found in all living creatures including human beings, and so is closely associated with our daily life.

Carbon is the sixth element in the periodic table, and has six protons and six neutrons in its core and six electrons surrounding the nucleus. At ground state, the electronic structure is $1s^2 2s^2 2p^2$. The two inner electrons cannot form bonds while the four valance electrons in 2s and 2p orbitals can form 4 bonds with other atoms. The 2s orbital and 2p orbitals are usually hybridized to form sp^3, sp^2, or sp hybrids. Figure 2.1 is a schematic of sp^3, sp^2, and sp hybrid formation. In sp^3 hybridization, the s orbital is hybridized with the three p orbitals to form four sp orbitals arranged in a tetrahedral geometry with bond angles of $109°18'$. In sp^2 hybridization, the s orbital is hybridized with two of the three p orbitals to form three sp orbitals arranged in a plane with bond angles of $120°$. In sp hybridization, the s orbital is hybridized with one of the three p orbitals to form two sp orbitals arranged in a linear form with bond angles of $180°$ [18]. All sp^3, sp^2, and sp orbitals form σ bonds while the unhybridized p orbitals form π bonds with other atoms.

Pure carbon as a solid material has three allotropes: diamond, graphite, and amorphous carbon. Their physical and chemical properties vary significantly due to different bonding states and/or crystal structures. Diamond consists of sp^3 bonded carbon and has a tetrahedral crystal structure. Graphite consists of sp^2 bonded carbon and has a hexagonal crystal structure.

Amorphous carbon consists of a mixture of sp, sp^2, and sp^3 bonds and has no crystalline structure. Carbon nanotubes, which have a cylindrical nanostructure, belong to graphite family. In this chapter, the fundamentals of diamond and CNTs and their applications in FEE and FBHT will be discussed in detail.

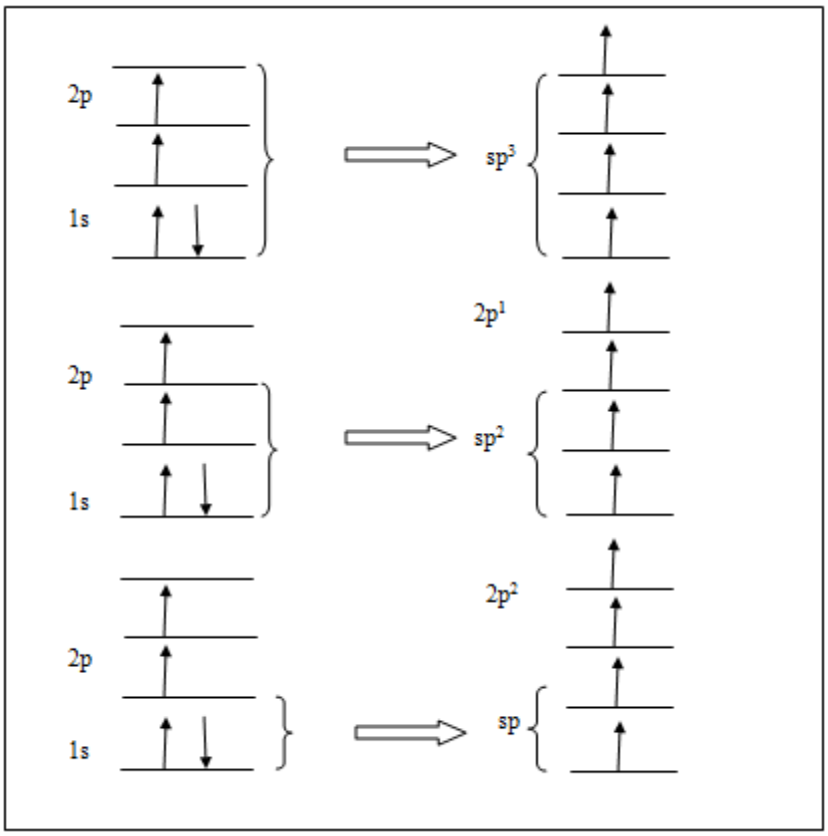

Figure 2.1. Schematic of sp^3, sp^2, and sp hybridization.

2.2 Diamond

2.2.1 Structure and Properties

Among all known natural materials, diamond has the highest hardness, highest room temperature thermal conductivity, and smallest thermal expansion coefficient. It also has many other superior properties such as a wide band gap, chemical stability, and high transparency for a wide range of wavelengths. Table 2.1 lists the physical properties of diamond. Due to its unique properties, diamond has been broadly used in cutting tools,

optical devices, thermal management, and electron beam devices [19]. The outstanding properties of diamond are attributed to its unique structure. In the structure of diamond, as shown in Figure 2.2, each carbon atom is in an sp^3 hybrid bonding state linked to four neighboring carbon atoms to form a coordinated tetrahedral structure with strong σ bonds (bond length 0.154 nm). The lattice structure is rigid and stable with high atom density, which gives diamond ultra-high hardness and chemical stability. The covalent bond between each atom in the diamond lattice makes diamond a natural insulator and hydrophobic.

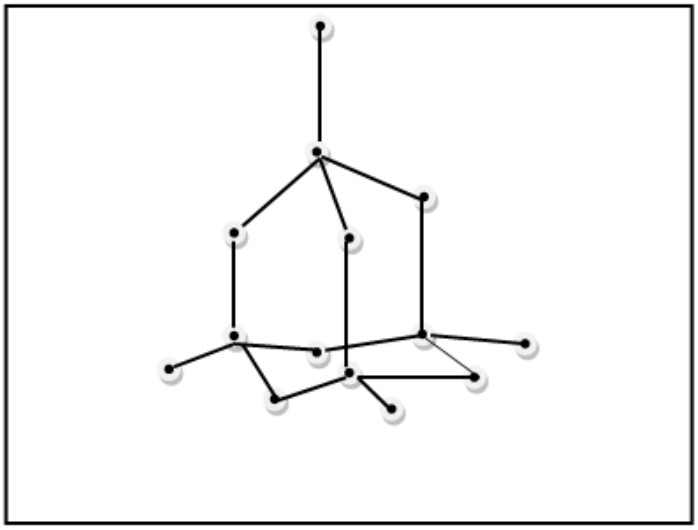

Figure 2.2. Structure of diamond lattice.

Table 2.1. The properties of diamond [20].

Property	Value	Units
Hardness	10,000	kg/mm^2
Strength, tensile	>1.2	GPa
Strength, compressive	>110	GPa
Sound velocity	18,000	m/s
Density	3.52	g/cm^3
Young's modulus	1220	GPa
Poisson's ratio	0.2	Dimensionless
Thermal expansion coefficient	0.0000011	/K
Thermal conductivity	20.0	W/cm-K
Thermal shock parameter	30,000,000	W/m
Debye temperature	2,200	K
Optical index of refraction(at 591nm)	2.41	Dimensionless
Optical transmissivity (from nm to far IR)	225	Dimensionless
Loss tangent at 40 Hz	0.0006	Dimensionless
Dielectric constant	5.7	Dimensionless
Dielectric strength	10,000,000	V/cm
Electron mobility	2,200	$cm^2/V\text{-}s$
Hole mobility	1,600	$cm^2/V\text{-}s$
Electron saturated velocity	27,000,000	cm/s
Hole saturated velocity	10,000,000	cm/s
Work function	small and negative	On (111) surface
Band gap	5.45	eV
Resistivity	10^{13}-10^{16}	Ohm-cm

2.2.2 Synthesis of Diamond Thin Films

The first diamond synthesis method was developed in the 18th century using high-pressure and high-temperature techniques [21]. This method produces small diamond particles that are not suitable for many applications.

Synthesis of diamond at a reasonable rate by chemical vapor deposition (CVD) was developed in the early 1980s and has become a widely used method for synthesizing diamond thin films [22]. Using the CVD method, diamond thin films can be deposited on a substrate with controlled structure and morphology to achieve desirable tribological and electronic properties. The CVD growth process is shown in Figure 2.3. H_2 gas is decomposed into atomic hydrogen (H) in a thermal or plasma CVD reactor under a vacuum environment. Next, the precursor gas (for example, methane (CH_4)) is decomposed into hydrocarbon radicals due to the attack of atomic hydrogen. The radicals are then transported to the substrate surface and deposited as diamond or other forms of carbon. Only diamond is stable in this atomic H rich environment, and the atomic H acts as an etchant to remove non-diamond carbon. Therefore, only pure diamond remains and grows. The most common CVD techniques for diamond deposition are Microwave Plasma CVD (MPCVD) and Hot Filament CVD (HFCVD). The details of diamond deposition by these two techniques are discussed in the following sections.

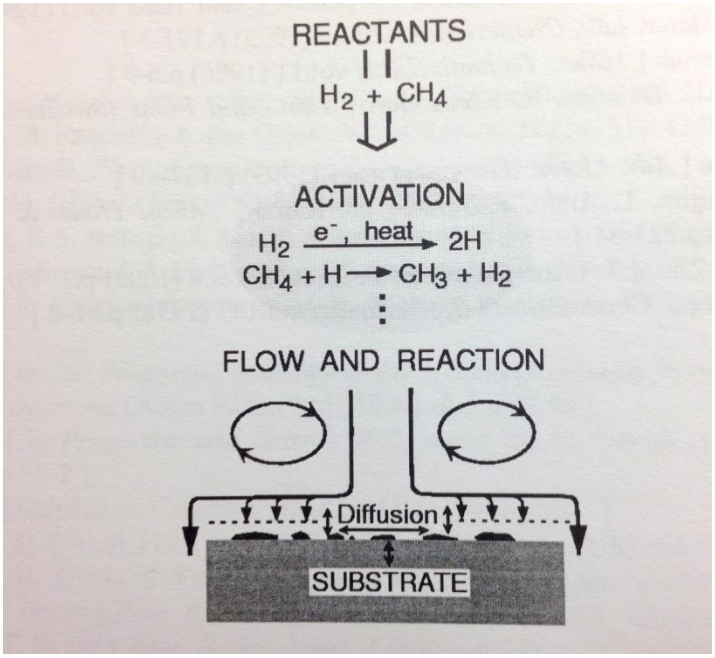

Figure 2.3. Schematic of the general process for the CVD of diamond [23].

2.2.2.1 MPCVD

MPCVD uses a microwave plasma to decompose and activate precursor gases for diamond deposition. The microwave supplies energy to generate the plasma by inciting collisions between gas molecules. The benefit of using microwave plasma is that it used plasma instead of high temperatures to decompose and activate the precursor gases, which allows for a lower reaction temperature at the substrate and prevents contamination from the evaporation of other materials. Figure 2.4 is a schematic of an MPCVD reactor. For diamond deposition, the chamber is pumped to vacuum and filled with precursor gases. The gas flow rate is controlled by the Mass Flow Controller (MFC). Then, microwave power is produced at the generator and coupled into the chamber through the quartz window. The precursor gas is stimulated by the microwave and forms a plasma ball.

MPCVD for diamond growth was first reported in 1983 by Kamo *et al*. [24]. Since then, more MPCVD reactors have been designed for diamond growth with the common types of bell jar, disc, and jet torch [25]. In 1987, ASTeX invented a “bell jar” system to overcome the contamination problem. In this system, a silica bell jar is designed to confine the plasma discharge. Later, they improved the bell jar design with a silica microwave window. The

plasma generated is confined between the substrate holder and the silica window. The ASTeX system has a diamond deposition rate of 10 μm/h over a 20 cm diameter substrate with a mass deposition rate of 1 g/h. From 1986 to 1995, Wavemat Inc. and Michigan State University developed an inside coupling cavity disc reactor. In this reactor, a large cavity (45 cm diameter) and substrate holder (up to 33 cm diameter) was developed for larger area diamond deposition. In late 1980s, Mitsuda developed a jet torch reactor with a low gas pressure and low diamond deposition temperature. At low pressure, the plasma heating of the substrate is reduced and hence the substrate temperature decreases. Some advantages associated with using MPCVD include high quality and low deposition temperature. MPCVD has high energy efficiency and much lower deposition temperature than HFCVD (discussed below). It has been reported that diamond thin films can be synthesized at a low temperature of 250 ℃ by MPCVD [26]. In addition, MPCVD has the potential for scaled-up diamond deposition. The major problem is the heterogeneous diamond growth rate caused by the shape of the plasma ball. The uneven shape of the plasma ball also induces residual stresses in the diamond thin films, causing adhesion problems between the diamond films and substrates.

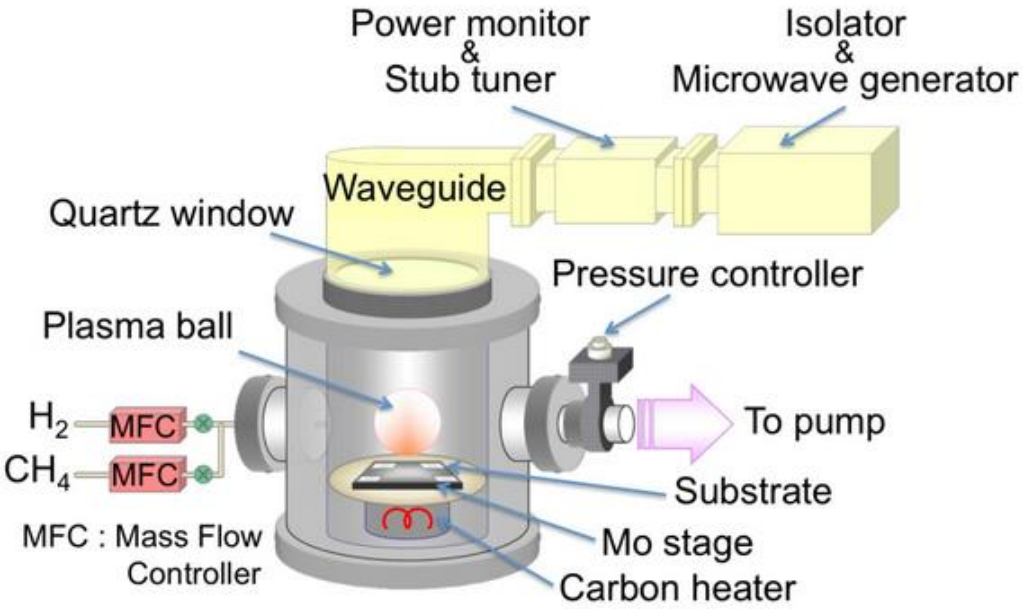

Figure 2.4. Schematic of an MPCVD reactor [27].

2.2.2.2 HFCVD

HFCVD for diamond deposition was first reported by Matsumoto and Tsutsumi in 1982 [28]. In this system, they chose a Tungsten filament over a flow tube to decompose precursors. The substrate in this equipment was heated by the filament and a heater.

An HFCVD system is similar to a light bulb that has a refractory filament in a vacuum environment. Figure 2.5 is a schematic of an HFCVD reactor. A filament (usually tungsten wire) is set above the substrate. The temperature of the filament usually reaches 2000 K or higher to decompose and activate the precursor gases for diamond growth. The operation pressure is usually dozens of Torrs. At such a high temperature, hydrogen gas (H_2) dissociates into atomic species that can interact with hydrocarbon. This reaction provides carbon species for diamond growth. The filament can also heat the substrate and provide the required temperature for diamond growth. To enhance the diamond nucleation density and growth rate, some attachments such as electrical bias can be set up in the system. It has been found that bias can force carbon ions to move to the substrate and create a carbon-rich layer for diamond nucleation. The advantages of HFCVD for diamond deposition are that the reactor is relatively simple, cheap, easy to set up, and suitable for the large scale production of diamond. So far, HFCVD has been the most popular method in industry for diamond thin film production. The major problem of HFCVD for diamond synthesis is with respect to the filament. The evaporation of the filament reduces its lifetime, makes the growth conditions change during deposition, and affects the quality of the diamond produced. Another filament problem is that, after a long reaction time, the filament will be carbonized by the hydro-carbide gas, forming a metallic carbide, becoming brittle with high electrical resistivity, and resulting in unstable diamond growth conditions.

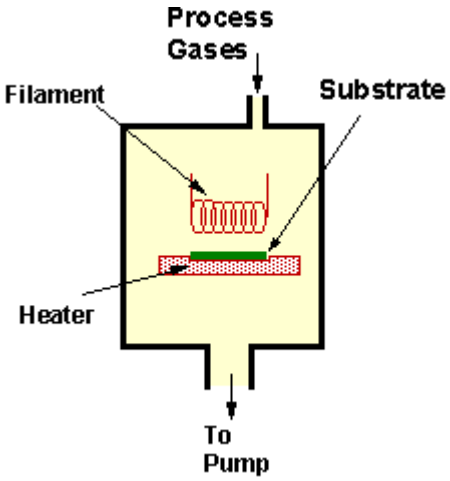

Figure 2.5. Schematic of an HFCVD reactor [29].

2.2.3 Adhesion of Diamond Thin Films

Adhesion is the interfacial force adhering two surfaces together. The adhering force can be a physical and/or chemical bonding force or a mechanical interlocking force [30]. In a coating system, adhesion is closely related to the physical and chemical properties of the film and substrate materials, the surface state of the substrate, and the deposition conditions. Good adhesion is necessary for diamond thin films to prevent it peeling off or failure in practical applications.

2.2.3.1 Adhesion measurement

Adhesion strength measurement can be conducted by destructive or nondestructive methods. Nondestructive methods use thermography, ultrasonics, acoustic emission, and laser shearography techniques to detect the adhesion strength indirectly [31]. Destructive methods apply force to the coatings and observe the damage caused by the force, and include pull-off testing, scratch testing, and indentation testing [32].

Pull-off testing is a qualitative method to measure the adhesion strength of diamond thin films. This method uses a loading fixture attached to the coatings and measures the load force required to pull off the coatings. Pull-off testing is simple, straightforward, and can be used to test any coatings, either brittle or flexible. However, it is limited to measurement of thin films with weak adhesion because the adhesion strength of the glues is usually lower than 90 MPa

[32]. Furthermore, the nonuniformity of film thickness, film quality, and film cohesion can affect the accuracy of the measurement.

Scratch testing is widely used for measuring the adhesion of hard coatings on hard substrates [32]. In scratch testing, a tip is drawn across the coating surface and the critical load to detach the coating is measured. Scratch testing equipment can be attached with microscopes, acoustic spectrometers, and surface-profiling equipment and is capable of measuring the adhesion combined with surface topography and mechanical properties of the samples. The testing process is simple but the tips are easily damaged by the high hardness of diamond.

The indentation method is usually applied to hard refractory coatings [32]. In indentation testing, a tip is pressed into the coating's surface. The adhesion of the coatings can be evaluated by observing the indentation marks. Rockwell and Vickers indentation are commonly used indentation methods for testing the adhesion of diamond thin films [32]. The advantages of indentation testing are that it is suitable for a wide range of materials, the testing process is simple, it can qualitatively measure the adhesion of the coatings, and the equipment is commercially available.

2.2.3.2 Adhesion of diamond thin films on Cu substrates

Cu is an ideal substrate material for diamond thin film applications in micro-electronics, heat transfer, and electrochemistry due to its high thermal and electrical conductivity. However, diamond thin films on Cu substrates always suffer an adhesion failure due to a thermal expansion mismatch, and a low affinity between diamond and Cu, and low diamond nucleation density on Cu.

In CVD diamond growth, high deposition temperature on the substrates is required [33]. When the deposited diamond thin films are cooled down to room temperature, the substrates will shrink substantially while the deposited diamond thin films will maintain almost the same dimensions. This is due to diamond's extremely low thermal expansion coefficient (1.1×10^{-7}/K at room temperature) while the substrate generally has a much higher thermal expansion coefficient. High thermal stress will be generated from this mismatch, which can

lead to delamination of the deposited diamond films from the substrates. This problem is particularly evident on Cu substrates due to the large thermal expansion coefficient of Cu (1.7×10^{-5}/K at room temperature).

Diamond thin films deposited on carbide-forming-metals such as tungsten, titanium, and molybdenum usually have relatively high adhesion due to the formation of a carbide interlayer between the diamond thin film and the substrate [34, 35]. However, Cu has a low affinity to diamond and cannot form any chemical bonds with diamond. In addition, Diamond nucleation density also affects the adhesion [35]. Higher nucleation density results in fewer voids and larger contact area between the thin film and the substrate, and thus higher adhesion. Nevertheless, the nucleation density of diamond on Cu is usually low because of the preferred formation of graphitic carbon.

2.2.3.3 Improvement of adhesion of diamond thin films on Cu substrates

As discussed in §2.2.3.2, diamond thin films have poor adhesion to Cu substrates and the films usually peel off after cooling down to room temperature. Therefore, it is necessary to enhance the adhesion for practical applications. There are three ways to increase the adhesion strength of diamond thin films on substrates: enhancing the diamond nucleation density, optimizing the diamond thin film deposition parameters, and modifying the surface state of the substrates [36].

When diamond thin films have low nucleation density on substrates, voids will be formed at the interface [35]. These voids will lead to the formation of cracks or peeling of the diamond thin films. To eliminate the voids, surface pretreatment and electric biasing methods for enhancing diamond nucleation have been attempted and successfully enhanced diamond thin film adhesion on carbide-form-metal substrates [37, 38]. However, these methods do not work well on Cu substrates due to the preferred graphite phase formed between the diamond thin films and the Cu substrate [39]. The graphite phase has weak adhesion to both the diamond thin film and the Cu substrate, which decreases the adhesion strength between them.

Diamond deposition parameters have also been investigated to enhance diamond thin film adhesion on metallic substrates. It is believed that, among all deposition parameters, the

deposition temperature affects diamond thin film adhesion on metallic substrates to the greatest extent [40]. A low deposition temperature reduces the thermal expansion mismatch between the diamond thin films and substrates, which decreases the interfacial thermal stress. A good example is that the low power used for MPCVD deposition to maintain a low substrate temperature can enhance diamond adhesion on a Ti substrate [40]. This method might not be as effective for Cu substrates due to the enormous thermal expansion difference between diamond and Cu. Even if deposited at a low temperature, diamond thin films could not have enough adhesion strength and may peel off from the Cu substrates.

Other efforts have been made to modify the surface state of substrates, including deposition of an interlayer, alloying substrates with aluminum (Al), and substrate surface modification [36, 41-44]. The interlayer method adopts a thin layer at the interface that has good adhesion to both the diamond thin film and the substrate. But this layer can induce an interface barrier that increases the total thermal and electrical resistance, so it is not ideal for heat transfer or FEE applications. Alloying is a technique which can modify the physical or chemical properties of the metals by adding other elements. Adding Al into Fe based alloys has been found to be able to enhance the adhesion of diamond thin films significantly [43, 44]. The mechanism for this enhancement is that a tiny amount of Al in the substrate can prohibit the formation of the graphite phase, thus enhancing nucleation and adhesion of diamond on Fe-based substrates. This mechanism may also work well with Cu substrates [43, 44]. Therefore, Al alloying into Cu might be promising for depositing adherent diamond thin films on Cu substrates.

Substrate surface roughness also influences the adhesion of diamond thin films on metallic substrates [45]. With high roughness, the caverns and holes on the surface of the substrates can trap diamond, forming mechanical inter-locking between the diamond thin films and the substrates and thereby increasing the adhesion strength. This method has effectively enhanced diamond thin film adhesion on tungsten and cobalt substrates [45, 46]. Therefore, increasing the surface roughness may also enhance diamond thin film adhesion on Cu substrates.

In summary, great efforts have been made to improve diamond thin film adhesion on metallic substrates, but no method has achieved good adhesion of diamond thin films on Cu substrates. Al alloying and surface roughing methods are promising approaches to solve this adhesion problem.

2.3 CNTs

2.3.1 Structure and Properties

Carbon Nanotubes (CNTs) were first discovered by Iijima in 1991 [47]. There are two types of CNTs: Single-Wall Carbon Nanotubes (SWCNTs) and Multi-Wall Carbon Nanotubes (MWCNTs). The structure of a SWCNT can be depicted as a hollow cylinder made by rolling a graphene sheet. The rolling manner is determined by vector C, which can be calculated using equation (2.1) [48]:

$$C=na_1+ma_2, \quad (2.1)$$

where a_1 and a_2 are graphite vectors, and n and m are integers. The tube is formed by rolling the vectors onto each other. Three different manners of rolling make three different SWCNT structures: armchair, zigzag, and chiral (Figure 2.6) [48].

A SWCNT can be a conductor or a semiconductor depending on the manner of rolling [49-51]. Due to the strong σ bonds, as in graphene, SWCNTs have incredible mechanical strength and high thermal conductivity [48, 52]. Theoretical calculations and experimental measurements have demonstrated that SWCNTs can be as stiff as diamond and have an ultra -high Young's modulus and tensile strength [53]. The thermal conductivity of SWCNTs has been measured as comparable to diamond at room temperature [54].

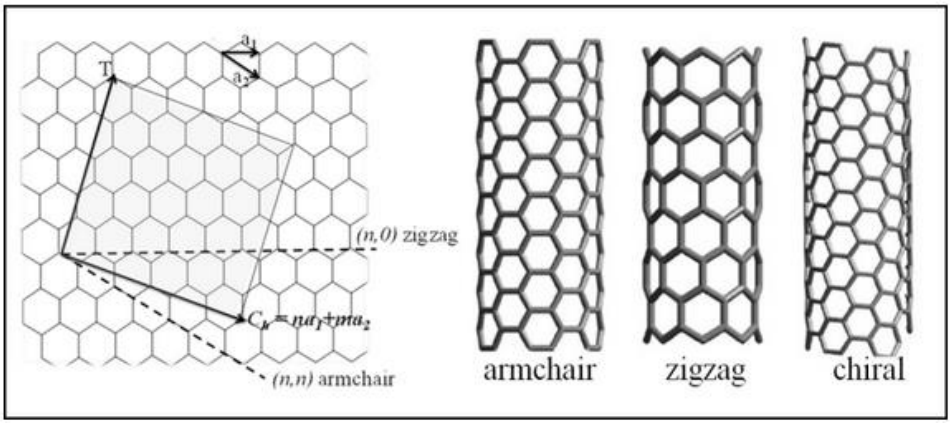

Figure 2.6. Three types of carbon nanotubes rolled from a sheet of graphene [55].

MWCNTs are concentric tubes of graphene, with an interlayer spacing of 3.4 nm. They have properties close to SWCNTs, including a high Young's modulus, tensile strength, and thermal conductivity.

2.3.2 Synthesis of CNTs

In the early days of CNT synthesis, arc discharge and laser ablation were the main methods employed [56]. Later, to satisfy the demands of scaled-up production of controlled or patterned CNTs for FEE and other applications, CVD techniques were developed. CVD growth of CNTs is considered to follow a VLS mechanism according to observations from high-resolution transmission electron microscopy (HRTEM) [57]. In this mechanism, the vaporized precursors (V) are dissolved into catalyst particles to form an eutectic phase with a lower melting point, causing the particle to become liquid (L). The concentration of precursor increases until oversaturation is reached. After that, a solid carbon phase (S) precipitates from the liquid catalyst particle. As the precipitation continues, a nanotube nucleates and grows. The most commonly used CVD techniques for CNT growth are thermal CVD, HFCVD, and MPCVD.

2.3.2.1 Thermal CVD

A schematic of a thermal CVD reactor is shown in Figure 2.7. In thermal CVD, a thermal furnace supplies the heat to decompose the precursors for CNT growth. A catalyst is required for this process and can be introduced either before growth as a supported catalyst

on the substrate or during growth as an injected floating catalyst [58, 59]. The floating catalyst method is good for large scale CNT production [60]. Thermal CVD can be used to synthesize both SWCNTs and MWCNTs. The merits of thermal CVD include low cost and easy set-up. The major downside of thermal CVD is the high temperature required for deposition. Especially for SWCNT, temperatures over 900 ℃ are necessary for deposition.

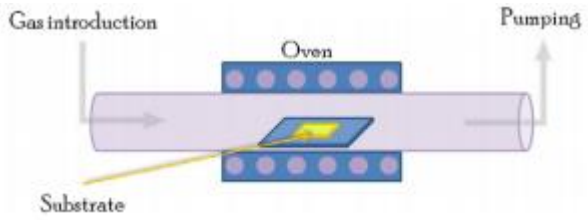

Figure 2.7. Schematic of a thermal CVD reactor [61].

2.3.2.2 HFCVD

HFCVD reactors (see Figure 2.5) can also be used for CNT growth. The filament supplies heat to decompose the precursors for CNT growth. The catalyst can be either supported by the substrate or floated in using gases, as is done in thermal CVD. For CNT growth, HFCVD has some advantages over other CVD techniques. It has better heat control than thermal CVD. In thermal CVD, the substrate temperature is similar to the precursor decomposition temperature because the whole chamber is uniformly heated in a furnace. In this case, it is impossible to adjust the deposition temperature without changing the temperature for the gas to decompose. But, in HFCVD, the substrate temperature can be controlled by adjusting the distance between the filament and the substrate without changing the filament temperature. CNT deposition with a low substrate temperature and high filament temperature can be achieved by HFCVD. Another advantage of HFCVD is that it is flexible with respect to setting up extra attachments for specific research demands. For example, in the present work, a DC bias was applied between the filament and substrate to enable vertically aligned CNT growth. The bias provides the driving force needed to align the CNT.

However, HFCVD has disadvantages of being easily contaminated from the evaporation of the filament and limited filament stability and lifetime.

2.3.2.3 MPCVD

MPCVD utilizes a plasma to heat and decompose the precursors for CNT growth. In the CNT deposition process, the plasma decomposes the precursor at relatively low temperatures. This could result in a much lower substrate deposition temperature than the previous two CVD methods. MWCNTs and Multi-Wall Carbon NanoFibers (MWCNFs) can be deposited at temperatures lower than 120 ℃ [62, 63]. These low temperatures can be tolerated by most substrates. However, MPCVD for CNT growth is not uniform because the plasma ball induced by microwave results in different plasma density at substrate surface.

2.3.3 Alignment of CNTs

The alignment of CNTs is crucial for FEE and FBHT applications. Aligned CNTs could have a high FEE current density due to the increase of β values [4]. The β value is related to the emitters' aspect ratio, which is high in aligned CNTs. Aligned CNTs also have a high heat transfer efficiency due to the increased contact area in the flow. In order to obtain CNTs with desirable alignment, it is necessary to understand the CNT growth mechanism.

2.3.3.1 CNT growth mechanism

During CNT deposition, a hydrocarbon precursor such as methane is decomposed and dissolved into the catalyst particles. Once a supersaturated state is reached, carbon precipitates in a crystalline tubular structure, which is followed by CNT growth. Under such conditions, there are two possible CNT growth models [64-66]. When the catalyst particle has a strong adherence to the surface, carbon precipitates at the top surface of the catalyst particle and continues to grow with the particle attached to the substrate. This is called the "base growth" model. In contrast, when the catalyst particle has a weak adherence to the surface, carbon precipitation occurs at the bottom surface of the particle and the growing CNTs lift the particle as they grow. In this case, the catalyst particles are embedded at the top end of the CNT and this is called "tip growth" model. Baker first proposed the above

mechanism for carbon filament growth based on electron microscopy observations [64-66], and it is commonly accepted that this mechanism can also be used to explain CNT growth. The observation of catalyst particles located at either the top or bottom end of CNTs supports this growth mechanism [67-70]. Wang *et al.* reported that this CNT growth mechanism is related to the dynamic interplay between the catalysts and CNTs, as well as the interactions between the catalyst and substrate [70]. When the catalysts are treated to have a reduced adhesion between the catalysts and the substrates, the CNT growth changes from base growth to tip growth. When bias was used to assist aligned CNT growth, the catalysts at the tips would be attracted by the electric field and create a stress that assists CNT alignment [71]. On contrary, catalysts at base do not show this effect. Therefore, tip growth enhances alignment.

2.3.3.2 Aligned growth methods

Currently, there are three mature methods to synthesize aligned CNTs using CVD techniques [72-74]. "Crowding effect" was firstly used to grow high density CNT arrays where the van der Waals forces between high density CNTs arrays facilitate aligned growth. This high density of CNT arrays can be achieved using high density catalysts. A growth template was then used to fabricate aligned CNTs. Kim *et al*., Sui *et al*., and Lee *et al*. chose a nanoporous Anodized Aluminium Oxide (AAO) template to fabricate aligned CNTs [73, 75, 76]. The template was designed to have nanosized pores filled with catalyst. The walls of the pores supported the aligned growth. Biasing the substrates has also been used to assist aligned growth. Aligned CNTs were obtained by biasing the substrate with negative voltage in a DC discharge [77]. Yang *et al.* deposited well aligned CNTs on Inconel sheets by HFCVD at a bias voltage of -500 V [78]. Chowalla *et al*., Chen *et al*., and Merkulov *et al*. synthesized vertically aligned CNTs using a similar technique [79-82]. Catalyst particle size has also been found to influence CNT alignment. Yang *et al*. reported aligned CNTs could not be obtained until the catalyst size was 1 μm or larger [78].

2.4 Diamond and CNT Hybrids

As discussed in the preceding sections, both diamond and CNT are carbon materials with outstanding properties. A hybrid material combining them could take advantage of their unique properties and have broader applications.

2.4.1 Synthesis of Hybrids

2.4.1.1 Transformation of CNTs to diamond

Diamond and CNT are two different allotropes of carbon. Under specific conditions, they can transform into each other. Two mechanisms have been proposed to explain the transformation of CNTs to diamond by hydrogen treatment: solid–solid phase transformation and solid–gas–solid phase transformation [26, 83, 84]. In solid–solid phase transformation, the point defects created by the hydrogen treatment at the CNT surface show sp^3 bonding structure and act as nucleation sites for diamond growth. In solid–gas–solid phase transformation, hydrogen reacts with graphite at elevated temperatures to form a variety of hydrocarbon species and radicals. These species include CH_4 and CH_3 radicals with sp^3 bonding, which are precursors for diamond nucleation and growth. Diamond nanostructures such as nanorods and diamond nanowires can be synthesized from CNTs by this transformation mechanism [85-87]. Previous publications have demonstrated that diamond can be synthesized by transformation from CNTs. Yang *et al.* used MWCNTs as a precursor to synthesize diamond in a pure hydrogen plasma discharge. It has been shown that diamond can nucleate on a CNT surface [84]. Wang and Cao [88] transformed CNTs into diamond using a high temperature and high pressure method. Diamond crystals could not be obtained under these conditions if graphite was used as the raw material rather than CNTs. In this transformation, CNTs are first converted into a middle phase of quasi-spherical onion-like structures before being transformed to diamond crystals. In other work by Zhang *et al.*, Spark Plasma Sintering (SPS) was used to convert CNTs to diamond [89]. The results showed that MWCNTs can be transformed into micro-diamond at a high temperature of 1500 ℃ and a high pressure of 80 MPa. The diamond synthesized was single or agglomerated crystalline

particles with a maximum size of 100 μm. These diamond particles appeared on top of a layer of amorphous carbon and residual CNTs. In addition, Sun *et al.* transformed multi-wall carbon nanotubes into nanocrystalline diamond by hydrogen plasma post-treatment [90]. Similar transformation of MWCNTs or carbon onions into nanodiamond by hydrogen treatment has also been reported by Banhart and Wen [91, 92].

2.4.1.2 Growth of Diamond on CNTs

In addition to being transformed from CNTs, diamond can directly nucleate and grow on CNT surfaces using CVD techniques. The difference between transformation of CNTs to diamond and growth of diamond on CNTs is that the transformation utilizes CNTs themselves as precursor without adding other carbon sources while the growth consumes carbon-containing gas precursors. In this chemical reaction, atomic H plays a key role in diamond nucleation [93]. H atoms decomposed from H_2 gas have high energy that can capture carbon atoms in the CNTs and form C-H gases. The missing carbon atoms in CNTs form point defects. These defects created by H attack show sp^3 bonding and become nucleation sites for diamond growth. To confirm this theory, Muniz *et al.* performed a simulation of nucleation of nanocrystalline diamond on different graphene walls [94]. The results showed that diamond nucleation can take place on CNTs with different diameters and graphene walls. Related experimental results also support the growth of diamond on CNTs. Terranova *et al.* reported nanosized diamond growth on SWCNTs using an HFCVD method [93]. They obtained a nanodiamond coated SWCNT hybrid material and believed that H atoms attacking CNTs was the critical factor in this reaction. Yang *et al.* synthesized diamond thin films and nanotips through etching of graphite by hydrogen [83]. Barnard *et al.* reported that the sp^3 hybridized defects on SWCNT provided the nucleation sites for nanodiamond growth [95]. Orlanducci *et al.* mentioned nanodiamond growth on SWCNT using nanocarbon powders in an HFCVD reactor [96]. Shankar *et al.* deposited nanodiamond on CNTs using an HFCVD method and found that high hydrogen concentrations in the reaction chamber could completely destroy CNTs while low hydrogen concentrations could result in the formation of a diamond/CNT hybrid material [97].

2.4.1.3 Growth of CNTs on Diamond

Diamond and CNT hybrid material can also be prepared by depositing CNTs on diamond using CVD techniques. The growth of CNTs usually requires transition metal catalysts (iron, nickel, or cobalt) [58], with the size and density of the catalyst particles determining the diameter and density of the CNTs, respectively. Fernandes *et al.* reported the growth of CNTs on nanodiamond by MPCVD using an iron catalyst [98]. Tumilty *et al.* obtained vertically aligned MWCNTs on a single crystal diamond using a glow discharge method where a nickel film deposited by vacuum evaporation was used as a catalyst [68]. Recent research showed that nanodiamond could also be a catalyst for the growth of CNTs. Diamond and CNT hybrid material prepared by this method could have direct bonds formed between diamond and CNTs. Takagi *et al.* successfully deposited CNTs on diamond without using a metal catalyst and found that nanosized diamond (4-5 nm) could act as a catalyst for CNT nucleation [99]. Wang *et al.* synthesized metal-free CNTs on diamond substrates and proposed that the hexagonal planes of the n-diamond could provide the catalyst sites for the nucleation of CNTs [100].

2.4.2 Properties and Applications

When CNTs and diamond are combined to form hybrid materials, they can theoretically form covalent bonds with each other, which results in good adhesion between them. This theory was proposed by Shenderova *et al.* [101] and Horner *et al.* [102] and then experimentally confirmed by Tumilty *et al.*, Terranova *et al.*, and Takagi *et al.* [68, 87, 99]. Shenderova *et al.* used density functional based tight-binding simulations to calculate covalent bonding between CNTs and the diamond surface to explain the absorption of CNTs onto diamond (100)-(2x1) surface. Horner *et al.* calculated the interaction of carbon nanotubes with a non-hybrid (100) diamond surface and determined the characteristics of the covalent interface formed between these two materials; the most stable (5,5) nanotube-diamond structure had a binding energy of 1.7 eV. From the theoretical research

above, strong covalent bonding is believed to be formed between diamond and CNTs. Terranova *et al.* synthesized a nanostructure by direct nucleation of diamond on the defects of CNT surfaces. The hybrid material obtained had direct bonding between diamond and the CNTs due to the direct growth of diamond. Takagi reported CNT growth from diamond without use of a catalyst. They proposed a "vapor-solid surface-solid" (VSSS) CNT growth model in which CNT growth on the nanodiamond surface is analogous to the homoepitaxial growth of diamond with C-C covalent bonding. Tumilty *et al.* reported the synthesis of CNTs on diamond using a nickel catalyst. The resultant CNTs adhered strongly to the diamond, suggesting strong C-C covalent bonds between the CNTs and the diamond. Therefore, diamond and CNTs hybrid structures could feature covalent bonds between the CNTs and the diamond, which guarantees good adhesion.

Diamond and CNT hybrid materials have many potential applications [1-10]. One application is as a heat sink for high-power electronic devices. They can be good replacement candidates for the traditional heat sink material due to the high thermal conductivity of both diamond and CNTs. Another potential application is for FEE emitters. The poor adhesion of CNTs to the substrate is a major cause of FEE failure. The good adhesion between CNTs and diamond could improve CNT FEE stability.

2.5 Field Electron Emission

2.5.1 Basic Knowledge

2.5.1.1 Electron emission phenomenon

Electron emission is a process in which electrons are excited and emitted from a solid surface. Inside a metal, electrons are free to move but cannot escape to vacuum due to the potential barrier at the surface. To escape from the metal surface into vacuum, electrons need to obtain sufficient energy to overcome the energy barrier, which is called the work function (ϕ). The work function is related to the surface characteristics and morphologies of solids. The energy required for electrons to escape can be supplied by heating, absorption of light, or an electrostatic field. In FEE, electrons are excited by a strong electrostatic field (could over

10^6 V/m) and emitted from solids into vacuum. The other two types of emission are Thermionic Electron Emission (TEE) and photoemission.

2.5.1.2 Thermionic electron emission

Thermionic electron emission is based on the emission of electrons by transferring energy from crystal lattice vibration in solids at elevated temperature. It is related to the status of electrons at different temperatures. There are two versions of the electron distribution function. At absolute zero, it is a step function, as follows [103],

$$n(E) = \begin{cases} 1 & E < E_f \\ 0 & E > E_f \end{cases}, \qquad (2.2)$$

where E_f is the Fermi level. At a finite temperature, it becomes a continuous function due to the fact that electrons can be excited to occupy energy levels above the Fermi level. The electron distribution function follows the Fermi-Dirac distribution function [103],

$$n(E) = \frac{1}{\exp\left(\frac{E-E_f}{kT}\right)+1}, \qquad (2.3)$$

where n(E) is the probability density of occupation (average number of electrons per unit energy per unit volume) of a state with energy E, E_f denotes the Fermi level, k represents the Boltzmann constant (1.38×10^{-23} J/K), and T the absolute temperature. From equation (2.3), it is known that the probability of occupation is related to the temperature and the energy difference $E-E_f$. Neglecting other factors (for example, external electric field), only electrons with energy levels higher than the vacuum level can overcome the barrier and escape.

Richardson and Dushman studied thermionic electron emission from metals at high temperature. The emission current j of thermionic electron emission can be calculated using equation (2.3) [104, 105],

$$j = \int en(E)v(E)dE, \qquad (2.4)$$

where j is the emission current density, *e* is the magnitude of electron charge, *E* is the electron energy, and *v*(E) is the velocity distribution. n(E)dE is the density of electrons, in the energy range between E and E + dE, per unit volume, which can be calculated using equation (2.5),

$$n(E)d(E) = \frac{8\pi m^3}{\hbar^3}\frac{v^2 dv}{1+\exp(\frac{E-e\varphi}{kT})} \ , \tag{2.5}$$

Then, equation (2.4) can be written as

$$j\,(\Phi, T) = AT^2 \exp(-\frac{e\varphi}{KT}), \tag{2.6}$$

$$A = \frac{emk^2}{2\pi^2\hbar^3}, \tag{2.7}$$

where ħ=h/2π, h is Planck's constant, k represents the Boltzmann constant (1.38×10^{-23} J/K), and T the absolute temperature.

At low temperatures, thermionic electron emission is extremely low due to the density of electrons with energy higher than the vacuum level is very low. At high temperature, electrons will be thermally excited to occupy higher energy levels. Thus, thermionic emission electrons are generated.

2.5.1.3 Schottky electron emission

In the discussion of thermionic electron emission, the effect of the external electric field was neglected. In fact, external electric field affects electron emission. Low external electric field lowers the work function of a metal surface shown in equation (2.8),

$$\varphi' = \varphi - e^{3/2}F^{1/2} \ , \tag{2.8}$$

and enhance the thermionic electron emission, resulting in equation (2.9) [103],

$$J_f = j_0 \exp\left(\frac{e^{3/2}F^{1/2}}{KT}\right) \ , \tag{2.9}$$

where *F* is the electric field, j_0 is the thermionic electron emission current density from zero electric field at a temperature of T, k is the Boltzmann constant (1.38×10^{-23} J/K), *e is* the magnitude of electron charge, and T is the absolute temperature. Using $j_0 = AT^2 \exp(-e\phi/kT)$ from equation (2.6), then j_F, the emission current density for an electric field *F*, is

$$j_F = j_0 \exp\left(\frac{e^{\frac{2}{3}}F^{\frac{1}{2}}}{kT}\right) \ , \tag{2.10}$$

This enhanced emission is called Schottky lowering. This theory was proposed by Schottky and has been demonstrated to be valid over a wide range of temperatures and fields up to 1×10^6 V/cm [106]. In Schottky electron emission, the external electric field lowers the surface barrier of the emitters and enhances the emission current. This model is relatively

accurate for external electric fields lower than 1×10^6 V/cm. Above that, FEE from Fowler-Nordheim (F-N) tunneling becomes the dominant emission mechanism. In the Schottky electron emission regime, electrons are emitted from states above the emitter's Fermi level while in FEE electrons are emitted from states close to the emitter's Fermi level. Schottky electron emission is an enhancement of thermionic electron emission while FEE is temperature independent.

2.5.1.4 Field electron emission

A FEE process can be broken down into two steps. The first step is the transportation of electrons to the surface of emitters. The second step is the tunneling of the electrons through the surface barrier of emitters into vacuum. At low temperature, the movement of electrons inside the metals is finite due to the potential barrier. When an external electric force is applied to metals, the potential barrier is reduced. FEE occurs when the potential barrier width is small enough to allow electrons to tunnel through metals. FEE of semiconductors is different with respect to the work function. The work function of metals is simply the energy difference between the Fermi and vacuum levels while the work function of a semiconductor is complicated. If electrons are emitted from the conduction band of a semiconductor, the work function is the energy difference between the conduction band minimum (CBM) and the vacuum level. If electrons are emitted from the valence band of the semiconductors, the work function is the energy difference between the valence band maximum and the vacuum level.

In 1928, Ralph H. Fowler and Lothar Wolfgang Nordheim proposed the theory of FEE from solids [107]. As a fundamental FEE theory, the (F-N) theory gives an analytic formula for the emission current density versus the external electric field (J-F). The Fowler-Nordhein theory makes a series of assumptions to simplify the FEE model: The emission follows sommerfeld model which presents the emission properties of metals. The electron emission obeys the Fermi-Dirac distribution function f (E). A triangular potential barrier is assumed in Vacuum. The emission is considered at the tip of the emitter and the effects of substrates are neglected. The emitter is perfect without impurities and defects. The work function of emitter

is independent of external electric field. Electron tunneling arises only along one direction due to the tip of emitter is usually sharp from the macroscopic point of view and electrons tunnel through the vacuum potential from the thinnest region of the potential barrier. Based on these assumptions, they proposed the F-N equation,

$$I=AJ=At_N^{-2}\,\alpha^{\phi^{-1}}\beta^2E^2\exp\{-v_Nb\phi^{3/2}/(\beta E)\}, \quad (2.11)$$

where A is the effective emission area, I is the emission current, J is the emission current density, Φ is the local work function, E=V/d represents the nominal electric field, β is the field enhancement factor (FEF) which is related to the field F in the tunneling barrier to E (i.e., F = βE), α ($1.5410^{-6}AeVV^{-2}$) and b ($6.8310^{-9}eV^{-3/2}Vm^{-1}$) are constants, and v_N and t_N are Nordheim functions.

In order to obtain the emission properties of the solid material, an F-N equation of ln (I/V^2) vs. 1/V derived from the current-field curve is proposed. This plot gives a direct description of the FEE properties of the solid material (Figure 2.8). The linear curve of the F-N plot indicates electron emission from the tunnel effect, and the slope of the curve is related to the field enhancement factor (β). The absolute value of the emission current enables one to evaluate the area of the emitting surface. CNT emitters have a high aspect ratio, and thus the magnitude of the electric field on the tip of a vertically aligned CNT exceeds by approximately l/d times the average magnitude, which is determined as the ratio of the voltage applied V to the distance between the nanotube's tip and the anode.

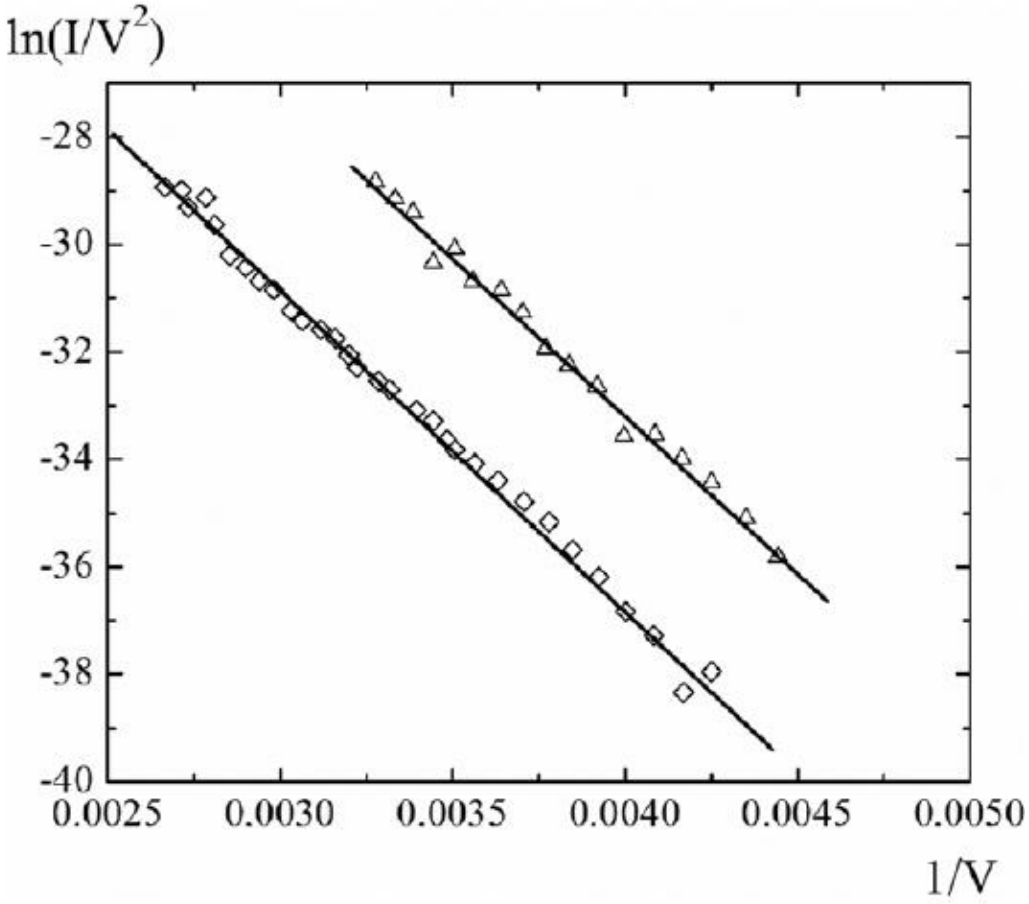

Figure 2.8. A typical F-N plot for CNTs before (triangle) and after (square) heat treatment [108].

In F-N theory, β can be calculated using equation (2.12,

$$\beta = bd\Phi^{3/2}/m \,, \tag{2.12}$$

where $b = -6.83\times10^{7} eV^{-3/2} Vcm^{-1}$, $d = 5\times10^{-4}$ cm, m is the slope of the F-N plot, and Φ is the work function of the CNTs in eV, here assumed to be 5.0 eV [109]. Figure 2.8 is a typical F-N plot of an individual CNT emitter. These two curves are F-N plots for CNTs before (triangle) and after (square) heat treatment.

From equations (2.11) and (2.12), the effective emission area A can be calculated using the following equation:

$$\ln(I/E^2) = \ln(A\alpha\Phi^{-1}\beta^2) - b\Phi^{2/3}/\beta E \,, \tag{2.13}$$

When CNTs are used for FEE emitters on metallic substrates, there are two potential barriers [13]. The first is the barrier at the interface between the CNTs and substrates that blocks

electron transfer to the CNTs. The second is the barrier between the CNT surfaces and the vacuum that blocks electron emission to vacuum. The two barriers are shown in Figure 2.9 [13]. The electrons emitted from the substrates to vacuum need energy to travel through these two barriers. The FEE turn-on field, defined as the electric field resulting in an emission current of 0.01 μA [103], of CNT emitters on metallic substrates is determined by the height of these barriers.

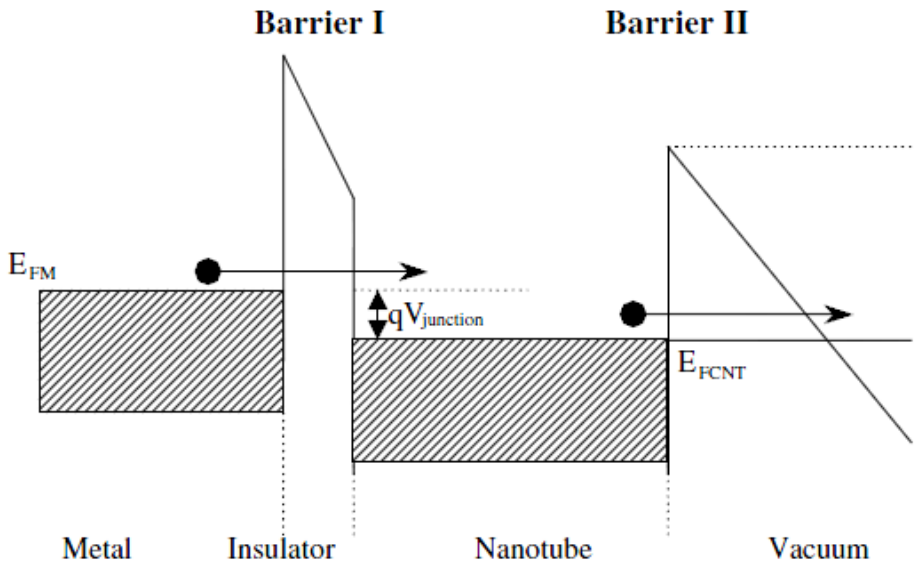

Figure 2.9. Band diagram of a two barrier model for CNT FEE emitters. EFM and EFCNT are the Fermi levels of the substrate and CNT, respectively. Vjunction is the voltage drop at the substrate/CNT junction [13].

2.5.1.6 Effective electron mass of CNT FEE emitters

Effective electron mass is defined as the mass of the electrons responsive to the external electric force. It is broadly used to calculate the electron transport in solids under the influence of the electric field. The effective electron mass of a solid can be calculated using equation (2.14),

$$m^* = \frac{\left(\frac{h}{2\pi}\right)^2}{\frac{d^2E}{dk^2}} \quad , \tag{2.14}$$

where m* is the effective electron mass, h is the Planck constant, E is the energy, and k is the

wave vector of the solid.

The energy E of a SWCNT consists of a set of one-dimensional energy dispersion relationships. The energy dispersion relationship of a SWCNT is given by calculating the electronic structure of graphene using equation (2.15) [110],

$$E = \pm v_{pp\pi}\left[1 + 4\cos\left(\frac{\sqrt{3}K_x}{2}a\right)\csc\left(\frac{K_y}{2}a\right) + 4\cos^2\left(\frac{K_y}{2}a\right)\right]^{1/2}, \quad (2.15)$$

where $V_{pp\pi}$ is the nearest neighbor overlapping integral between carbon-carbon atoms used in the tight binding calculation of CNTs, and K_x and K_y are wave vectors of CNTs. Then, the effective electron mass of CNTs can be calculated from equations 2.10 and 2.11. The simulation of effective electron mass for MWCNTs arrays is difficult due to the variance in characteristics of each tube, including length, diameter, and electrical conductivity. All of these factors complicate calculations and make it difficult to predict the characteristic of the MWCNTs.

The effective electron mass of MWCNTs can be estimated using the F-N equation (2.16) [111],

$$j_{FN} = AE^2\exp\left(-\frac{B}{E}\right) , \quad (2.16)$$

where j_{FN} is the field emission current density, E is the electric field applied, and A and B are defined as

$$A = \frac{q^2 m}{8\pi h m^* \Phi_B} , \quad (2.17)$$

$$B = \frac{8\pi\sqrt{2m^*}}{3qh}(q\Phi_B)^{3/2} , \quad (2.18)$$

where Φ_B is the effective barrier height, m^* is the effective electron mass, h is the Planck constant, and q and m are the electron charge and mass, respectively. Therefore, effective electron mass m^* can be calculated if we know the effective barrier heightΦ_B.

2.5.2 Field Electron Emission Applications

The application of FEE technology began in the 1920s with the design of X-ray tubes for medical applications [112]. Since then, FEE techniques have been used in a wide variety

of electronic devices. Currently, the most used FEE devices on the market are FEE SEMs, cathode ray lighting tubes, X-ray sources, and microwave amplifiers. FEE devices have obvious advantages over older Thermal Electron Emission (TEE) devices. TEE devices require a heating time upon startup, while FEE devices have a shorter response time allowing them to be turned on and off in a faster manner. FEE devices have a longer service lifetime due to a low working temperature while TEE devices work at a much higher temperature and therefore their service lifetime suffers.

Recently, a new FEE device, Field Emission Display (FED), has been developed. This device is still under development by companies including Sony, Samsung, and AU Optronics. A 35-inch high definition CNT-FED monitor has been invented by Samsung SDI C0 [7]. There are several advantages associated with FED. First, an FED monitor can be thinner than a conventional cathode ray tube monitor due to there is no need for electronic beam deflection. Second, an FED monitor can provide more dynamic colors than a liquid crystal display monitor. Last, an FED monitor is more energy efficient due to the power consumption of an FED monitor is much less than either a cathode ray tube monitor or liquid crystal display monitor.

2.5.3 Field Electron Emission Materials

2.5.3.1 Tungsten

Conventional FEE emitters are metallic micro-tips, for example, tungsten tips. They have been broadly used in cathode ray lighting tubes, X-ray sources, and Field Emission Scanning Electron Microscopes (FESEM). However, due to high production costs and degradation of the tips, metallic FEE devices are not competitive with other types of devices. The cost of producing metallic FEE emitters is high due to difficulties in fabricating micro-size metal tips. During emission, gas molecules are ionized and bombard the tip, causing tip degradation that further results in failure of the metal emitters. To reduce this ion etching, a high vacuum working environment is needed, which increases the assembly cost of FEE devices.

2.5.3.2 Diamond

Diamond is regarded as new type of FEE emitter due to its high mechanical strength, chemical inertness, and Negative Electron Affinity (NEA) [113]. The electron affinity χ is defined as the energy difference between the vacuum level and the CBM. The electron affinity value represents the energy needed to extract an electron from the CBM to vacuum. When solids have a positive electron affinity (PEA), the electrons at the CBM need a certain energy to escape from the solid surface. But when solids have NEA property, electrons at the CBM are free to leave. It has been reported that CVD diamond has a NEA due to the hydrogen-carbon bond on the diamond surface [114]. This hydrogen-carbon bond is commonly found at the CVD diamond surface due to the use of hydrocarbon precursors in diamond CVD synthesis.

It is known that diamond has low electrical conductivity, which is undesirable for FEE applications. But evidence shows that diamond can exhibit FEE behavior [1, 2]. It is believed that the graphitic phase of diamond is crucial for diamond's FEE phenomena. In the graphitic phase, sp^2 carbon exists at the diamond grain boundary. Research has shown that the graphitic phase can be a bridge to transport electrons from the substrate to the diamond surface [114]. Electrons are transferred into the vacuum through this specific region of the diamond. However, the effect of the sp^2 content of diamond on FEE is still not clear.

2.5.3.3 CNTs

CNT FEE emitters can overcome limitations of metallic FEE emitters due to their unique physical and chemical properties and low production cost. The strong C-C bonds of CNTs provide good mechanical strength and chemical inertness against emission degradation. CNTs can be mass produced at low cost using CVD techniques. CNT FEE performance is dependent on the potential barrier height of the emitters and the density of the tubes [4, 115]. The potential barrier height corresponds to the properties of the CNTs, substrates, and their junction. A minimum potential barrier is desirable to achieve high emission current. In addition, the emission current density is depended on the density of CNTs. To obtain a high FEE emission current, CNT emitters must be aligned with optimal density [16, 73]. Nilsson

calculated that the optimal density of CNTs occurs when the height of the CNTs is about 1.5 times the inter-tube space [16]. If the density of CNT arrays is too low, there will not be enough emitters to emit electrons, resulting in a low emission current. If the density of CNT arrays is too high and the tubes are too close to each other, emission of electrons from CNTs will be shielded by the electric field from neighboring tubes. This shielding results in reduced electric field at the tip of CNTs, resulting in the decrease of emission current. This effect is called the "screen effect". Many approaches have been attempted to obtain an optimal CNT density. A common method for controlling the density of CNTs is to control the density of catalysts using a template [73]. However, this method is complicated, and cannot be used to achieve mass production of CNTs FEE emitters. It is necessary to find a simple and effective technique to control the density of CNTs for FEE applications.

A limitation to the use of CNT FEE emitters in practical applications is the poor FEE stability: a gradual drop of emission current with emission time. Two mechanisms have been proposed to explain this emission failure.

The first mechanism suggests that the poor stability is due to ion bombardment from the gas phase in the emission or selective oxidation [116, 117]. This failure has been observed for SWCNT and arc-discharge MWCNT FEE emitters. Layer-by-layer burn out of MWCNTs prepared by an arc-discharge method was observed during emission using *in situ* TEM [118]. Bonard *et al.* prepared CNTs by an arc-discharge method and compared the degradation of single wall CNTs and multi wall CNTs over time [116]. It was found that the degradation rate of single-wall CNTs was much faster (factor $\geqq 10$) than that of multi-wall CNTs, and this was attributed to ion bombardment from the gas phase gradually destroying the CNTs layer by layer. As this degradation rate is low, the CNT FEE emitter's lifetime can be more than 8000 hours.

The second mechanism suggests that the mechanical failure caused by the tensile loading of the emitter under the applied electric field is responsible for the emission degradation. The weak contact between the CNTs and the substrate results in heat accumulation by the CNTs, which will eventually burn out the CNTs. This failure is mostly

observed on CVD MWCNTs due to the poor contact between CNTs and substrates. Bonard *et al.* used a two-probe characterization method and observed the failure of multi-walled CNTs prepared by an HFCVD method [12]. They used Keithley 237 source-measure units for testing. The two-probe method uses a single CNT emitter as the cathode and W needles as the anode. SEM was used for *in situ* observation of CNT destruction (Fig. 2.10). The burn out of CNTs was observed. SEM micrographs showed that even a small applied voltage (2V) is sufficient to destroy CNTs. Using simulation, the force necessary to fracture a well-anchored multiwall arc-discharge nanotube was found to be much higher than for CVD-grown tubes. So, it is believed that the main FEE failure of CVD CNTs emitters is due to poor contact with the substrate.

The CNT FEE stability testing was usually carried out by measuring the degradation of emission current over time at a high emission current (over 1 uA) [109, 117]. Sever degradation of current (i.e. degradation more than 50%) is regarded as failure of CNT emitters. However, up to now, no standard testing has been developed to define emission stability.

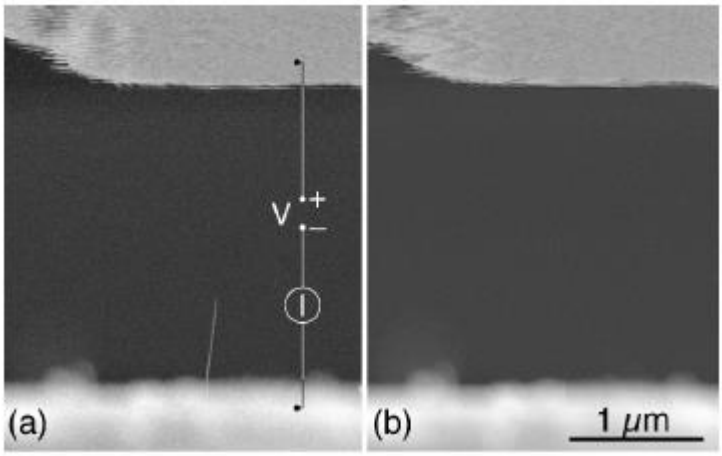

Figure 2.10. SEM micrograph of a nanotube of 0.66-mm length and 5-nm radius with the anode positioned at 2-mm distance before (a) and after (b) destruction of the tube [12].

To address the issue, work has been done to enhance the FEE stability of CNT emitters. One direction is to improve the heat conductivity of the substrate material. Lahiri *et al.* prepared a CNT-based field emitter on a Cu substrate [119]. Due to the high thermal

conductivity of the Cu substrate, their emitter could last for 300 minutes. This method, to some degree, improves the FEE stability of CNT emitters, but does not completely solve the heat accumulation problem; the lifetime of their emitter remains limited. Another method is to provide a protective and heat-conductive coating over the CNT surface [120]. Guglielmotti *et al.* reported SWCNTs coated with diamond nano-particles with stable emissions of up to 900 seconds [120]. The hard diamond thin films could protect the CNTs from being damaged by ion bombardment. However, the lifetime of this emitter is still short and it is not suitable for CVD MWCNTs. To enhance the stability, a third method of introducing an interlayer between CNTs and substrates has been developed. Park *et al.* used various buffer layers (TiN, Al, Al/TiN, and Al/Ni/TiN) between CNTs and tungsten to enhance the CNT's FEE stability [121]. The buffering layer improved the contact between the CNTs and the tungsten and enhanced the FEE stability. The Al/Ni/TiN layer showed the best lifetime, at up to 1440 minutes. Srividya *et al.* developed a Ti buffer layer to improve the field emission of a CNT based emitter and showed that the Ti buffer layer could improve contact between the CNTs and the substrate; a stable emission of longer duration (> 50 minutes) was achieved [122].

The above methods have, to some extent, prolonged the lifetime of CNT emitters but are far from meeting the requirements of practical applications. A longer service lifetime of thousands of minutes with a high emission current over 1 μA is desirable. Diamond has a high thermal conductivity and can be firmly bonded with CNTs. Using a diamond thin film interlayer would enhance the contact between CNTs and substrates and thus improve the emission stability of CNTs. Therefore, in the present research, a diamond interlayer is investigated for the improvement of the FEE stability of CNTs.

2.6 Flow Boiling Heat Transfer (FBHT)

2.6.1 Introduction

It is well known that Gordon Moore noted decades ago that "the number of transistors in a dense integrated circuit has doubled approximately every two years" [123]. Since then, the micro-chip has become so powerful that it requires an extremely efficient cooling system for

heat dissipation. There are two methods to enhance heat dissipation: active methods and passive methods [124]. In the active method, an external power source is supplied to enhance the heat transfer of the device. The passive method focuses on the modification of the surface of the device by adding a surface coating, increasing the surface area, or changing the working fluid of the device. Compared with the active method, the passive method is friend to the surrounding device.

Micro channel heat sinks are a passive method for Micro Electro Mechanical System (MEMS) based devices, and are considered to be more efficient heat dissipaters [125]. In the micro channel heat sink, two-phase flow can maintain a more stable and uniform surface temperature than single-phase flow due to its high heat transfer efficiency [126-128]. Flow Boiling Heat Transfer (FBHT) utilizes two-phase flow to achieve highly efficient heat transfer. In this heat transfer, the liquid coolant is at saturated conditions with a high heat transfer efficiency. The Critical Heat Flux (CHF) and onset boiling are two important parameters to represent the heat transfer efficiency. The CHF is the point where a dramatic decrease of heat transfer capabilities occurs and onset boiling is the point when liquid begins to vaporize and form bubbles in the flow.

2.6.2 CNTs as FBHT Materials

Recently, CNTs have been developed for FBHT applications and shown high heat transfer efficiency [14, 15, 129]. Singh *et al.* [129] reported significant heat transfer enhancement using CNTs on Si surfaces. Khanikar [14] defined the relationship between mass flux and CHF for the CNTs coatings by FBHT testing in a Cu micro-channel. Two mechanisms have been proposed for heat transfer enhancement using CNTs. One is the high thermal conductivity of CNTs and the other is the large surface area of CNT coatings that improves vapor embryo entrapment, and thus increases bubble nucleation for FBHT [15].

A major problem for CNTs in FBHT applications is weak adhesion strength on metallic substrates, which leads to high interfacial thermal resistance [12] and destroys CNTs under high coolant flow rates. Some researchers have attempted to solve this problem. Ujereh *et al.* adopted a Ti interlayer to enhance the adhesion between the CNT layer and the Cu substrate

[15]. Khanikar *et al.* used a triple layer catalyst system combining Ti, Al, and Fe to deposit CNTs on a Cu substrate [14]. The Ti layer anchored CNTs to the Cu surface, and the Al layer promoted the segregation of annealed Fe particles for catalyzing CNT growth. Kumar *et al.* used omega bond epoxy as an intermediate layer for CNTs grown on stainless steel substrates [130]. Tong *et al.* employed a thin layer of indium for CNT arrays grown on an Si wafer [131]. Improved adhesion was observed by these researchers. Lee *et al.* further reported that CNT wires had strong physical and electrical contacts with Ni-coated Cu [132]. However, the adhesion enhancement was insufficient for practical applications. Damage of CNTs by the flow has been observed. Therefore, it is desirable to develop new method for enhancing CNT adhesion on metallic substrates for FBHT applications. In this work, a diamond interlayer with strong adhesion to CNTs is used to further enhance the adhesion between CNTs and Cu substrates.

2.7 Characterization Techniques for Diamond, CNTs and Their Hybrids

2.7.1 SEM

Scanning Electron Microscopy (SEM) is a widely used characterization method for thin film coatings. It allows observation of the surface morphology of the substrate and coating materials. In this thesis, a JEOL JSM-6010 SEM located in the Department of Mechanical Engineering, University of Saskatchewan, was used to observe the surface morphology of the CNTs and diamond thin films. The magnification of this SEM ranges from 20 to 300,000× and the resolution limit is 4 nm. The accelerating voltage can be set from 2 to 20 KV, and the working distance is from 10 to 40 mm. This SEM has two detectors for both Secondary Electron Imaging (SEI) and Back-scattered Electron Imaging (BEI). The SEI detector gives secondary electron images, which provide sample topography for improved contrast. The BEI detector gives sample atomic number difference, with some topographic information [133].

2.7.2 TEM

Transmission Electron Microscopy (TEM) utilizes a high energy electron beam to travel through the thin specimen and form a diffraction pattern and image. Microstructures at the sub-nanoscale can be observed by TEM. Compared with SEM, TEM has much higher resolution and the ability to observe the detailed crystal structure of materials. TEM could characterize the structure of diamond thin films and CNT by identifying typical diffraction patterns and interplanar spacings. The diffraction pattern of a single crystalline material is displayed as dots while a polycrystalline material is displayed in the form of rings.

2.7.3 Raman Spectroscopy

Raman spectroscopy is commonly used to characterize carbon thin films by measuring the sp^2/sp^3 ratio and the stress in the thin films [134]. Raman spectroscopy is based on the mechanism of the Raman effect: "the inelastic scattering of incident monochromatic light". The Raman spectrum is the plot of intensity of scattered light versus the energy difference between the incident photon and the Raman scattered photon. Raman spectroscopy can qualitatively and quantitatively analyze matter and identify bond types present in the matter. Certain substances have characteristic peaks in the spectrum. For example, a sharp peak at around 1332 cm^{-1} is characteristic of natural diamond while a sharp peak at around 1580 cm^{-1} is characteristic of single crystal graphite [135,136]. Previous investigations have shown that the ratio of the integral area under the diamond peak and the graphite peak corresponds to the sp^3 to sp^2 ratio in diamond [137]. Based on Raman spectra, the sp^2/sp^3 ratio of diamond thin films is reported to increase with precursor methane gas concentration (from 1 vol.% to 50 vol.%) as shown in Figure 2.11 [103].

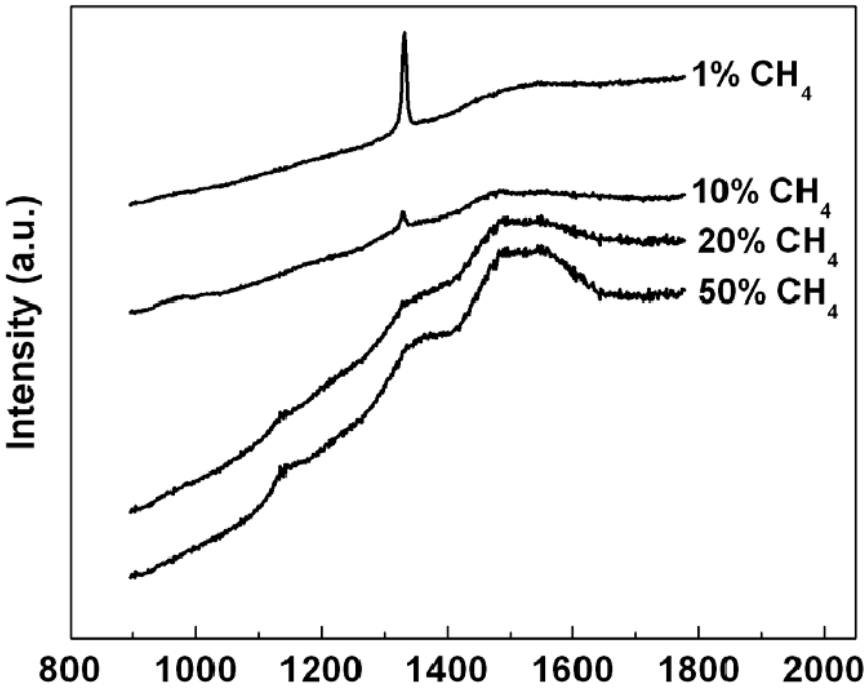

Figure 2.11. Raman spectra of diamond films grown under different CH_4 Vol concentrations with a -250 V substrate bias voltage [103].

2.7.4 Synchrotron-based X-ray Absorption Spectroscopy

A synchrotron is a type of particle accelerator that can be used to generate high brightness light to characterize structural and chemical properties of materials. A synchrotron has a powerful magnetic field to accelerate electrons and a circular orbital to confine and store the high energy electrons. Due to electrons are confined and accelerated in a circular orbital, synchrotron light is much brighter than that from a general optical light source. A synchrotron can create a broad range of light, from low frequency infrared light to high frequency X-rays and gamma rays.

When an X-ray generated by a synchrotron is directed at a sample, it will be absorbed, reflected, or transmitted. X-rays at specific energy levels radiated toward materials can excite inner core level electrons into an unoccupied electronic state and consequently emit photoelectrons, fluorescence electrons, and Auger electrons (Figure 2.12) [138]. X-ray Absorption Spectroscopy (XAS) can collect the emission electrons and Auger electrons to analyze the electronic state of the material. Depending on the electron collecting technique

employed, XAS can be conducted in Fluorescence Yield (FLY) mode or Total Electron Yield (TEY) mode. FLY mode measures fluorescence electrons emitted from samples and it is sensitive to the bulk material. TEY mode measures photoelectrons and Auger electrons emitted from samples and it is sensitive to the surface of the material.

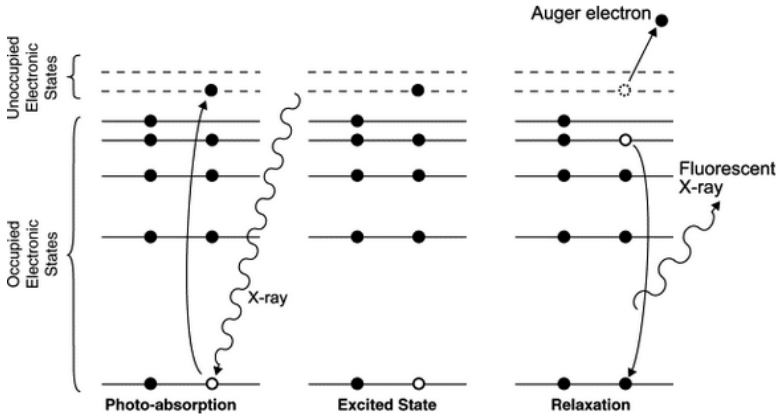

Figure 2.12. Schematic of the photo-absorption and relaxation process occurring in an XAS experiment [138].

2.7.5 Residual Stress Measurement

Diamond thin film coatings usually have internal (residual) stress after CVD deposition. In this thesis, the internal stress of the diamond thin film coatings was measured by Raman spectroscopy and XRD. In theory, compressive stress in the thin film results in an upshift of the Raman peak while tensile stress results in a downshift [139]. There is a linear relationship between Raman peak shift and stress for diamond thin films [139]. Kohzaki deposited diamond on an Mo substrate by thermal plasma CVD [140]. He calculated a linear relationship between Raman peak shift and stress, at around 2 cm^{-1} per GPa. Other factors such as grain size may cause Raman peak broadening [139] . When deposited diamond thin films cool down from elevated deposition temperature, the substrates shrink substantially while the diamond thin films almost maintain the original dimensions, resulting a compressive stress in the thin films. This stress causes up-shift of diamond Raman peaks [139].

XRD has been commonly used as a non-destructive approach for characterizing the crystal structure of materials. The XRD technique is based on Bragg's law,

$$n\lambda = 2d\sin\theta, \tag{2.19}$$

where λ is the X-ray wavelength, θ is the angle between the incident light and the diffraction surface, and d is the interplanar spacing. The diffraction pattern corresponds to the incident angle θ. The phase state of a crystalline material can be identified based on its diffraction pattern. XRD techniques are widely used to determine the internal stress in materials [141]. Macrostress can be measured based on the diffraction-line shift and microstress can be measured based on diffraction-line broadening. Figure 2.13 illustrates the influence of internal stress on XRD peaks [142]. Normally, compressive stress leads to a downshift of the diffraction lines while tensile stress leads to an upshift of diffraction lines.

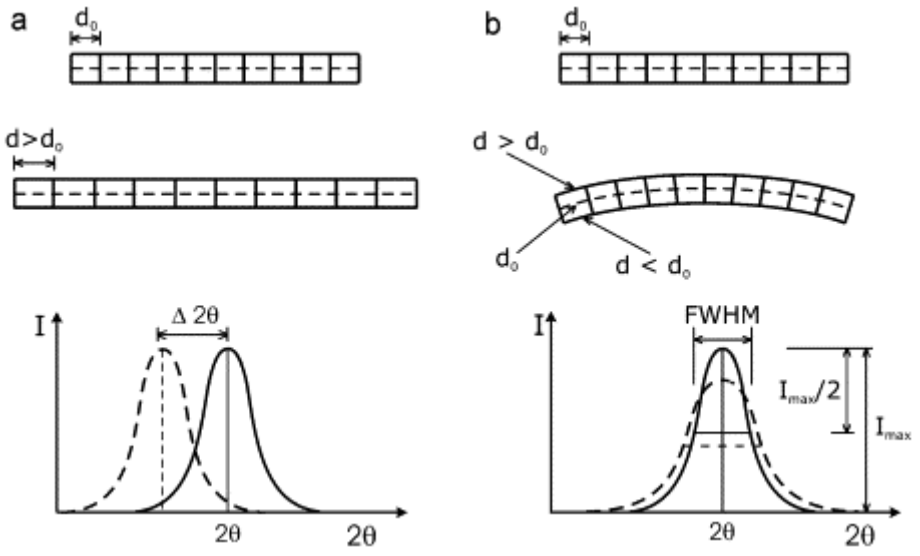

Figure.2.13. Influence of (a) macrostresses and (b) microstress on an X-ray diffraction peak. From Pinheiro [142].

2.7.6 Vickers Micro-hardness Indentation

The Vickers micro-hardness indentation technique was invented by Smith and Sandland in 1921 [143]. It is one of the most commonly used hardness tests [144]. Vickers hardness indentation equipment utilizes a diamond-shaped indenter and is an efficient and accurate

method to measure the hardness of materials at the micro-scale. Vickers hardness can be measured using following equation [144]:

$$\mathrm{HV} = \frac{2\mathrm{F}\sin(\frac{\theta}{2})}{\mathrm{d}^2} \times 1000, \tag{2.20}$$

where HV is the Vickers hardness, F is the test load, d is the mean of the diagonal of the indentation measured (μm), and θ is the angle of the indenter. As mentioned in section 2.2.3.1, Vickers Micro-hardness indentation is commonly used indentation methods for testing the adhesion of diamond thin films.

2.7.7 FEE Measurement

FEE measurement requires an ultra-high vacuum environment (usually ~10^{-6} Torr). The high vacuum could prevent the absorption of emitted electrons by air molecules and avoid an avalanche breakdown in the emission. According to Paschen's law, air molecules under a high voltage condition between two electrodes will be ionized and start a discharge [103]. The discharge will disturb the FEE measurement. The breakdown voltage can be calculated using

$$\mathrm{V_{breakdown}} = \frac{\mathrm{apd}}{\ln(\mathrm{pd})+\mathrm{b}}, \tag{2.21}$$

where $V_{breakdown}$ is the breakdown voltage, a and b are constants related to the properties of air molecules (a= 4.36×10^7 V/(atm.m), b=12.8 at standard temperature and pressure), P is the air pressure, and d is the distance between the two electrodes.

CHAPTER 3

EXPERIMENTAL METHODS

In this chapter, the detailed experimental methods used for the present research are being reported, including sample preparation, structural and mechanical property characterization, and measurement of FEE and FBHT characteristics.

3.1 Substrate

3.1.1 Substrate Materials

Cu has high thermal and electrical conductivity, which is desirable for substrate materials in FEE and FBHT applications. Therefore, it was chosen as the substrate for this research. Si is commonly used for diamond deposition due to its good affinity to diamond. In this thesis, Si was chosen as the reference substrate material.

3.1.2 Substrate pretreatment

3.1.2.1 Scratch treatment of substrates

The pretreatment of substrates can significantly affect diamond nucleation [145]. Substrate scratching was first reported by Mitsuda *et al.* in 1987 and since has become the most common pretreatment method for increasing diamond nucleation density [145]. There are two factors that enhance diamond nucleation density on substrates by diamond powder scratching. The surface micro-defects created by scratching can provide more diamond nucleation sites to bond with carbon atoms that have much lower energy than the original substrates. The other factor is that diamond powder particles that bombarded and seeded on the substrates by scratching could themselves be the nucleation sites. In this thesis, scratching was done by immersing substrate materials in an ultrasonic bath with a diamond powder suspension. A previous study conducted by our group revealed that the time of the ultrasonic scratching treatment significantly affected diamond nucleation [37]. An ultrasonic treatment time of 30 minutes was chosen for treating Cu-based substrates in this thesis. The size of

diamond powder used for scratching also affects the nucleation density of diamond formed at the early stages of deposition. Accordingly, nano-sized diamond powder (5 nm) was prepared for high nucleation density to obtain nanocrystalline diamond.

3.1.2.2 Sandblasting treatment of substrates

As discussed in Chapter two, substrate surface roughness has an influence on the adhesion of diamond thin films due to enhanced diamond nucleation and a mechanical interlocking effect. Sandblasting is an effective method to increase the roughness of the substrates to enhance the adhesion of diamond thin film on the substrates. In this thesis, oxygen-free Cu sheets (10 mm × 10 mm × 3 mm) were polished using sandpaper (#600 grid) and then ultrasonically cleaned in a 99% ethanol bath for 30 minutes. The cleaned Cu sheets were then sandblasted for 1 minute and further prepared for diamond deposition.

3.1.2.3 Al alloying treatment of substrates

Previous research shows that Al in the steel can prevent the formation of a graphite interlayer between diamond thin films and substrates, which therefore enhances diamond adhesion on Fe-based substrates [43]. Al would have similar effect on Cu-based substrates so, in this thesis, Al was alloyed into Cu to enhance diamond film adhesion on Cu substrates. The substrate materials used for diamond deposition were oxygen free Cu and two Cu–Al alloys with Al fractions of 1 and 3 at.%, respectively. The alloys were prepared by our collaborators in China using arc-melting method in which appropriate amounts of high-purity metals (99.999 at.%) of Cu and Al were repeatedly melted under a Ti-gettered inert atmosphere with non-consumable tungsten electrodes. The solidified alloy substrates were then machined into specimens 10 mm × 10 mm × 1 mm in size by wire cutting, mechanically polished with SiC sandpapers down to 600 # grid, and ultrasonically cleaned in ethanol for 10 min and then dried for use.

3.1.3 Substrates Prepared for FBHT Measurement

To measure the FBHT properties of the CNTs with a diamond interlayer, a micro channel Cu plate (Cu 145 alloy of 99.5 at.% Cu) was designed for the substrate. The Cu plate

was manufactured in the Physics Machine Shop, University of Saskatchewan. The Cu plate consists of top and bottom parts. The size of the top part is 20 mm × 25 mm × 8 mm and the bottom part is 30 mm × 35 mm × 5 mm. Figure 3.1 (A) depicts the Cu plate from the top and (B) is a picture of this Cu plate with a thermally insulating Teflon housing. A mini-channel 20 mm wide and 0.4 mm high was formed when the top plate was fixed to the housing. The diamond thin films and CNTs with a diamond interlayer were coated on the surface of the Cu plate for FBHT measurement.

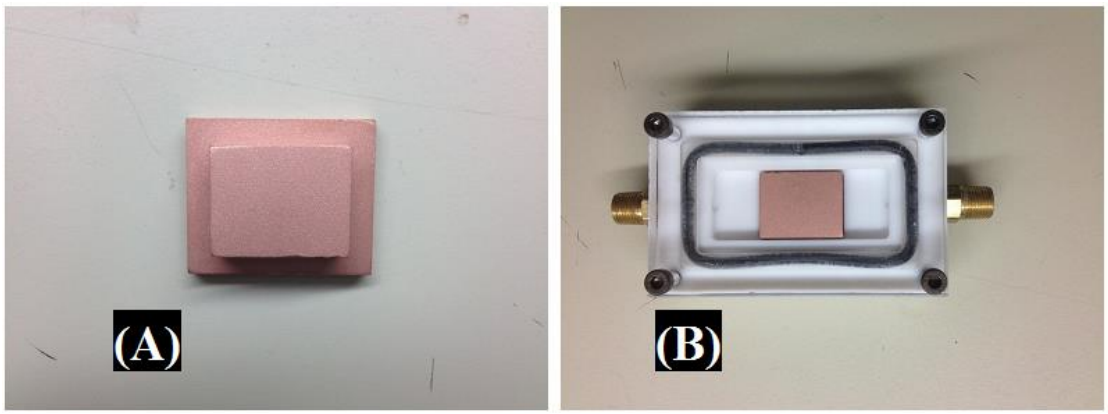

Figure 3.1. Top view of Cu plate (A) and polytetrafluoroethylene (PTFE) channel (B) for FBHT measurement.

3.2 Diamond Thin Film Deposition

3.2.1 HFCVD

In this thesis, some diamond thin film samples were deposited by HFCVD. Figure 3.2 is a picture of the HFCVD reactor. The main body of the HFCVD reactor is a cross-shaped glass chamber with a pumping system, a gas supply system, and a power supply system. In the chamber, a tungsten wire (diameter 0.3 mm) is coiled and heated to decompose the gases and create atomic H. To measure the substrate temperature, a thermocouple is connected to the back side of the substrate holder. The temperature of the substrate is controlled by adjusting the AC power output of the filament and the distance between the substrate and filament. For the substrate to have an appropriate diamond deposition temperature, Si substrates need a long distance (1 cm) to the filament due to their low thermal conductivity

while Cu substrates need a relatively short distance (0.5 cm) Due to their high thermal conductivity.

In the diamond deposition experiments, the chamber was first pumped to a pressure of 2 $\times 10^{-2}$ Torr by a rough pump, and then to a base pressure of 2 $\times 10^{-4}$ Torr by a diffusion pump. Thereafter, H_2 and CH_4 gases were introduced through a two-channel mass flow rate controller to a working pressure of ~20-30 Torr. The AC power applied to the filament was a voltage of ~30-40 V and a current of ~8-10 A. The typical temperature for diamond deposition measured by the thermocouple on the back side of the substrates was 770 K. The diamond deposition time ranged from one hour to several hours depending on the requirement for the film thickness. After deposition, the chamber was cooled down to room temperature in vacuum to prevent the oxidization of diamond. Finally, the sample was taken out for further characterization.

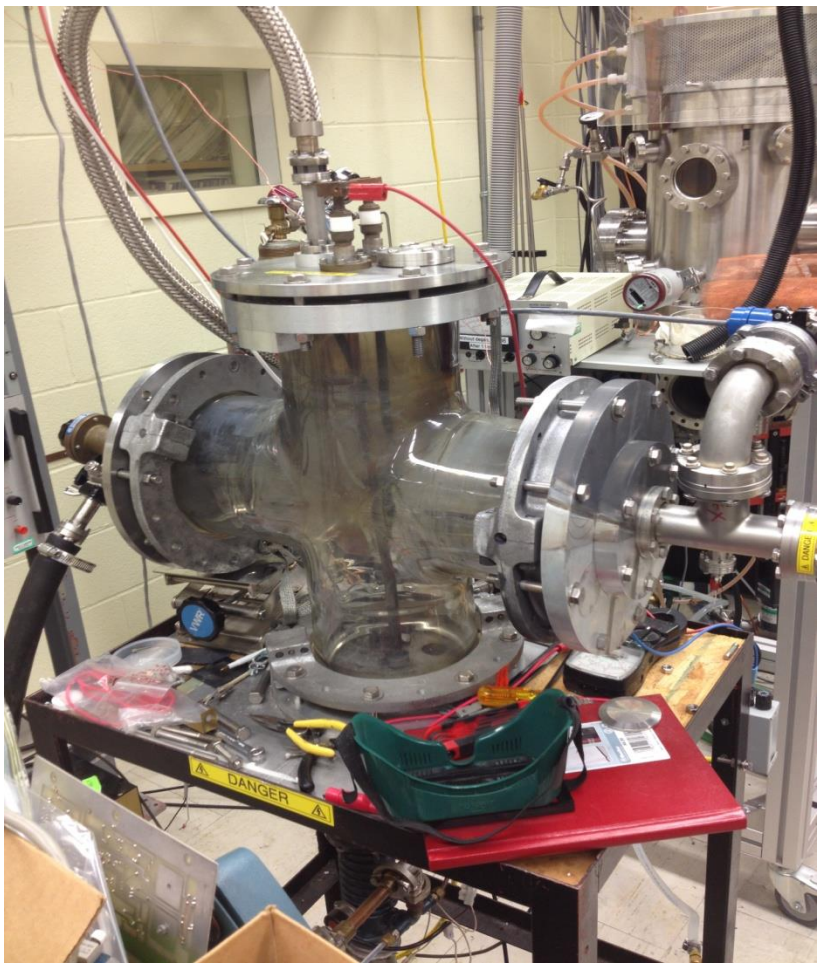

Figure 3.2. HFCVD reactor for synthesizing CNTs and diamond thin films.

3.2.2 MPCVD

All other diamond thin film samples were deposited by an MPCVD reactor. Figure 3.3 is a picture of the MPCVD reactor. It is an ASTEX-type (2.45 GHz 1100 W) reactor manufactured by Plasmionique Inc., and consists of a control system, a reactor chamber, a gas flow control system, and a pumping system.

For diamond deposition, a Mo or stainless steel plate was used as a substrate holder. Pretreated Cu or Si substrates were set on the substrate holder. The chamber was first pumped down to 1×10^{-2} Torr by a mechanical pump, and then to a base pressure of 1×10^{-6} Torr by a turbo pump. Gas mixture of H_2 and CH_4 mixture were then supplied to maintain a working pressure of 20 Torr and controlled by a two-channel mass flow rate controller. A plasma was then generated and tuned towards the substrate with a plasma output power of ~500-1200 W. Diamond deposition occurred at the surface of the substrates. The whole reaction could be observed through three quartz windows positioned on the side of the chamber. The position of the substrate was adjusted to minimize the plasma reflection. The deposition time ranged from three hours to more than ten hours. The diamond growth rate by MPCVD was lower than by HFCVD due to the lower substrate temperature and, accordingly, required a longer time. After deposition, the substrates coated with diamond thin films were cooled down to room temperature in vacuum to prevent oxidization of diamond, and then taken out for further characterization.

Figure 3.3. MPCVD reactor for synthesizing diamond.

3.2.3 Diamond Thin Films with Different Grain Sizes and CH_4 Concentrations

To obtain diamond thin films with different grain sizes, one group of diamond thin film deposition samples were pretreated with micro-diamond powder (1 μm) seeded on substrates and the other groups of diamond deposition samples were pretreated with nano-diamond powder (5 nm) seeded on substrates. Diamond thin film deposition was performed by HFCVD using identical conditions to those described above. The deposition time for the micron-diamond film and nano-diamond film were 5 hours and 2 hours, respectively.

To deposit diamond thin films with different sp^2 contents, the experiments were carried out using CH_4 (1 vol.% and 5 vol.%) and H_2 (99 vol.% and 95 vol.%) precursor gases with a total flow rate of 50 sccm. The 1 vol.% CH_4 samples represent low sp^2 content diamond thin

films while 5 vol.% samples denote high sp^2 content diamond thin films. All other deposition procedures are the same as described in §3.2.1.

3.3 CNT Deposition

3.3.1 Catalysts Preparation

It is commonly believed that CNT deposition requires catalysts such as iron, nickel, cobalt, or compounds thereof [146]. Iron has been commonly used as a catalyst for CNT growth due to its low cost and easy preparation. In this thesis, two methods were adopted for preparing the iron catalyst: spin-coating and sputtering.

3.3.1.1 Catalyst spin-coating for CNT deposition

The catalysts (Fe) for CNT growth were prepared by spin coating of ferric nitrate solution (0.1 mol/L) and followed by heat treatment in which a high speed spinning disc (over 900 revolutions per minute or rpm) was used. 0.05 ml of ferric nitrate solution was firstly cast on the diamond thin film surfaces and then spin-coated for durations of 30, 60, 90, and 120 seconds, respectively, in order to make ferric nitrate liquid layer with different thickness. During the spinning, part of the solution will be span off the surface due to the centrifugal force and thus the liquid layer thickness decreases with the increase of spinning time. After the spin-coating, the samples were heated in a thermal furnace at a temperature of 573 K for 2 hours to form Fe particles on the surface of diamond thin films to catalyze CNT growth. The Fe particle density formed decrease with the increase of the spin time due to the decrease of solution layer thickness. Those catalyst coated samples were then put into hot filament reactor for CNT growth.

3.3.1.2 Catalyst sputtering for CNT deposition

Sputtering is a powerful technique to obtain small size particles on the substrates [69]. It takes accelerated ions to sputter target to form small debris bombard on the substrates. The sputtering requires a vacuum environment to prevent air molecules from scattering the sputtering ions. The HFCVD system could easily accommodate the sputtering device and supply the required vacuum. To investigate the CNT growth model, a group of catalysts were

prepared by sputtering in the HFCVD system. In the chamber, DC power was supplied between the filament and the target. The filament was set as the anode while the iron target was set as the cathode. The system was first pumped down to 1×10^{-4} Torr and then filled with Ar gas. The diamond coated samples were sputtered at -700 V for 1 hour. After that, CNT deposition was carried out in the same system.

3.3.2 CNT Deposition by HFCVD

CNT deposition was carried out in the HFCVD system. The diamond coated sample with prepared catalysts was first placed onto the substrate holder. Then, the chamber was pumped down to a pressure of 1×10^{-2} Torr by a mechanical pump and then a base pressure of 1×10^{-4} Torr by a diffusion pump. CH_4 and H_2 mixture gas (10:40 v/v) was supplied by a two-channel mass flow rate controller and the chamber was maintained at a pressure of 20 Torr. AC power was applied to the filament with a voltage of ~30-40 V and a current of ~8-10 A. A DC bias was used for assisting aligned CNT growth with an applied voltage ranging from -400 to -700 V. The CNT deposition time was one hour, and the back side temperature of the substrate holder as measured by thermocouple was 723 K.

3.4 Characterization of the Microstructures

3.4.1 SEM

In this thesis, a JEOL JSM-6010 SEM, shown in Figure 3.4 and located in the Department of Mechanical Engineering, University of Saskatchewan, was used to observe the surface morphology of the CNTs and diamond thin films. This SEM has two detectors for both Secondary Electron Imaging (SEI) and Back-scattered Electron Imaging (BEI). In this thesis, SEI mode was mostly used to characterize the surface morphology of the CNTs and diamond thin films. The surface roughness of the Cu substrates before and after sandblasting treatment was observed using this mode, and the nucleation density of diamond on Cu substrates with or without sandblasting treatment was also observed. The thickness of the diamond thin films could be measured from a cross-sectional observation and the diamond growth rate could be calculated. The density of the CNT arrays was also determined. Some

other information about the samples was obtained using BEI mode. For example, the BEI detector could show the catalyst location in the CNTs. In this mode, the iron catalyst has a higher brightness while CNT bodies are dark due to the element weight difference between carbon and iron. Thus, the color difference indicates the location of the catalysts and the CNTs.

Figure 3.4. JEOL JSM-6010 SEM used in this thesis.

3.4.2 TEM

TEM observations of CNTs were carried out on a Philips CM10 located in the Department of Biology, University of Saskatchewan (Figure 3.5). The resolution of this TEM is 0.5 nm, and the magnification range is ~20-450000×. The TEM was used to observe the location of the catalyst in the CNTs to identify the CNT growth model. For the sample preparation, The CNT specimens were scratched from the substrates and dispersed in ethanol by an ultrasonic bath. Then the specimen suspension was dropped on a Cu grid for TEM observation. TEM observations of diamond on Cu alloys were performed in the Shenyang National Lab of Material Science, Institute of Metal Research, Chinese Academy of Science, to understand the interfacial structure between the diamond thin films and the Cu substrate and their chemical states. A Tecnai G^2 F20 transmission electron microscope, equipped with a High-Angle Angular-Dark-Field (HAADF) detector and Energy-Dispersive X-ray spectrometer (EDX) systems, was used at 200 kV for electron diffraction analysis and chemical composition analysis. Cross-sectional specimens for TEM observations were prepared by sequential procedures including cutting using Iso Met 5000, gluing using EM TXP, , and dimpling using VCR D500i to 15 μm in thickness, then finally ion-milling (LKY-AB) by Ar+ from both sides until some perforation appeared.

Figure 3.5. Philips CM10 TEM used in this thesis.

3.4.3 Raman Spectroscopy

Raman spectroscopy was used to characterize diamond and CNTs and measure the sp^2 and sp^3 phase content in diamond. The sp^2 and sp^3 measurements were carried out using a Renishaw micro-Raman system 2000 spectrometer (Figure 3.6) located at the Saskatchewan Structure Science Center (SSSC), University of Saskatchewan with a 514 nm laser wave length.

Figure 3.6. 514 Renishaw micro-Raman used in this thesis.

3.4.4 Synchrotron-based X-ray Absorption Spectroscopy

The electronic states of the Al-modified Cu substrate and diamond thin films were measured using the High Resolution Spherical Grating Monochromator (SGM) beamline at the Canadian Light Source Inc. (CLS), University of Saskatchewan. Synchrotron based X-ray near-edge fine structure absorption spectroscopy (XAS) was performed to address the electron configuration changes of copper.

3.5 Characterization of Properties

3.5.1 Residual Stress Measurement

Diamond thin film coatings usually have internal (residual) stress after CVD deposition. In this thesis, the internal stress of the diamond thin film coatings was measured by Raman spectroscopy and XRD. XRD measurements were carried out using a Rigaku Geigerflex diffractometer (Figure 3.7) located in the Plasma Physics Lab, University of Saskatchewan. A Co target was used with a scanning range from 0 to 120 °and a scan step of 0.02 °.

Figure 3.7. XRD equipment used in this thesis.

3.5.2 Adhesion testing

Vickers hardness indentation testing was used to test the adhesion between the diamond thin film and the Cu substrate. The Vickers hardness test was conducted on a MVK-H1 Mitutoyo instrument located in the Materials Science Lab, Department of Mechanical Engineering, University of Saskatchewan (Figure 3.8). Vickers hardness indentation testing was used to test the adhesion between the diamond thin film and the Cu substrate. The indentation was performed on the surface of the diamond thin film adhered to the Cu substrate. The indentation load was 100g and the duration of each indentation was 10 seconds. A continuous diamond thin film without delamination or cracks after indentation indicates good adhesion between the diamond thin film and the Cu substrate.

Figure 3.8. Vickers hardness tester used in this thesis.

3.5.3 FEE Measurement

FEE measurement was performed on a Keithley 237 high voltage measuring unit (Figure 3.9) using a diode configuration inside a vacuum chamber at a pressure of 1×10^{-7} Torr. The Keithley 237 high voltage measuring unit is a programmable device that can measure the voltage and current. Figure 3.10 is a schematic representation of this device. The samples were set as the cathode and a stainless steel pin with a diameter of 1 mm was the anode. The separation between the anode and cathode was 30 μm. Under this condition, a breakdown voltage calculated by equation 2.20 is over 3000 V, while the FEE measurement voltage is below 1000 V (far below the breakdown voltage). I-E (current verses electric field) curve and F-N plot of the sample can be calculated by Labview software. For FEE stability testing, a specific voltage (electric field) were applied to the emitters to have the same starting emission current of 30 μA and the variation of the current with time was recorded.

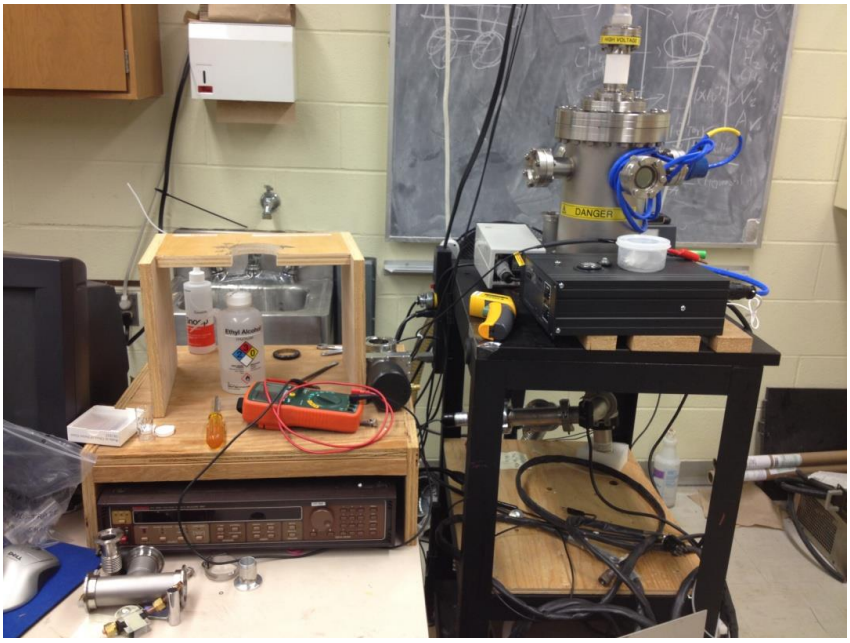

Figure 3.9. Keithley 237 high voltage measuring unit for FEE measurement.

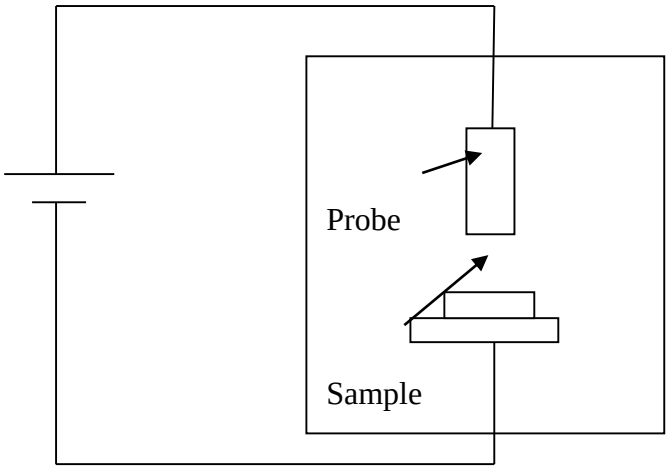

Figure 3.10. Schematic of the FEE measurement device.

3.5.4 FBHT Measurement

To measure the FBHT performance of CNTs with a diamond thin film interlayer on Cu, the experiment was set up as follows. CNTs with a diamond thin film interlayer coated Cu block were inserted into a PTFE channel from the back side (Figure 3.11). At the inlet and outlet of the mini-channel, cavities were provided to create a uniform flow through the channel. The testing plate was heated using 750 W two-cartridge heaters inserted into the Cu

block (dimensions of 30 mm × 35 mm × 175 mm). The heating rate of the heater was controlled by a 2000 W auto transformer. Along the length of the channel, three J type thermocouples were inserted, located 1.5 mm below the top surface of the block, for measuring the surface temperature. For measuring the temperature gradient, two 1 mm diameter metal insulated J-type thermocouples were inserted in the testing section, 1.5 mm apart in the vertical direction. The water inlet and outlet temperatures were measured using J type thermocouples. The instantaneous temperatures measured by the thermocouples were digitized using a data logger. All thermocouples were calibrated using a constant temperature water bath. A thick layer of glass wool insulation was provided to prevent heat loss to the surroundings. A schematic of these components is shown in Figure 3.11. The experimental setup is shown in Figure 3.12. Prior to the experiment, the water was boiled vigorously for 30 minutes to remove dissolved gases. Water flow was supplied by a pump at a temperature maintained at 90 ℃ using a water pre-heater. Heat was supplied to the testing plate in small increments by two electrical cartridge heaters inserted in the Cu block. Once the Cu block reached a steady state temperature, temperature data from the thermocouple were record by a data logger (Data taker, DT 85) data acquisition system. The experiment was repeated for different heat fluxes until the CHF was encountered, as identified by an abnormal temperature rise in the heater. The occurrence of the CHF can be identified by following phenomena: (a) backflow of vapor towards the inlet section, (b) sudden increase in surface temperature due to drying out of the surface, (c) and fluctuation of inlet temperature due to the backflow of vapor [147]. Flow boiling experiments were conducted for mass fluxes of 283, 348, and 427 kg/ m^2s using demineralized water as the working fluid. The water inlet temperature at the entry of the testing section was maintained at 90 ℃. The amount of heat flux supplied to the water by the Cu heating block was calculated using equation 3.1,

$$q=-K\frac{T1-T2}{\Delta X} \quad , \tag{3.1}$$

where q is heat flux (W/m^2), K is the thermal conductivity of Cu (W/m K), T_1 and T_2 are the temperatures measured from the heating section in the vertical direction (℃), and Δ x is the vertical distance between the thermocouples.

The FBHT coefficient could be calculated from the heat flux and the average surface and wall temperatures using equation 3.2 [148],

$$h = \frac{q}{T_s - T_f} \ , \tag{3.2}$$

where h is the FBHT coefficient, q is the heat flux, and T_s and T_f are average surface and wall temperatures, respectively.

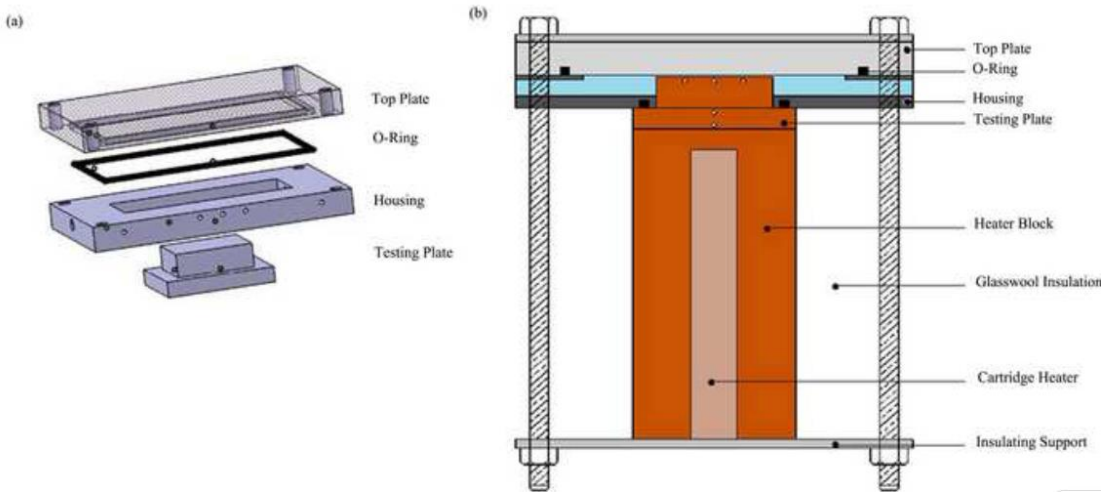

Figure 3.11. Schematic of the FBHT measurement components.

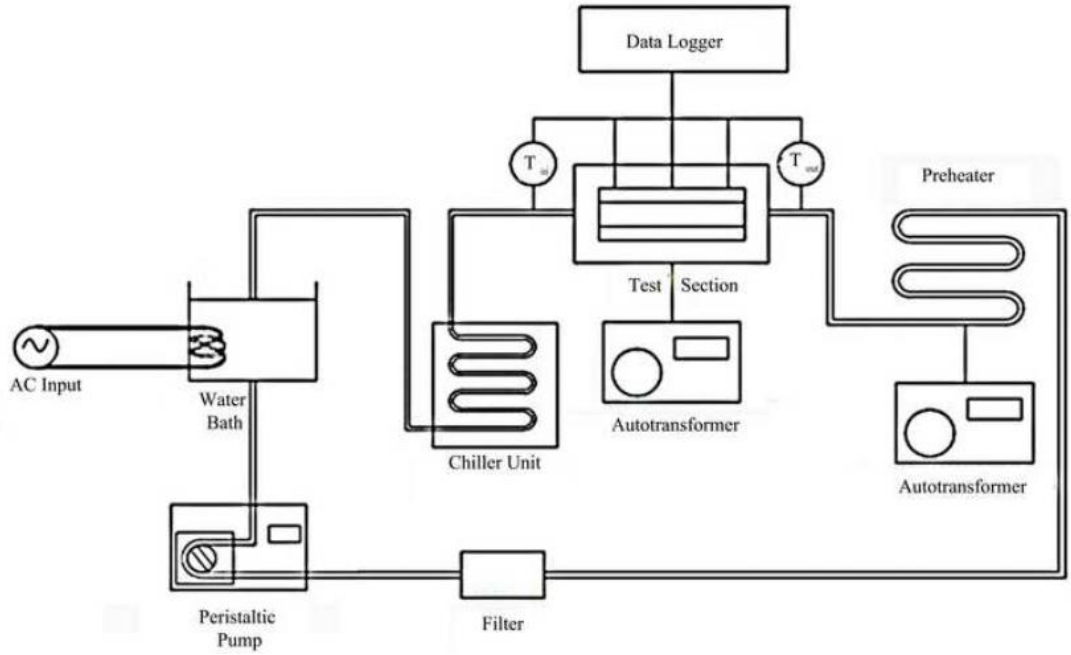

Figure 3.12. Schematic of the FBHT measurement experimental setup.

FBHT stability testing was done by measuring subcooled flow boiling curves of CNTs with a diamond interlayer coated Cu surface at mass fluxes of 89 and 283 kg/m^{2}s, respectively. The mass flux of 89 kg/m^{2}s was chosen to analyze the FBHT stability of the material at a lower low mass flux. The time for each measurement was one hour, followed by a cooling stage of approximately 20 hours. Each measurement was repeated four times on the same sample to assess repeatability.

CHAPTER 4

IMPROVEMENT OF DIAMOND ADHESION ON CU SUBSTRATES

In this chapter the results of various experiments on improvement of diamond adhesion to Cu substrates is being presented and discussed.

4.1 Effect of Sandblasting Treatment on diamond adhesion

As discussed in Chapter two, diamond thin film adhesion can be enhanced by treatment of the substrate surface, for example, increasing the roughness. Sandblasting is an effective way to increase roughness of the substrate. Figure 4.1 shows SEM images of the surface morphology of untreated and sandblasted Cu substrates before diamond deposition. It can be seen that the surface roughness of the Cu substrates significantly increased after sandblasting treatment. Table 4.1 presents the surface roughness values (Ra) measured by Mitatoyo Suftest.211 roughness measurement device. The average roughness values increase from 0.28μm to 2.00μm after sandblasting treatment.

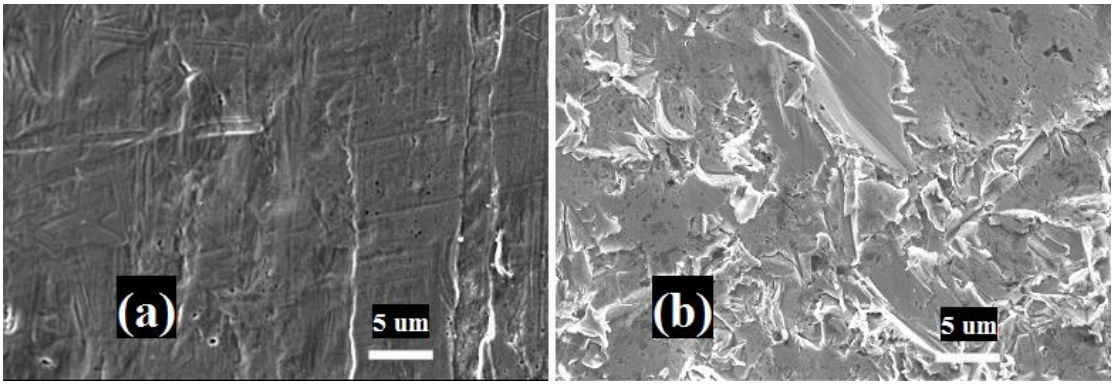

Figure 4.1. SEM images (SEI mode) of (a) untreated Cu and (b) sandblasted Cu.

Table 4.1 Surface roughness of copper substrate before and after sandblasting.

	Roughness (μm)
Copper substrate before sandblast	0.28 ± 0.01
Sandblasted copper substrate	2.00 ± 0.01

Figure 4.2 shows SEM images of diamond thin films deposited on Cu substrates without sandblasting treatment. The diamond thin films partially peeled off the substrate before the application of any force, which indicates poor adhesion. Figure 4.2 (a) shows that some cracks form in the diamond thin film due to the thermal stress resulting from cooling of the substrate following diamond deposition. There is a significant thermal expansion mismatch between diamond and Cu; after cooling down from a high deposition temperature, the Cu substrate shrinks substantially while the diamond thin film contracts much less. High stress develops between the substrate and the coating so cracks in the diamond thin film appear. Our results agree well with previous reports that showed poor adhesion of diamond thin films on Cu substrates [39]. Unlike carbide forming metals, such as Cr and Ti, Cu cannot form any carbide during the CVD growth of diamond. As a result, the diamond nucleation density on Cu is usually lower than on carbide forming metals, giving rise to insufficient contact area between the diamond layer and the substrate. In addition, Cu has almost no affinity for diamond, resulting in no bond formation between the Cu and the diamond. Therefore, the adhesion of diamond to untreated Cu substrates is usually poor.

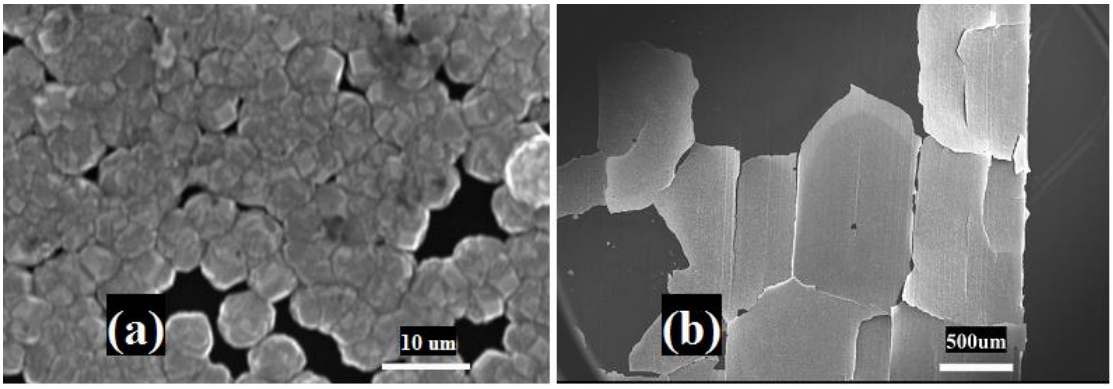

Figure 4.2. SEM images (SEI mode) of diamond thin films on untreated Cu at (a) high magnification and (b) low magnification.

Figure 4.3 shows the surface morphology of diamond thin films deposited on sandblasted Cu substrates for short (3 hours) and long (5 hours) growth periods. It can be seen that with a short growth time, the diamond thin film has a nanocrystalline structure and is porous and noncontinuous. After a longer deposition time, the diamond thin film becomes

denser and more continuous; there are no cracks or film peeling observed even for the thicker diamond thin film. The diamond films shown in Figure 4.3(b) illustrates the growth of secondary diamond nucleus, consistent with the results reported by Lu et al [104]. In Figure 4.3 (a), the density of diamond nanoparticles is fairly high, indicating a high diamond nucleation density. Normally, it is difficult to have diamond nucleation on Cu and the nucleation density is low [39]. Therefore, the sandblasting method used in this study clearly enhanced the diamond nucleation density on Cu substrates. The enhanced diamond nucleation density could increase the diamond thin film adhesion strength on Cu substrates. The thick diamond film in Figure 4.3 (b) has no obvious cracks or breaks due to good adhesion on the Cu substrate. Therefore, the SEM results show that the sandblasting treatment increased both the diamond nucleation density and adhesion to the Cu substrate.

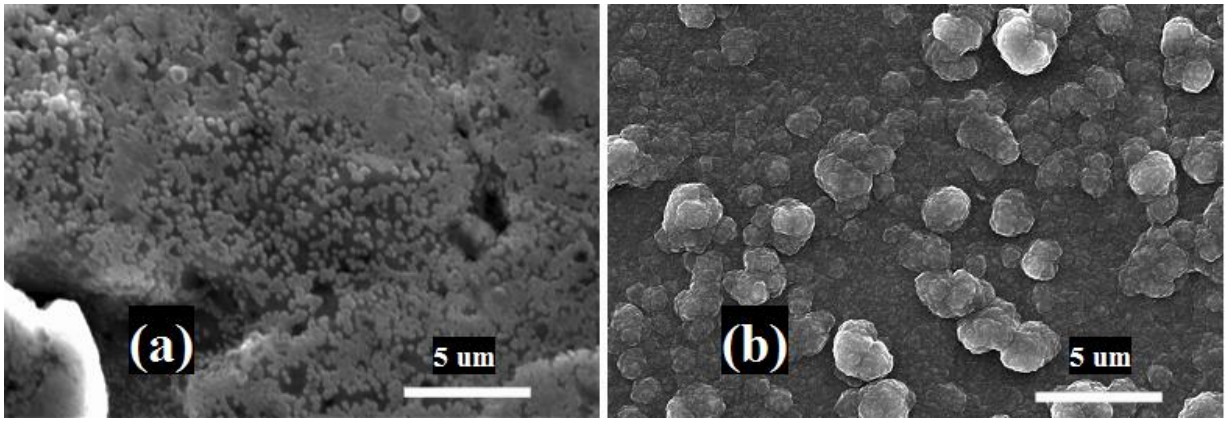

Figure 4.3. SEM images (SEI mode) of diamond thin films grown on sandblasted Cu for (a) 3 hours and (b) 5 hours.

As shown in Figure 4.1 and Table 4.1, sandblasting treatment increases the roughness of the Cu substrate surface and created some defects. These defects can provide extra nucleation sites for diamond growth, resulting in a higher diamond nucleation density and the formation of a nanocrystalline structure (see Figure 4.3) instead of a microcrystalline structure (see Figure 4.2). The increased surface roughness caused by sandblasting increases the contact area between the diamond thin film and the Cu substrate, which enhances the adhesion strength. Additionally, the rough surface can also cause mechanical interlocking and thus

increase the adhesion properties of the diamond thin films [149]. The strong adhesion between the diamond thin film and the sandblasted Cu substrate was confirmed by Vickers indentation testing under a load of 100 g, as shown in Figure 4.4. There is no coating delamination observed around the indent which indicates a good adhesion between the diamond thin film and the Cu substrate.

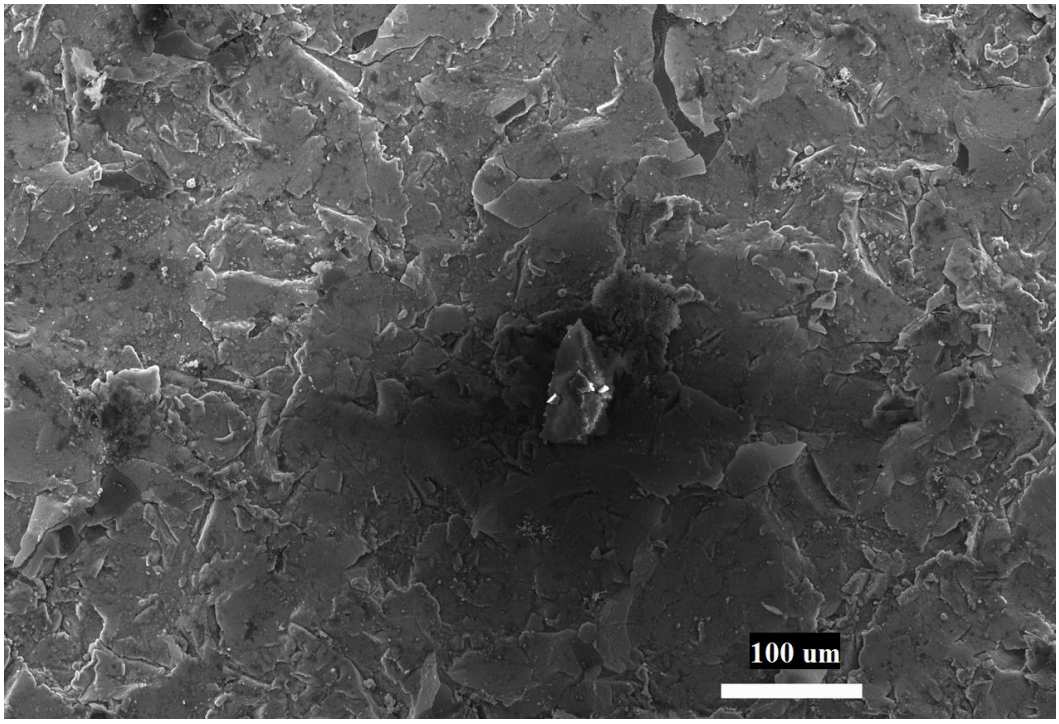

Figure 4.4. An SEM image (SEI mode) of a diamond thin film on sandblasted Cu after indentation.

Figure 4.5 shows XRD patterns of diamond thin films coated on sandblasted Cu. In Figure 4.5 (a), the diamond thin film created after 2 hours of deposition has a nanocrystalline structure and is porous and noncontinuous (Fig. 4.3 (a)). The diffraction peaks at 51.7 °, 60.1 °, and 90.3 ° originate from the (111), (200), and (220) planes of Cu, respectively. The peaks of the nanodiamond thin films are insignificant and overlap with the Cu signals. After 5 hours of deposition time, the diamond thin films are dense and continuous without cracks and peeling (Fig. 4.3 (b)). Peaks at 51.1 °, 59.7 °, and 89.1 ° are diffractions from the (111), (200), and (220)

planes of diamond, respectively. The diamond peaks are quite strong and cover the Cu peaks. The strong diamond XRD patterns demonstrate the presence of thick diamond thin films on Cu substrates after 5 hours of deposition. These peaks have a slight downward shift due to the higher compressive stress of the diamond films. The existence of this stress suggests sufficient adhesion strength between the diamond thin film and the Cu substrate to prevent the diamond thin film from cracking or peeling.

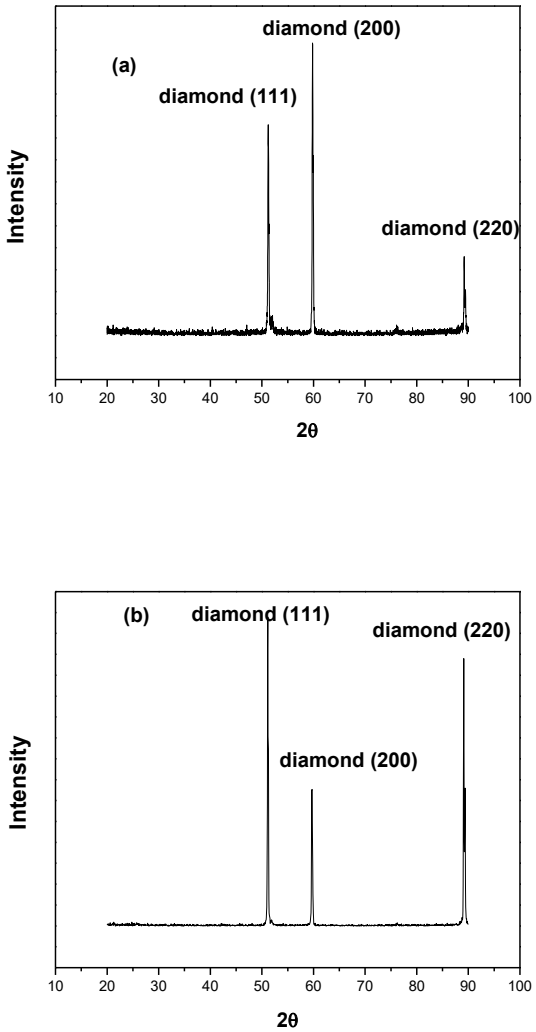

Figure 4.5. XRD patterns of diamond grown for (a) 2 hours and (b) 5 hours on sandblasted Cu.

Figure 4.6 shows the Raman spectra of diamond thin films deposited on Cu substrates. The spectrum of the diamond thin film on the non-treated Cu substrate (Figure 4.6 (b)) features a typical diamond peak at 1332 cm^{-1} while the peaks from diamond thin films on sandblasted Cu substrates are shifted to 1338 cm^{-1} (5 h; Fig. 4.6 (a)) and 1335 cm^{-1} (3 h; Fig. 4.6 (c)), respectively. The up-shift of the diamond peak from its typical position is caused by residual compressive stresses accumulated in the diamond thin films. This shift can also be considered as an indication of good interfacial bonding between the diamond film and the substrate. Once the diamond thin film detaches from the substrate and becomes free-standing, such as on the non-treated Cu substrate, the internal stress is released and the Raman spectrum peak returns to its typical position at 1332 cm^{-1} (see Fig. 4.6 (b)).

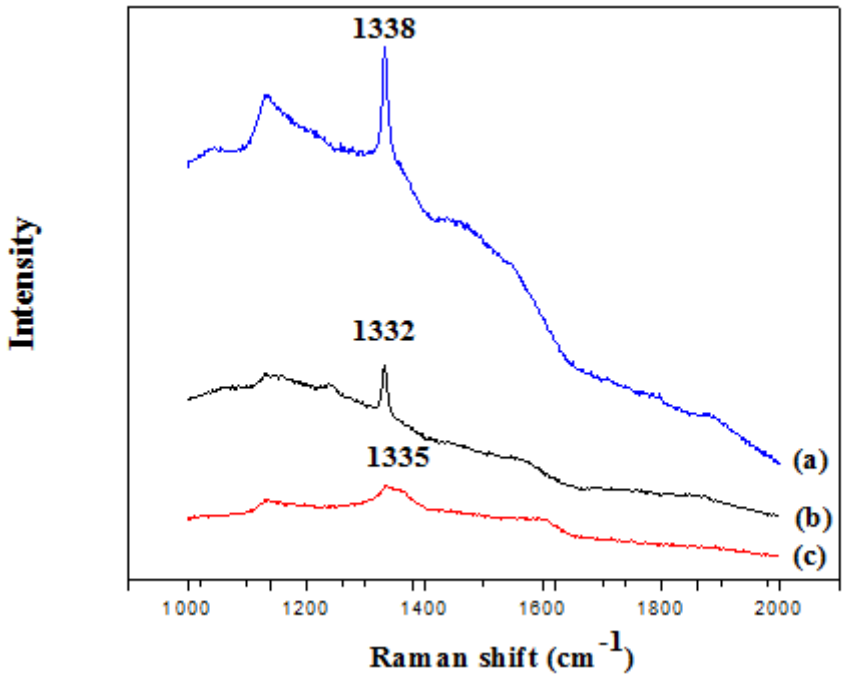

Figure 4.6. Raman spectra of diamond thin films on (a) sandblasted Cu substrate after 5 hours deposition; (b) non-treated Cu substrate after 5 hours deposition; and (c) sandblasted Cu substrate after 3 hours deposition.

4.2 Effect of Al Alloying on diamond adhesion

Figure 4.7 (a,b) shows the surface morphologies of diamond thin films formed on pure Cu after a 15 hour MPCVD process in a H_2-CH_4 (99:1, v/v) plasma atmosphere. The diamond film covered the whole surface of the Cu substrate at first, but then started to buckle, crack, and spall during the cooling process, resulting in a discontinuous diamond film on a partially exposed substrate surface. Moreover, the residual diamond film on the Cu substrate still shows weak interfacial adhesion. It can be easily scratched from the substrate using tweezers, or even spall off the substrate on its own. The Raman spectrum of the residual diamond film in Figure 4.7(c) shows the characteristic sharp peak of diamond at 1332 cm^{-1}. However, the spectrum from the exposed substrate surface shows typical features of graphitic and/or amorphous carbon, as indicated by the two peaks centered at 1350 cm^{-1} (D band) and 1584 cm^{-1} (G band). The relatively low intensities of these peaks are closely associated with the small quantity of non-diamond carbon formed on the substrate surface. Nonetheless, the formation of this intermediate graphite layer is believed to markedly deteriorate the interfacial bonding strength of the diamond thin films [43].

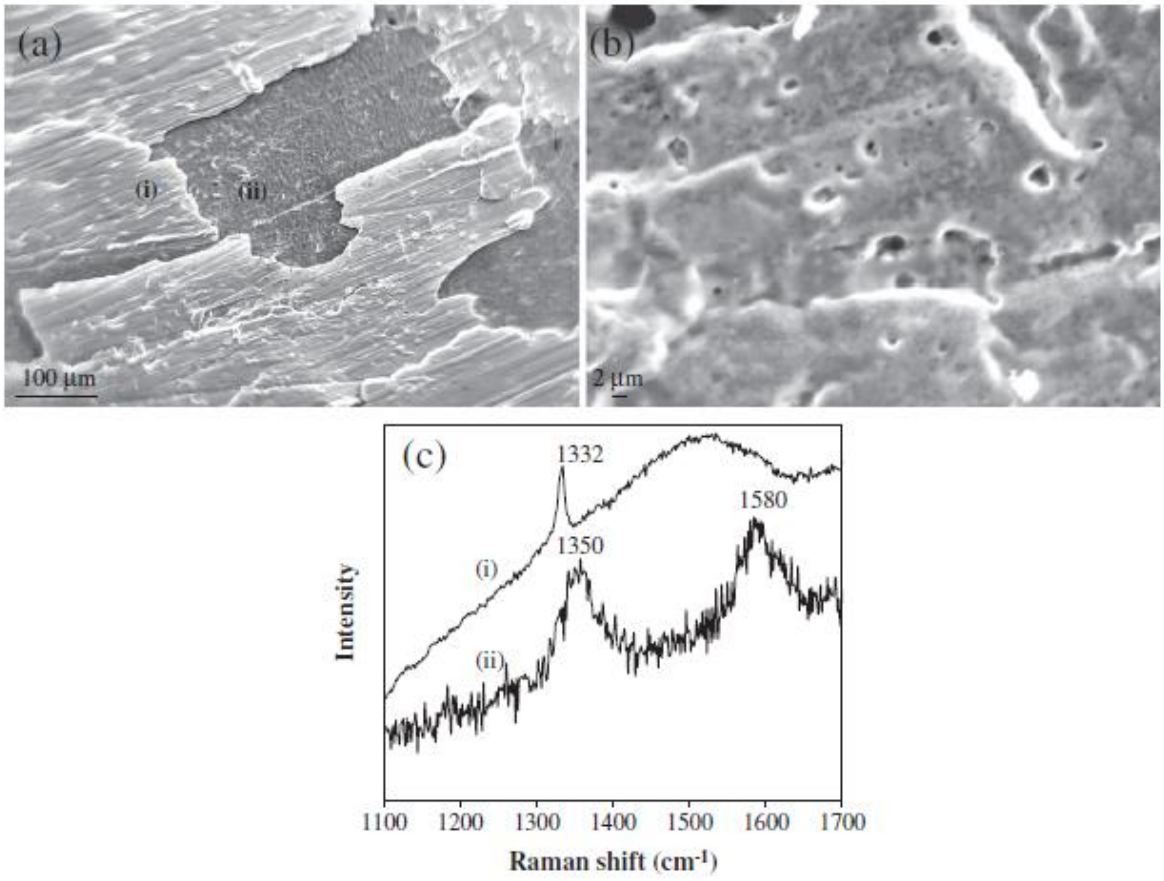

Figure 4.7. SEM images (a,b) in SEI mode and the corresponding Raman spectra (c) of diamond thin films on pure Cu substrates.

It has been reported that Al alloying on Fe-based alloys can significantly promote the formation of adherent diamond films. In this study, diamond deposition on Al-modified Cu substrates was investigated.

Diamond thin films have been deposited on Cu substrates with the addition of 1 (Cu-1Al) and 3 (Cu-3Al) at.% Al, respectively. Following Al addition to the Cu substrate, diamond deposition was significantly improved. Although the diamond film that formed on the Cu–1Al substrate still sustained local spallation, the residual diamond film became more difficult to remove from the substrate surface. In contrast, the diamond film formed on the Cu–3Al substrate displayed less interfacial delamination and a continuous and adherent diamond film remained over a larger surface area. Figures 4.8 (a) and (b) show the surface morphologies of the diamond films deposited on the Cu–3Al substrates, which display a dense structure

consisting of well faceted diamond micro-crystallites. Figure 4.8 (c) is the Raman spectrum of the diamond film, which exhibits a distinctive diamond peak centered at approximately 1337 cm^{-1}. The up-shift and broadening of the diamond peak from the typical position at 1332 cm^{-1} is caused by residual compressive stresses accumulated in the diamond film. This shift can be considered an indication of good interfacial bonding between the diamond film and the substrate. Once the diamond film detaches from the substrate and becomes free-standing, such as after indentation testing, the internal stress is released and the Raman peak returns to the typical position at 1332 cm^{-1}.

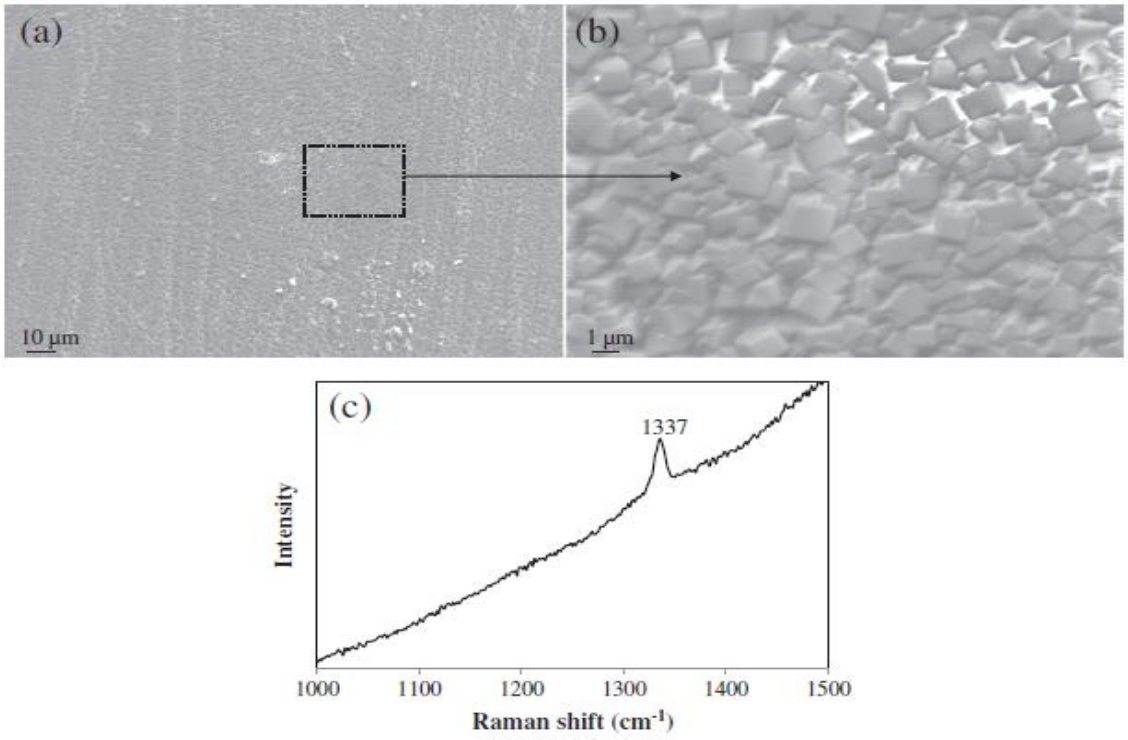

Figure 4.8. SEM images (SEI mode) of Cu-3Al substrate coated with continuous microcrystalline diamond film: (a) general view; (b) magnified view; (c) corresponding Raman spectrum.

To better understand the enhanced film adhesion in terms of the changes in interfacial chemistry, typical Cu–Al samples with local spallation of diamond films were selected and the exposed Cu–Al substrate surfaces analyzed by Raman spectroscopy, as shown in Figure 4.9. A slight signature of non-diamond carbon is still detected on the surface of the Cu–1Al

substrate, but has completely disappeared in the case of the Cu–3Al substrate surface. This comparison clearly reveals that an increased aluminum concentration in the Cu substrate is beneficial with respect to suppressing the formation of non-diamond carbon species, and is considered to be a critical factor for the enhanced interfacial bonding of diamond film on the Cu–Al substrate.

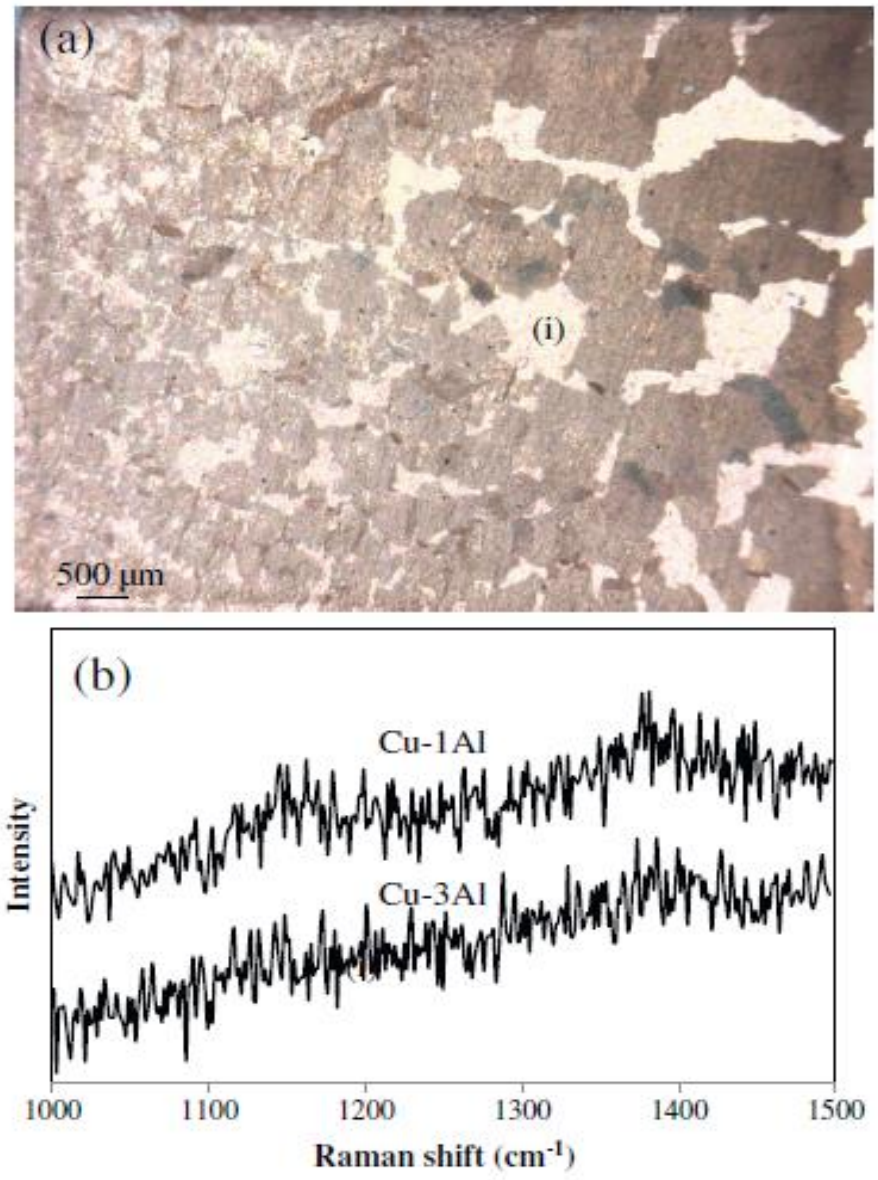

Figure 4.9. Optical micrograph of Cu–1Al covered with partially spalled diamond film (a), and the corresponding Raman spectra (b) measured from the exposed substrate surface, marked as i; spectrum measured from exposed Cu–3Al substrate surface is provided for comparison.

Figure 4.10 displays a typical cross sectional TEM image of the diamond film grown on the Cu–3Al substrate in a H_2–CH_4 (99:1, v/v) gas mixture, with the diamond film and Cu substrate being clearly identified by Selected Area Electron Diffraction analysis (SAED). The diamond film adheres well to the Cu substrate without obvious interfacial separation. In most interfacial regions, an intermediate layer forms at the interface between the diamond film and the Cu–Al substrate, where the intermediate layer does not exhibit any diffraction patterns.

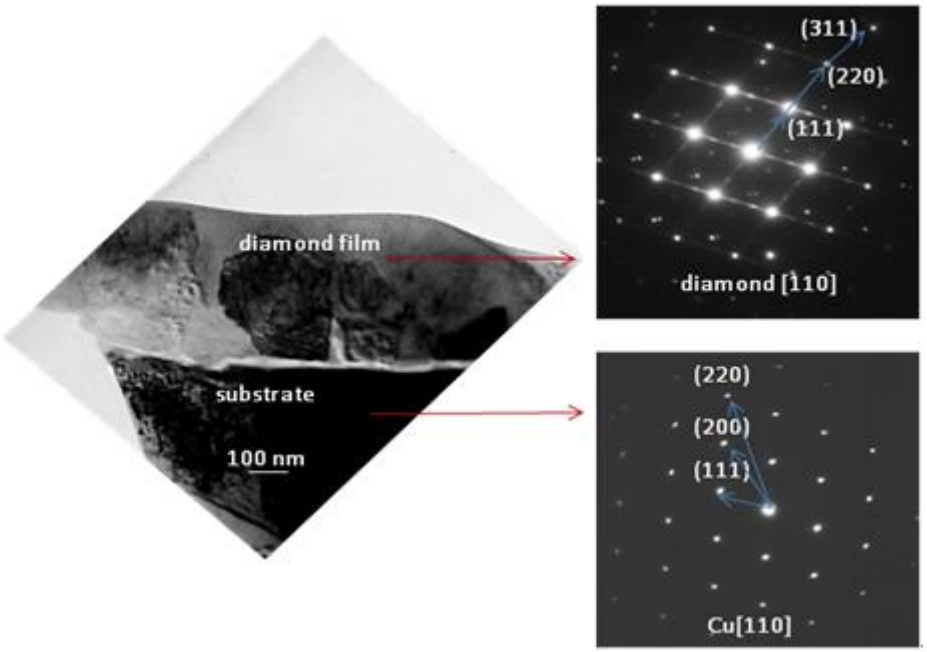

Figure 4.10. Cross sectional TEM image (bright field) of diamond film grown on Cu-3Al substrate and the corresponding SAED patterns.

A Tecnai G^2 F20 TEM, equipped with High-Angle Angular-Dark-Field (HAADF) detector and Energy-Dispersive X-ray spectrometer (EDX) systems, was used at 200 kV for electron diffraction analysis and chemical composition analysis. An EDX line-scan depth profile of the major components, spanning from the diamond film down to the near surface of the substrate (as indicated by the arrow in Figure 4.11a), demonstrates that there is insignificant oxygen inclusion in the diamond film, but its concentration substantially increases at the interface location (Fig. 4.11b). The same trend is also observed on aluminum. The comparison of EDX point analysis measured at the interface and near-surface regions of

the substrate clearly confirm the simultaneous enrichment of oxygen and aluminum at the interface. It is preliminarily concluded that an aluminum-rich oxide sub-layer, normally showing an amorphous structure, formed at this interface zone.

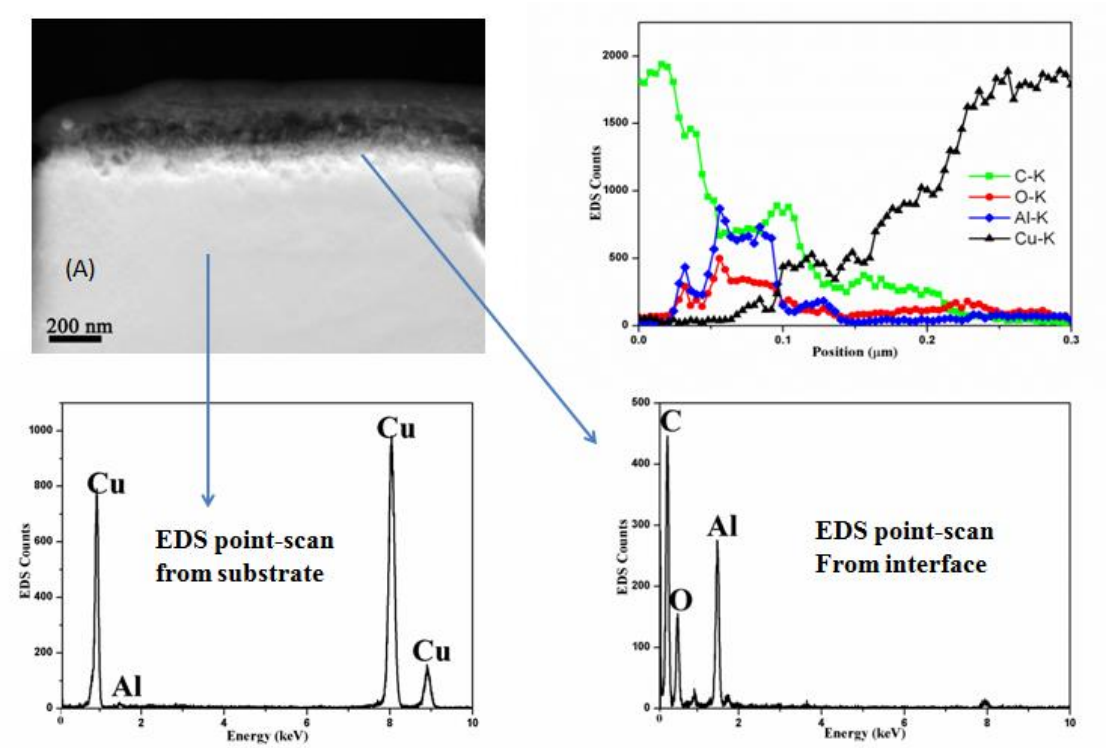

Figure 4.11. Cross sectional HAADF image (bright field) of diamond film grown on Cu-3Al substrate prepared with H_2-20 vol.% CH_4 and EDX line-scan depth profile and point analysis around the diamond substrate interface.

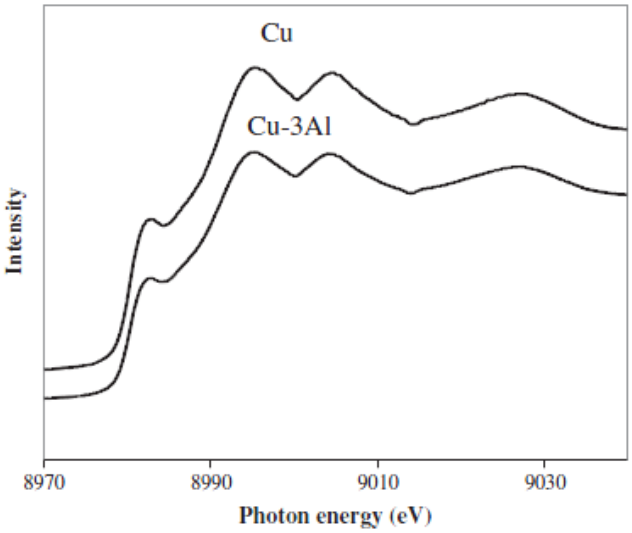

Figure 4.12. Synchrotron X-ray Cu K-edge absorption spectra (TEY mode) measured from clean pure Cu and Cu-3Al substrate.

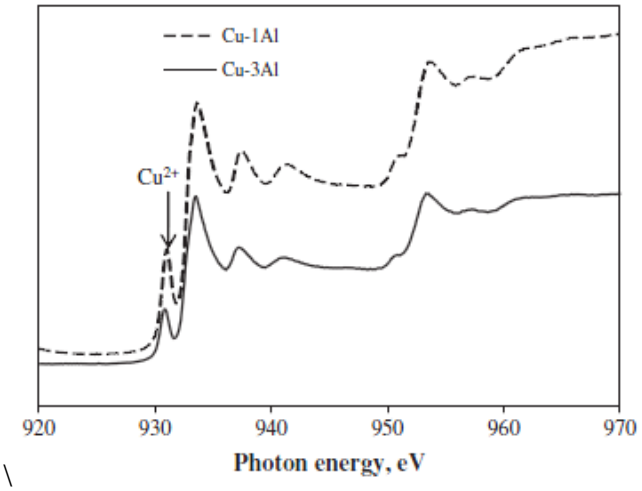

Figure 4.13. Synchrotron X-ray Cu L-edge absorption spectra (TEY mode) measured from air-oxidized Cu-1Al and Cu-3Al substrates at 650 ℃, showing formation of Cu oxide.

The diamond deposition behavior on the Al-modified Cu substrate is somewhat similar to that investigated for Al-containing Fe-base alloys [43, 150]. In those studies, slight Al modification improved the adhesion of diamond thin films on the Fe-based alloys. The Al addition is effective due to its inhibition of a graphite phase by the formation of an intermediate amorphous alumina barrier layer on the substrate surface, which ultimately enhances the adhesion of the diamond thin film. However, due to the nature of the different

substrates, a number of distinctive deposition features were observed for the current Cu substrates in comparison with previous Fe-based alloy substrates under investigation. For a long time, the transition metals Fe, Co, Ni and their alloys have been known to possess strong catalytic ability for the preferential formation of graphite. These materials usually suffer from severe carburization and metal dusting attack during exposure to high temperature carbonaceous environments [151]. The catalytic properties of these transition metals are closely related to their external electron configuration, particularly the partially filled 3d shell (Fe: $4s^2$ $3d^6$; Co: 4s2 $3d^7$; Ni: $4s^2$ $3d^8$). The catalytic ability is thought to decrease with the gradual filling of the 3d shell. The current study and related reports reveal that a small amount of graphite always forms on a pure Cu substrate after a plasma enhanced CVD process [152]. One possible reason is that the graphite may be produced by carbon precipitation during the cooling stage. As Cu is immiscible with carbon and does not form any carbide, the amount of precipitated carbon is also limited. Due to this property, Cu has been used as a highly efficient substrate for the large-scale synthesis of graphene [153]. If a transition between $4s^1$ $3d^{10}$ and $4s^2$ $3d^9$ can occur on Cu, a weak catalytic ability will be activated and induce a slight graphitization. The XAS synchrotron analysis shown in Figure 4.12 demonstrates that alloying Al with Cu does not give rise to any obvious shifts in peak position or changes in the spectral shape of Cu, except for a slight decrease in the peak intensity with increasing Al fraction. This may be partially related to the low fraction of Al in the Cu substrate, and continued investigation is required to verify this assumption. After Al addition, covalence between Cu 3d and Al 3p orbitals is induced, Al 3p→ Cu 3d charge transfer occurs, and graphitization is suppressed. In the Al modified Cu alloy, it is believed that Al may play a key role in inhibiting the occurrence of graphitization on the Cu substrate, which acts as a physical barrier layer separating the carbonaceous gas atmosphere from the substrate. As Al has a much stronger chemical affinity for oxygen than Cu, preferential oxidation of aluminum occurs during the deposition process. At an identical temperature of 650 ℃, air oxidation of Cu–Al alloys containing 1~3 at.% Al produces mixed oxides containing both Cu and Al, as demonstrated in Figure 4.13. Comparatively, the selective

external oxidation of aluminum is significantly enhanced under the ultra-low oxygen partial pressure in the processing chamber, established by the residual oxygen and oxygen impurities originating from the gas mixture. Comparison of the previously investigated Fe–Al alloys and the current Cu–Al alloy highlights the large difference between the critical Al concentration required to form a continuous external alumina under identical deposition conditions due to the more stable nature of Cu as opposed to Fe. On the Fe–Al binary alloy, the critical Al concentration has not been precisely determined but should well exceed 10 at.%; otherwise, surface graphitization and substrate carburization on the Fe–Al alloy surface cannot be completely suppressed.

CHAPTER 5

FEE PROPERTIES OF CNTS WITH A DIAMOND INTERLAYER

In this chapter, the experimental results of FEE properties of CNTs with different densities on different substrate materials are being presented. The effects of diamond interlayer, CNT density, and substrate materials on FEE properties is then discussed and FEE mechanisms are further clarified.

5.1 Effect of a Diamond Interlayer on FEE Stability

The poor FEE stability of CNTs is mainly due to the weak adhesion between the CNTs and the substrates. In this work, a diamond thin film interlayer was adopted to enhance adhesion between the CNTs and the substrates. Figure 5.1 shows the Raman spectra of CNTs with a diamond interlayer. The sharp diamond peak centered at 1332 cm^{-1}, and D and G peaks from CNTs at 1350 and 1550-1600 cm^{-1}, respectively, indicate a mixed structure of diamond and CNTs. Generally speaking, Raman spectroscopy is relatively more sensitive to sp^2 carbon than sp^3 carbon [154]. As a result, the Raman peaks of CNTs should be stronger than those of diamond. In stark contrast, our Raman spectra give the opposite result. One possible reason for this result is that the diamond film is thick while the CNTs are thin (at the nano scale).

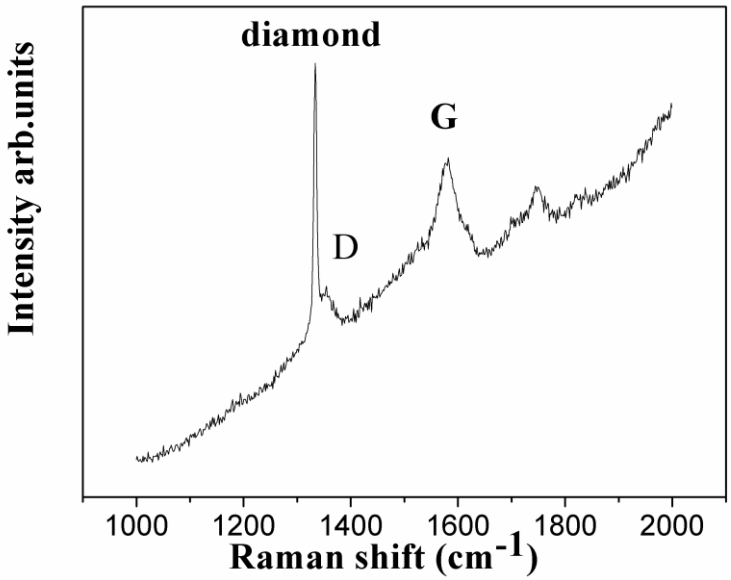

Figure 5.1. Raman spectra of CNTs with a diamond interlayer.

Figures 5.2 and 5.3(a,b) show the morphology of the CNTs with a diamond thin film interlayer without bias treatment and with bias treatment of -400 and -700 V, respectively. The CNTs are randomly distributed if no bias voltage is applied and vertically aligned if negative bias is applied. The CNTs deposited at a bias voltage of -400 V exhibit a better alignment than those deposited at a bias voltage of -700 V. The results confirm that biasing is needed to obtain aligned CNTs, and strong bias voltage is harmful to the alignment. Merkulov *et al.* propose a bias assisted CNT alignment growth theory [71]. In this theory, CNTs with tip growth and base growth would have different alignment properties due to the stress on the catalyst particles produced by bias electrostatic forces. Tip growth would enhance alignment while base growth would not enhance alignment. The CNTs in Figure 5.3 are well aligned, and so may follow a tip growth model.

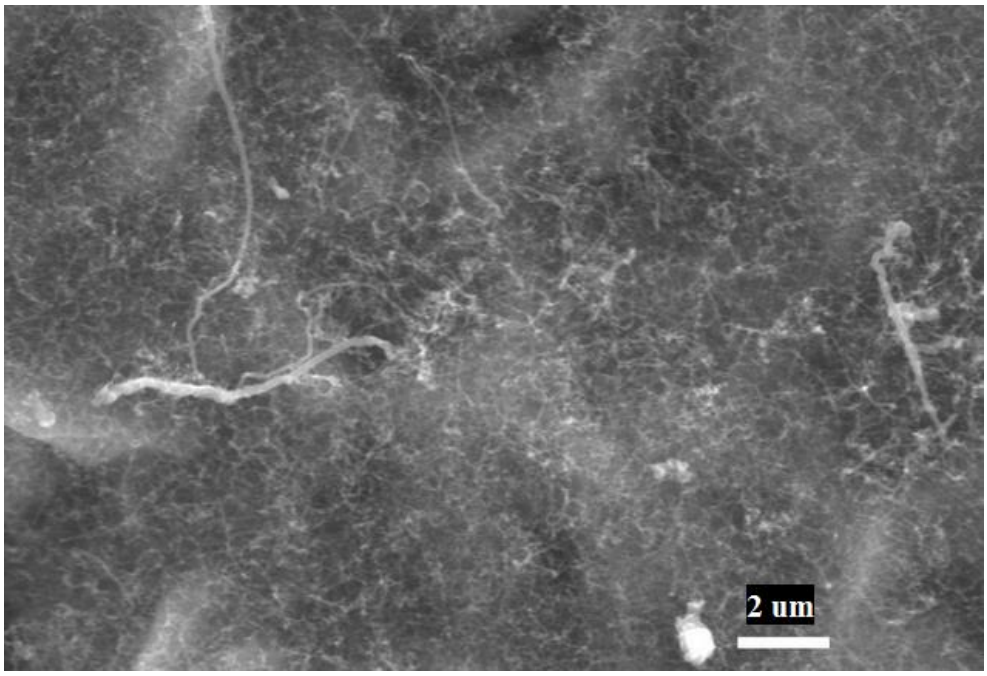

Figure 5.2. SEM image (SEI mode) of CNTs deposited without applied bias voltage.

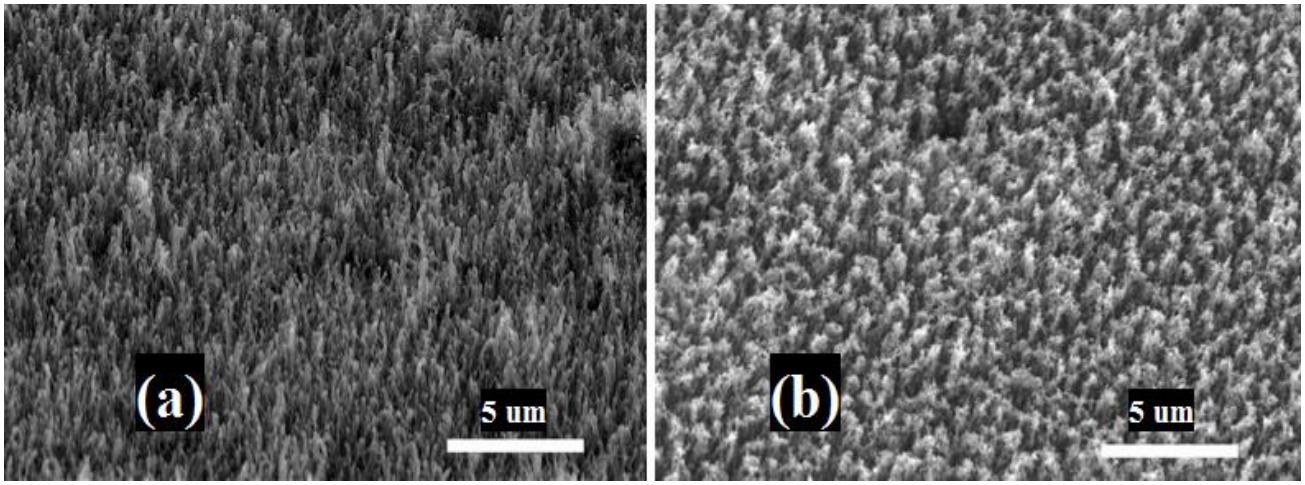

Figure 5.3. SEM images (SEI mode) of CNTs deposited on diamond with a bias voltage of (a) -400 V and (b) -700 V on the substrate.

Figure 5.4 shows SEM images (top-view and tilted at an angle of 30°) of CNTs deposited on diamond thin films. The left part of each image was taken using BEI mode and the right part of each image was taken using the SEI mode. The catalyst (iron) has a higher atomic number than carbon, it is much brighter than the CNTs; thus, the the brighter spots in the figures indicate the existence of catalyst particles. In Figure 5.4(a), the catalyst particles

are sparsely distributed, indicating a low density of CNTs. In Figure 5.4(b), the CNTs are vertically aligned and there is a catalyst particle on each tip, demonstrating that they followed the tip growth model. Figure 5.5 is a TEM image of the CNTs scratched out of the substrate. Dark catalyst particles located at the tip of CNTs also indicates that they followed the tip growth model. It has been proposed that the interaction between the catalyst particles and the substrate determines the growth model of the CNTs, i.e., “base growth” or “tip growth” [70]. The spin-coating catalyst on the diamond thin film surface has a weak interaction with the diamond thin film. CNTs could grow in the spaces between the catalysts and the diamond thin film, which results in tip growth. Under these conditions, direct contact between the CNTs and the diamond might result in C-C covalent bonding [101, 102].

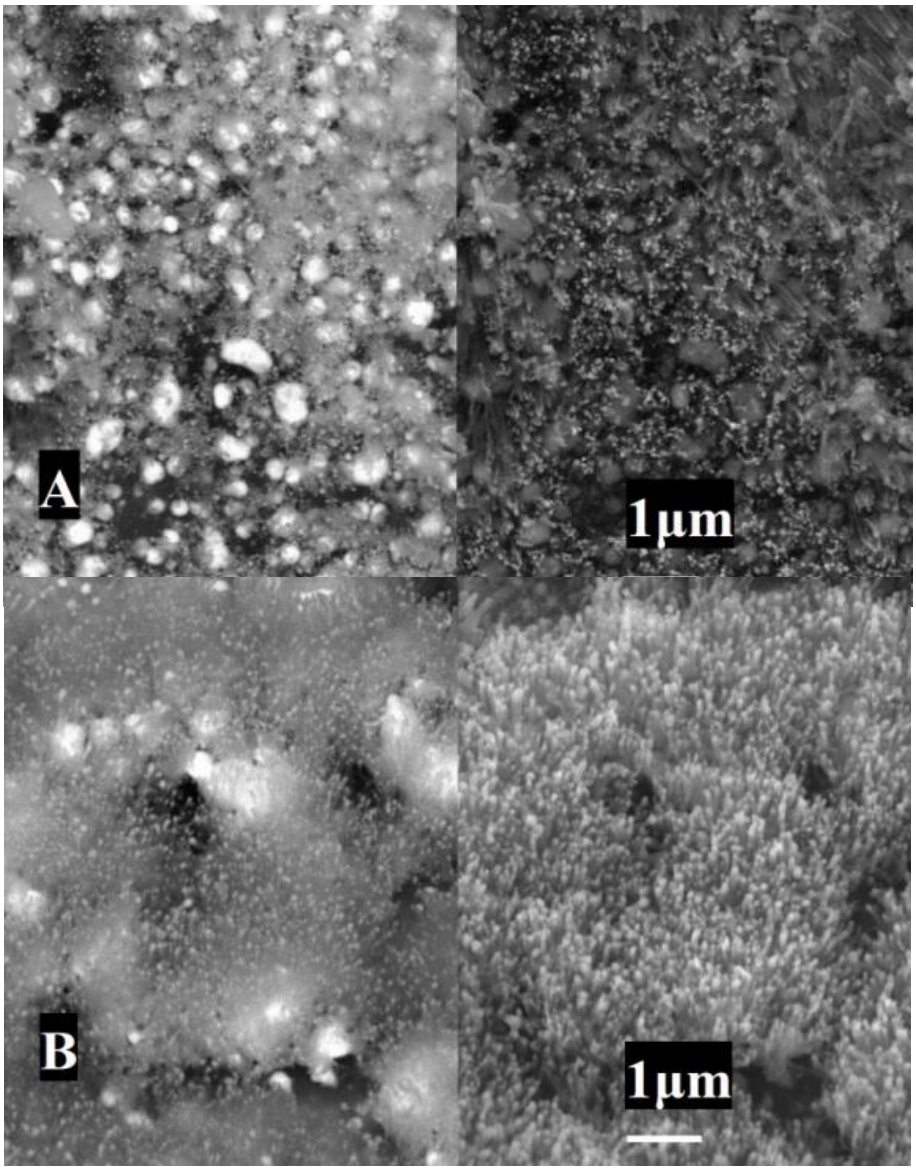

Figure 5.4. SEM images of CNTs deposited on diamond: (A) top view and (B) tilted at a 30 ° angle. The left part of each picture is in BEI mode and the right part of each picture is in SEI mode.

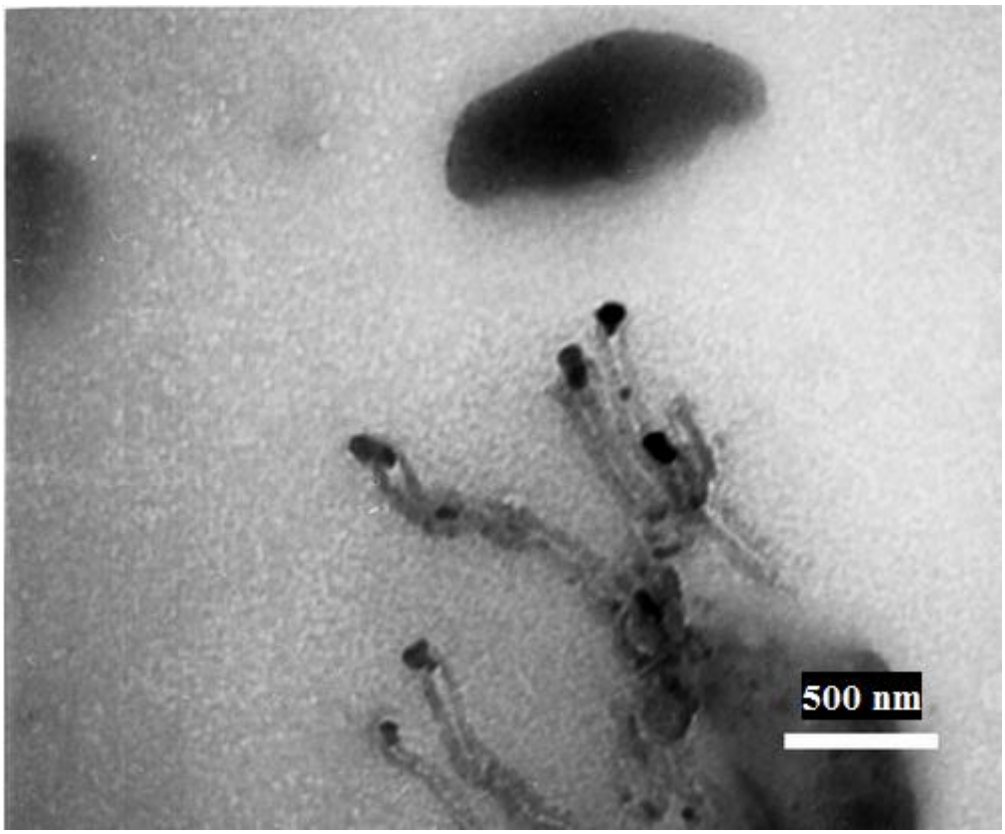

Figure 5.5. TEM image (bright field) of CNTs scratched off the substrate.

For comparison, another group of CNTs were deposited using sputtered catalysts on diamond thin films. Sputtered catalysts have a relatively strong interaction with the diamond thin film, which results in “base growth”. In this case, the catalyst particles are located at the bottom of the CNTs and are sandwiched between the CNTs and the diamond thin film. CNTs deposited under these conditions should be weakly adhered to the diamond thin film. This assumption is confirmed by tap water flushing testing (Figure 5.6). The CNTs deposited with the sputtered catalyst are flushed away by the tap water whereas the CNTs deposited with spin-coated catalysts are still adhered to the diamond layer after flushing.

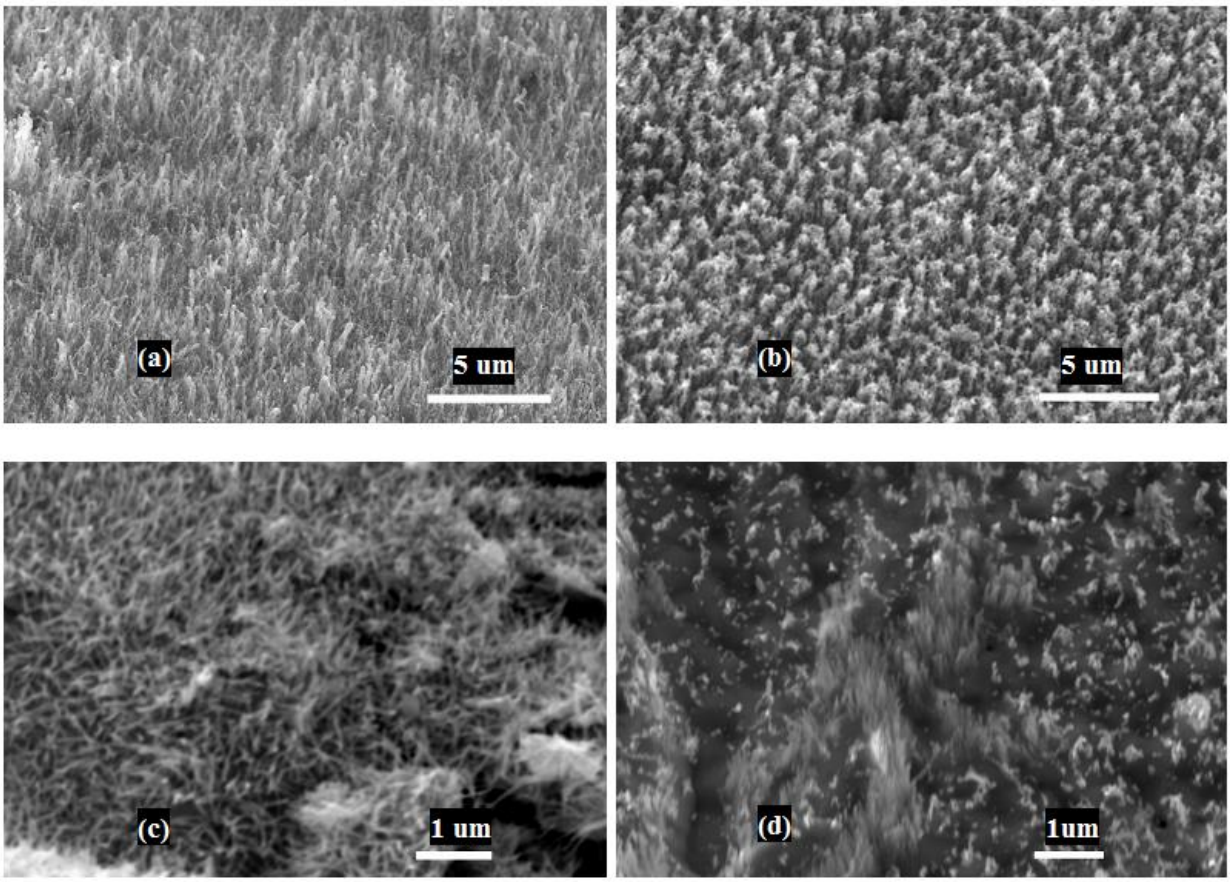

Figure 5.6. SEM images (SEI mode) of spincoated CNTs (a,c) and sputtered CNTs (b,d) before (a,b) and after (c,d) tap water flushing testing.

The TEM and SEM images clearly show that CNT deposition by the spin-coating method results in a “tip growth” mechanism in which the catalyst particles are located at the top of the CNT tips. The diamond thin film underneath is then directly bonded to the CNTs. This direct contact between the diamond thin film and the CNTs might enhance the adhesion and thermal conductivity of CNTs to the substrate, which would facilitate FEE stability of the CNTs.

Figure 5.7 displays the emission current vs. electric field strength curve of CNTs and CNTs with a diamond interlayer on Si substrates, respectively. CNTs with a diamond interlayer have a lower emission current than pure CNTs in the same electric field. The reduced emission current is possibly due to the poor electrical conductivity of the diamond interlayer, which increases the potential barriers of emission. In order to obtain more detailed

emission properties of these materials, a Fowler-Nordheim (F-N) curve of the ln (I/V^2) vs. V^{-1} derived from the current-field curve was plotted and is shown in Figure 5.8. F-N theory provides a model for electron tunneling through the surface barrier [107]. The linear curve of an F-N plot indicates the electron emission from the tunnel effect, and the slope of the curve is related to the field enhancement factor (β). In F-N theory, β can be calculated using equation 5.1 [155],

$$\beta = bd\Phi^{3/2}/m\ , \qquad (5.1)$$

where $b = -6.83\times10^{7} eV^{-3/2} Vcm^{-1}$, $d = 5\times10^{-4}$ cm, m is the slope of the F-N plot, and Φ is the work function of the CNTs in eV. From the literature, a work function of 5.0 eV is commonly used to calculate β [109]. Thus, the β of CNTs on Si is about 4.5×10^{3}, and the β of the CNTs with a diamond interlayer on Si is about 1.8×10^{3}. Both emitters have a high value of β due to FEE enhancement resulting from high aspect ratio of the CNTs [4].

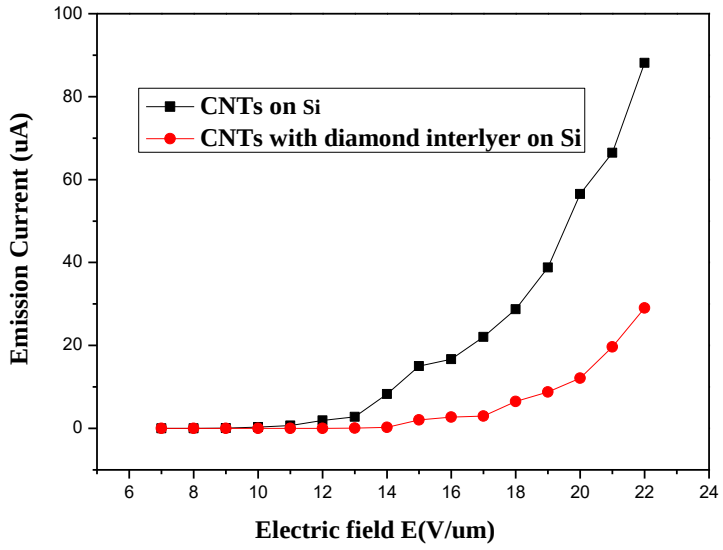

Figure 5.7. Emission current-electric field strength curves of CNTs and CNTs with a diamond interlayer on Si substrates.

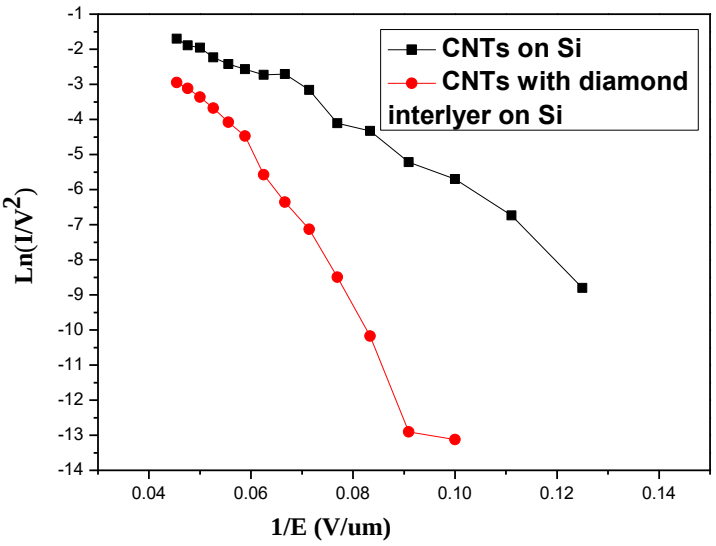

Figure 5.8. F-N plot of CNTs and CNTs with a diamond interlayer on Si substrates.

FEE stability has been studied by measuring how the emission current varies with time (initial emission current was 30 uA). Figures 5.9 and 5.10 illustrate these results for the CNTs and the CNTs with a diamond interlayer on Si substrates, respectively. CNTs with a diamond interlayer have significantly enhanced emission stability compared to pure CNTs. After 5000 minutes, the emission current of the CNTs with a diamond interlayer on Si substrates is 27 uA without obvious degradation from the starting value of 30 uA. But after only 60 minutes, the emission current of the CNTs on the Si substrate degraded from 30 to 17 uA. The decay of the emission current is probably due to CNT emitter damage caused by heat accumulation during emission. The improvement of the emission stability of the CNTs with the diamond interlayer is significant.

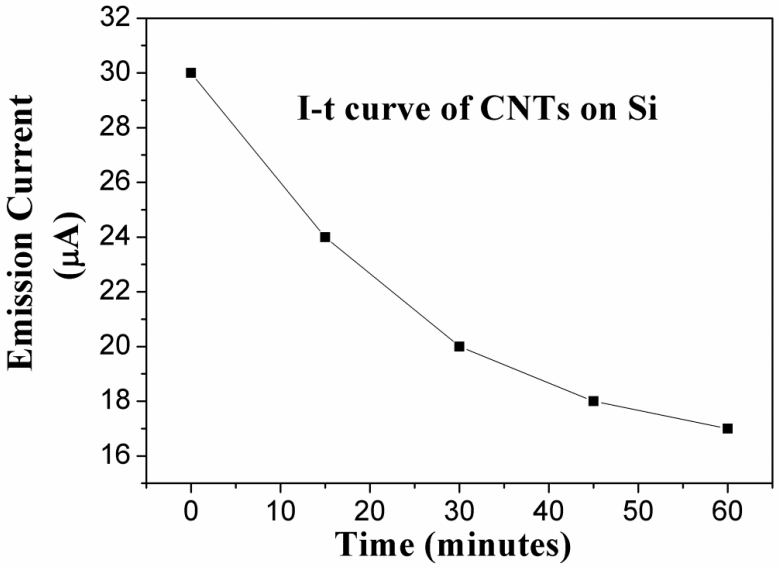

Figure 5.9. Emission current versus time for CNTs on Si.

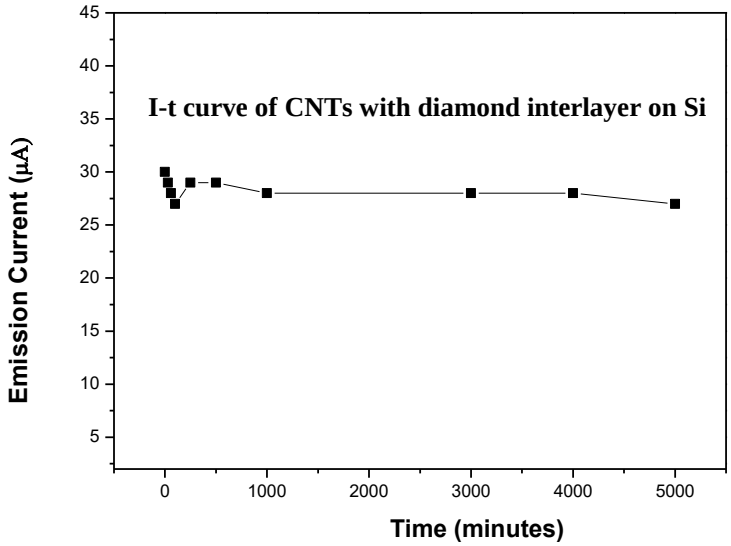

Figure 5.10. Emission current versus time for CNTs with a diamond interlayer on Si.

Table 5.1 lists the emission stability of our CNTs with a diamond interlayer and other CNT-based materials, including CNT coated tips, CNT/diamond monolithic composites, and diamond coated CNTs. It shows that our material exhibits superior emission stability compared to other CNT-based materials. As discussed in Chapter two, the failure of CNT

FEE emitters is caused by the weak adhesion between the CNTs and the substrates [12]. The weak adhesion results in heat accumulating, which burns out the CNT emitters. For the CNTs with a diamond interlayer emitters in this work, the CNTs can form strong covalent bonds with the diamond thin film and have good adhesion strength [102]. The high thermal conductivity of the diamond layer and the strong covalent bonding at the interface can significantly improve the heat transfer from the CNT emitters to the substrate and thus decrease the damage to the CNTs resulting from heat accumulation during the emission. Consequently, emission stability can be significantly improved.

Table 5.1. Current stability of various CNT-based materials.

Materials	**Current stability (min)**	**Reference**
CNTs on Co tip	2100	[156]
CNT-diamond monolithic composite	2600	[109]
CNTs on W tip	2400	[157]
Diamond coated CNT teepee	2000	[158]
Nano-diamond coated single wall CNT	900	[120]
CNTs with a diamond interlayer	>5000	Present research

To further understand the mechanism by which CNTs with a diamond thin film interlayer enhance FEE stability, diamond thin films with different sp^2 content were prepared. Figure 5.11 is a SEM image of a 1 vol.% CH_4 micro-diamond film synthesized by HFCVD. From Figure 5.11, it is evident that the film has a well-faceted microcrystalline structure with a grain size ranging from submicron to a few micrometers.

The Raman spectrum of this film in Figure 5.12 shows a sharp diamond peak centered at 1332 cm^{-1} with a low broad non-diamond carbon peak, indicating high quality diamond with low non-diamond carbon impurities, e.g., sp^2 carbon. In general, the thermal conductivity of diamond film is higher with increased grain size and reduced impurities because phonons are the main carriers for conducting heating in diamond [159]. The phonons will be scattered at grain boundaries and impurities, resulting in reduced heat transfer efficiency. Therefore, films with larger grain sizes and higher impurity have enhanced thermal conductivity because of the reduced phonon scattering [159].

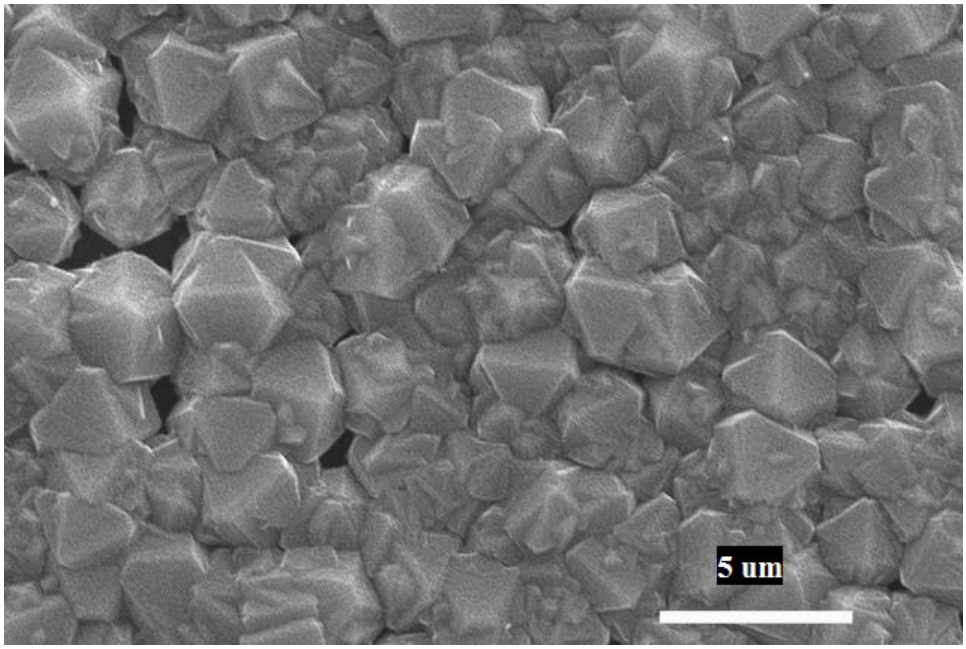

Figure 5.11. SEM image of surface morphology of 1 vol.% micron-diamond film.

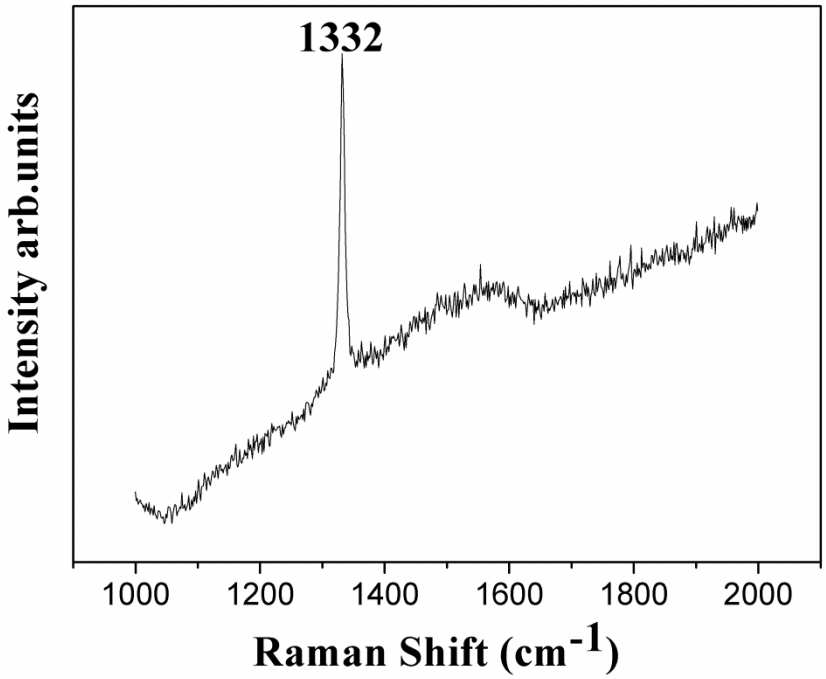

Figure 5.12. Raman spectra of 1 vol.% micron-diamond film.

Figure 5.13 is a SEM image of 5 vol.% CH_4 nano-diamond film synthesized by HFCVD and Figure 5.14 is the Raman spectra of this film. Figure 5.13 shows that the diamond film has a nano-crystalline structure with a grain size less than 100 nm. The Raman spectra in Figure 5.14 have two broad peaks centered at 1332 and 1580 cm^{-1}, which indicates that this diamond film contains a relatively high level of non-diamond carbon impurity. The thermal conductivity of this 5 vol.% CH_4 nano-diamond film should be lower than that for the 1 vol.% CH_4 micron-diamond.

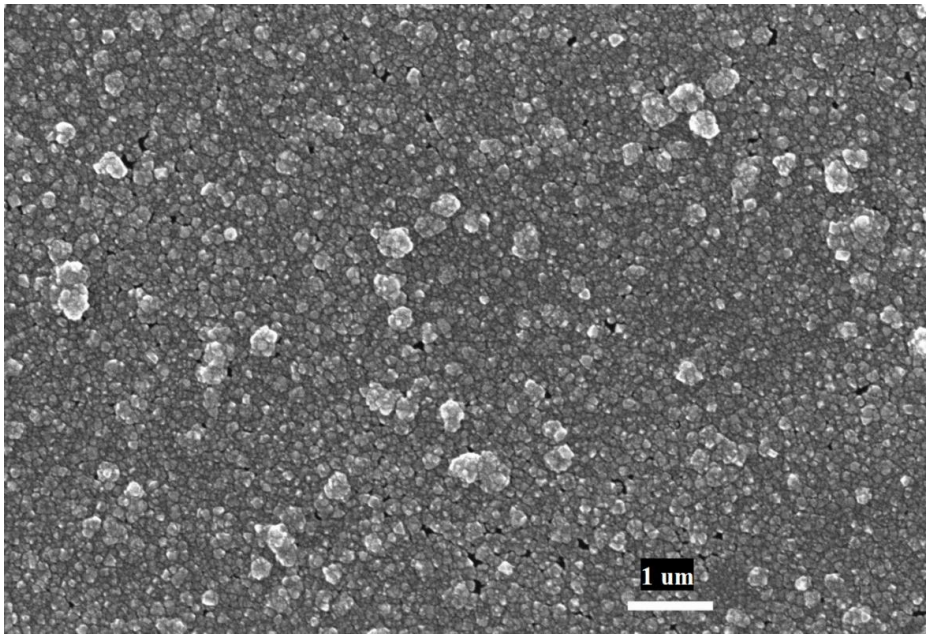

Figure 5.13. SEM image of surface morphology of 5 vol.% nano-diamond film.

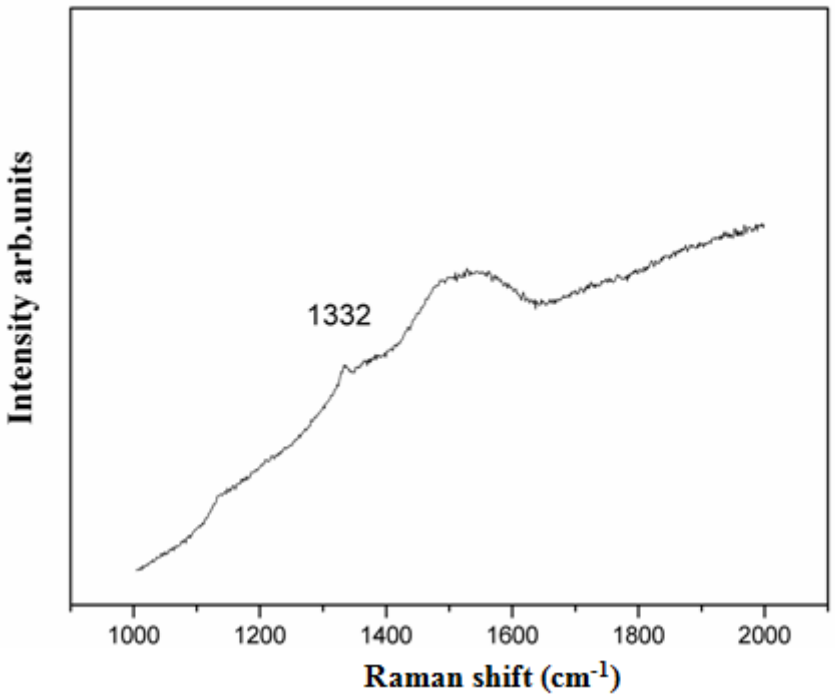

Figure 5.14. Raman spectra of 5 vol.% CH_4 nano-diamond film.

Figures 5.15 and 5.16 are the FEE stability testing I-t curves for CNTs with the 1 vol.% CH_4 micron-diamond film and the 5 vol.% CH_4 nano-diamond film, respectively. It appears

that both samples have good emission stability. After 5000 minutes, the current of the 1 vol.% CH_4 micron-diamond film sample decays from 30 to 27 μA and the current of the 5 vol.% CH_4 nano-diamond film sample decays from 30 to 25 μA. The CNTs with the 1 vol.% micron-diamond film only show slightly better stability than those with the 5 vol.% nano-diamond film. Therefore, increasing the grain size and decreasing the purity of the diamond thin film interlayer can improve the FEE stability of the CNTs but it is not a major effect.

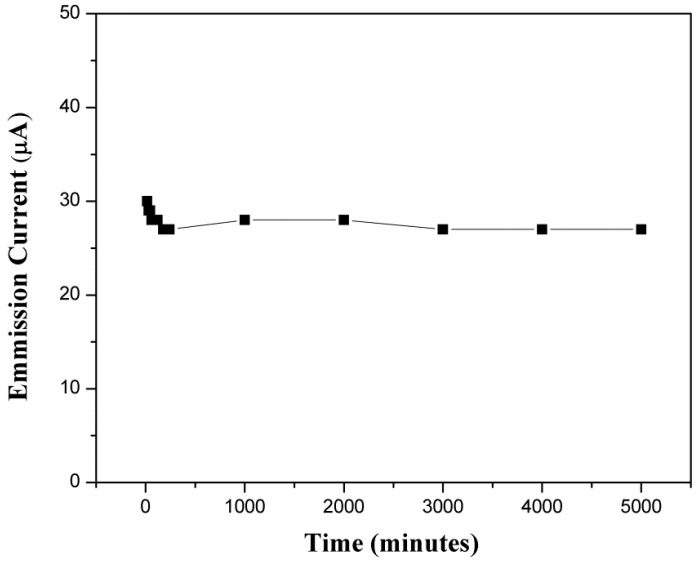

Figure 5.15. FEE I-t curve of CNTs with 1 vol.% micron-diamond film.

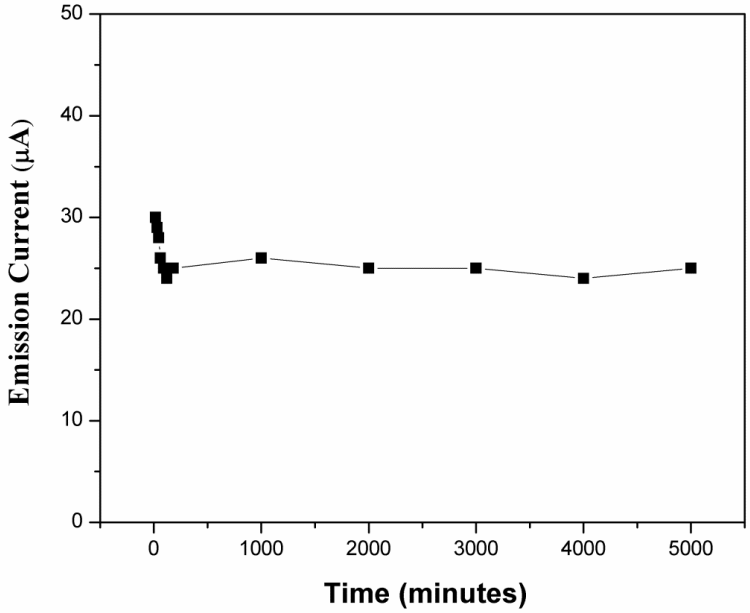

Figure 5.16. FEE I-t curve of CNTs with 5 vol.% nano-diamond film.

5.2 Effect of Substrate on FEE stability

The substrate effect on the FEE stability of CNTs with a diamond thin film interlayer was also considered. Substrates with high thermal conductivity probably also enhance the FEE stability of emitters in the present work. Therefore, the CNTs with the diamond thin film interlayer were deposited on Cu substrates. To have a clear view of the diamond interlayer and the Cu substrate, the sample was scratched using tweezers. Figure 5.17 is the SEM image of the CNTs after scratching. A vertically aligned CNT layer, a diamond layer underneath, and the Cu substrates can all be clearly seen.

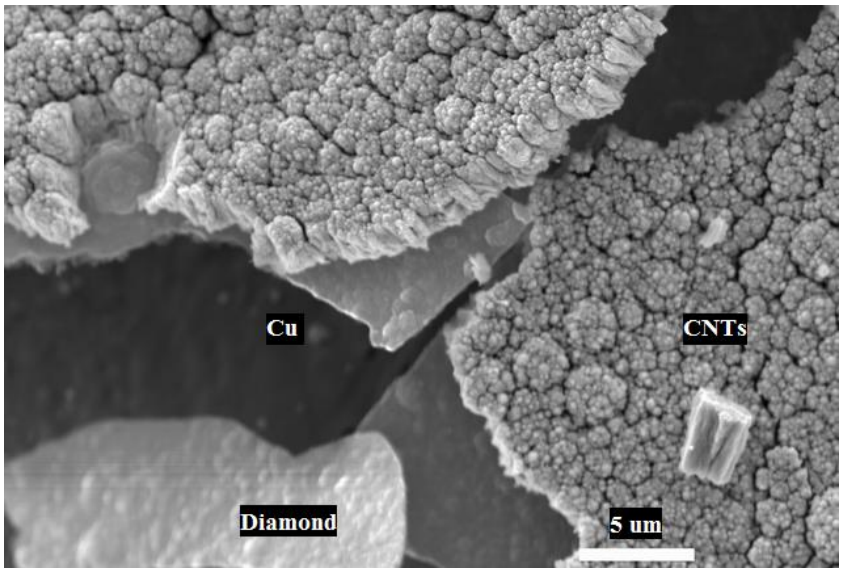

Figure 5.17. SEM image (SEI mode) of CNTs with a diamond interlayer on Cu substrate after scratching.

Figures 5.18 to 5.20 present the FEE stability testing results for CNTs deposited directly on Cu substrates, CNTs with a diamond interlayer on Cu substrates, and CNTs with a diamond interlayer on Si substrates, respectively. It can be seen that the emission currents of the CNTs with a diamond interlayer on Cu substrates and Si substrates have good emission stability during the 5000 minutes testing. On the contrary, the emission current of the CNTs directly deposited on Cu substrates decreases from 30 to 9 μA in 60 minutes.

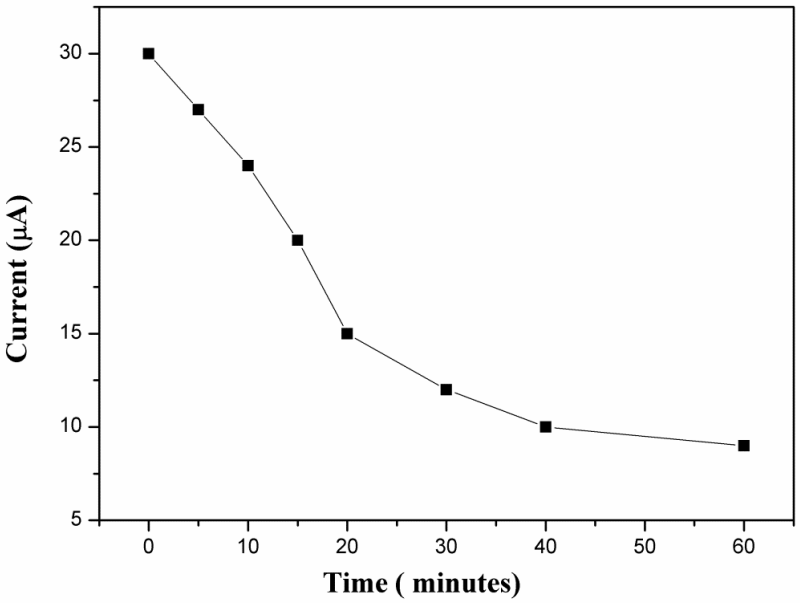

Figure 5.18. FEE I-t curve of CNTs directly on Cu substrate.

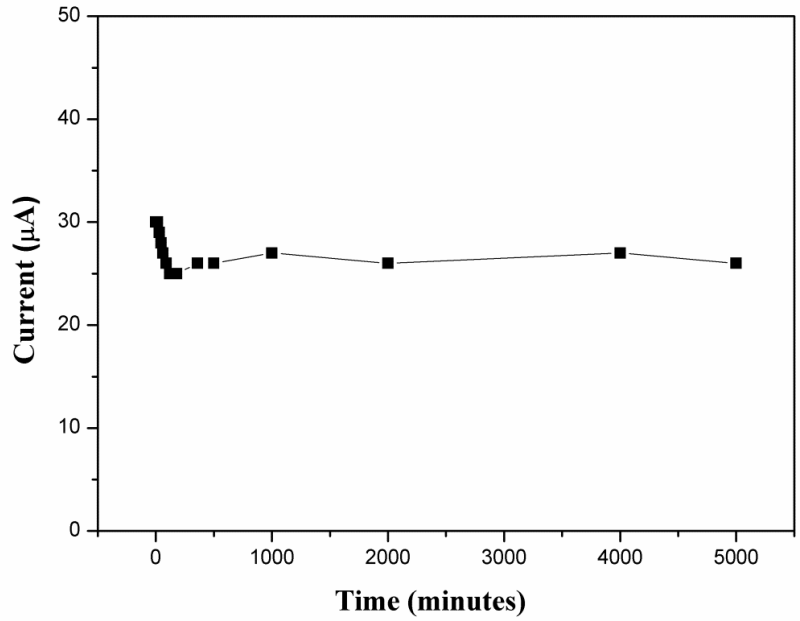

Figure 5.19. FEE I-t curve of the CNTs with a diamond interlayer structure on Cu substrate.

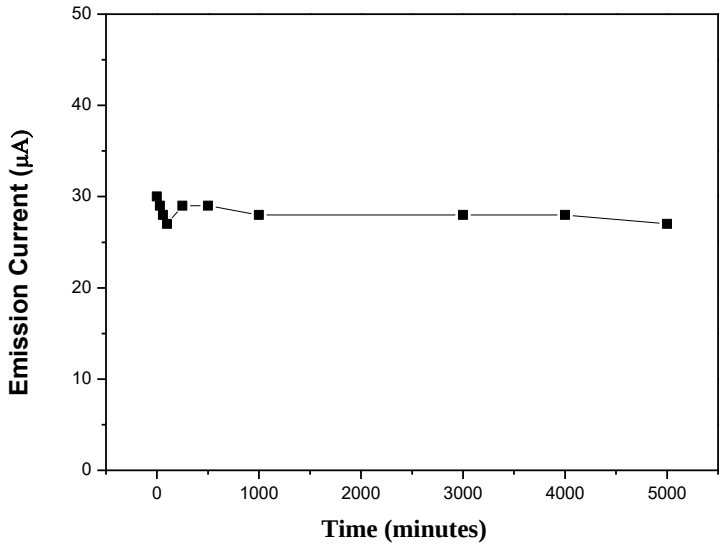

Figure 5.20. FEE I-t curve of the CNTs with a diamond interlayer on Si substrate.

The FEE degradation is probably caused by damage to the CNTs due to heat accumulation at the interface resulting from the poor interfacial contact [12]. The diamond layer has good contact with both the CNTs and the substrate, which enhances the heat dissipation generated at the interface, and thus improves the emission stability of the CNTs. The good FEE stability of the CNTs with the diamond interlayer demonstrates that the diamond film effectively absorbs the heat accumulated during emission and transfers it to the substrate. The Cu substrate has a much higher thermal conductivity than the Si substrate, so Cu might be a better heat conducting channel than Si to disperse heat generated. But results from Figures 5.19 and 5.20 indicate that emitters on Cu substrates do not have significantly better stability performance than those on Si substrates. Therefore, we can conclude that the substrate material does not have a major effect on the FEE stability of CNTs with a diamond interlayer.

5.3 Effect of CNT Density on FEE Turn-on Field

It is believed that CNT density can influence the FEE turn-on field [4]. Figure 5.21 shows SEM images of CNTs deposited with catalysts spin-coated for different lengths of

time ranging from 30 to 120 seconds. The CNT density decreased with increasing spin-coating time. The CNTs grown with catalyst spin-coated for 90 seconds are uniform with a relatively appropriate density and are probably the best for FEE applications. CNTs spin-coated for 60 seconds have a higher density, which might cause "screen effect" and increases the turn-on field. The density of the CNTs spin-coated for 120 seconds is not sufficient to supply an emission current. Figure 5.22 provides the FEE I-E plots of CNTs prepared by spin-coating for 60, 90, and 120 seconds. The 90 second spin-coating sample has an obviously lower FEE turn-on field and higher emission current than the other two samples. The results show that 90 second spin-coating time provided the best CNT density for the FEE in this work.

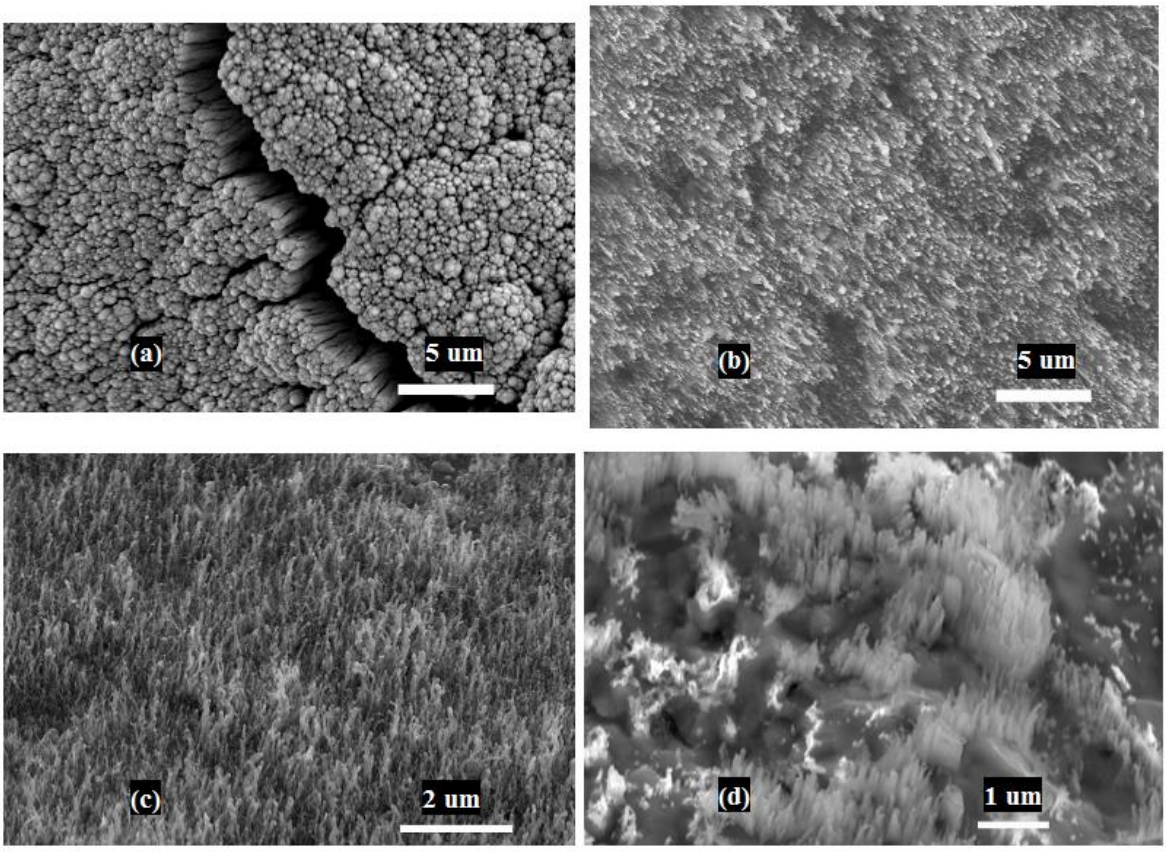

Figure 5.21. SEM images (SEI mode) of CNTs deposited on diamond coated Cu substrates with catalyst spin-coated for (a) 30 seconds, (b) 60 seconds, (c) 90 seconds, and (d) 120 seconds.

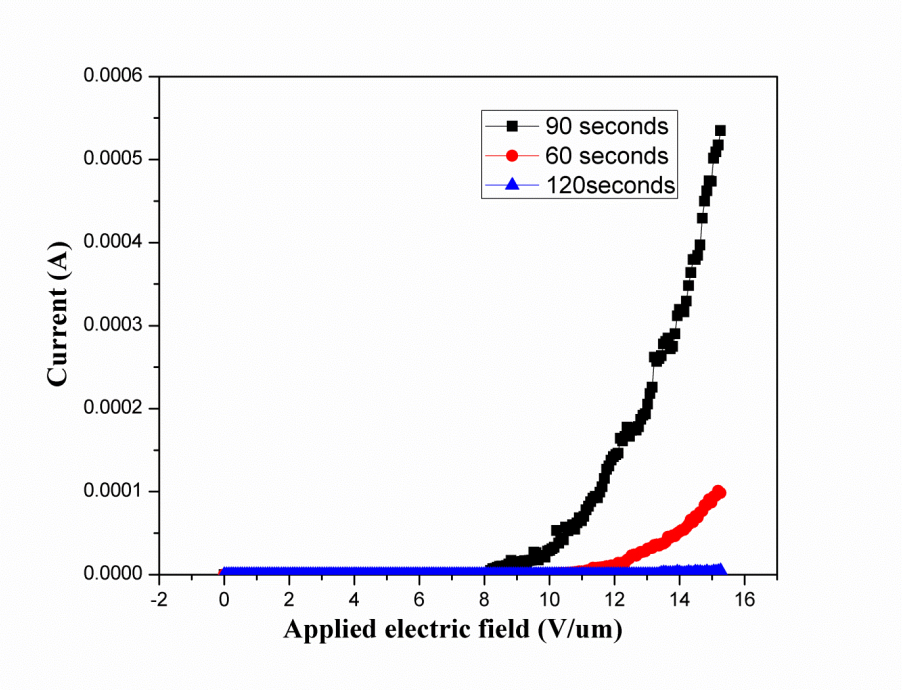

Figure 5.22. FEE I-E plot of CNTs deposited with different catalyst spin-coating times.

5.4 Effect of Diamond Interlayer on FEE Turn-on Field

To understand the effect of the diamond thin film interlayer on our emitters' FEE turn-on field, diamond thin films with different sp^2 content were prepared. Figure 5.23 depicts the Raman spectra of the diamond thin films and CNTs with the diamond interlayer. The spectrum of the CNTs with the diamond interlayer shows a D peak at 1350 cm^{-1} and a G peak at 1580 cm^{-1}. No diamond peak is found, indicating that the CNTs covered the diamond layer. It can also be seen that the diamond peak from the diamond thin film shifted from 1332 to 1338 cm^{-1}, which indicates high compressive stress in the diamond layer. This stress is caused by the large thermal expansion coefficient difference between the diamond and the Cu substrate. There is also a broad peak around 1580 cm^{-1} in the spectra of the diamond thin film, revealing graphitic carbon formed in the thin film. The intensity of this peak is higher in the 5 vol.% CH_4 diamond sample than in the 1 vol.% CH_4 diamond sample, corresponding to a higher graphitic carbon content. This graphitic carbon is induced by the coalescence of nano-sized diamond clusters that could increase the conductivity of the diamond [166]. As a result, the 5 vol.% CH_4 diamond thin film could have lower electrical resistance. Therefore, a lower FEE turn-on field is expected for the CNTs with this diamond layer.

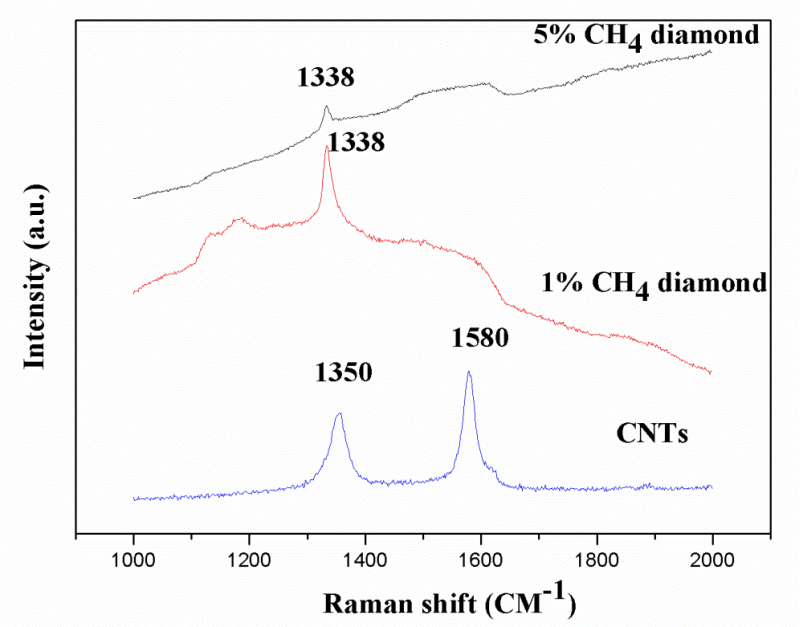

Figure 5.23. Raman spectra of CNTs and of diamond films grown with 1 vol.% CH_4 and 5 vol.% CH_4.

The FEE I-E plots of the CNTs with 5 vol.% CH_4 (DC5%) diamond and 1 vol.% CH_4 diamond (DC1%) on a Cu substrate as well as CNTs with 1 vol.% CH_4 diamond on an Si substrate (DS1%) are presented in Figure 5.24. Figure 5.25 provides the corresponding FEE F-N plots. If we define the turn-on field as the electric field at which the emission current reaches 0.01 μA, the DC 5% sample has a turn-on field of 5.1 V/μm while that for the DC 1% sample is 10.2 V/μm and for the DS 1% sample is 13.8 V/μm. All of the F-N plots of the three samples are linear with an explicit knee. These results indicate that both the substrate material and the graphitic carbon content in the diamond layer affect the turn-on field of the CNTs. The DC 5 % sample with the higher graphitic carbon content in the diamond layer had the lowest turn-on field. This is probably due to these factors reduced the emission barrier of the material. It is well known that diamond has a high FEE turn-on field due to the difficulty in conducting electrons from the back contact into the conducting band of the diamond [103]. A previous study noted that the sp^2 carbon (graphitic phase) in the diamond grain boundary region could be a conducting channel [17]. The sp^2 carbon could act as the electron transportation path, transporting electrons and improving the conductivity of the diamond. Lu

et al. used a high CH_4 concentration to increase the sp^2 phase content in diamond for FEE applications [114]. The FEE turn-on field was reduced from 16 to 6 V/μm. In the present work, the diamond thin film interlayer appears to be the major barrier blocking the transport of electrons into the CNTs. But if the diamond layer has high sp^2 content, it would have better electron transport ability and inject more electrons into the CNTs. Accordingly, the CNT FEE turn-on field would be reduced. A similar mechanism was presented by Sharma *et al.* who used a Ti interlayer between CNTs and a silicon substrate [161]. The introduction of the Ti interlayer acted as a conducting channel between the substrate and the CNTs and reduced the FEE turn-on field. Other investigations have also shown reduced FEE turn-on fields due to enhanced electrical conductivity between CNTs and the substrate [119]. Furthermore, Cu substrates have much higher electrical conductivity than Si substrates. Therefore, in Figure 5.25, the DC 5 % sample deposited on a Cu substrate with a higher sp^2 content in the diamond layer would have the lowest interfacial resistivity and thus the lowest FEE turn-on field.

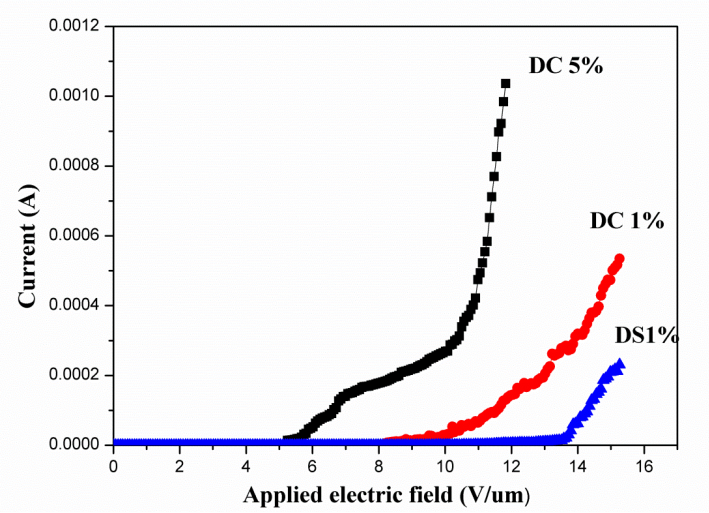

Figure 5.24. FEE I-E plot of CNTs on Cu substrate with 5 vol.% CH_4 diamond (DC 5%) and 1 vol.% CH_4 (DC 1%) diamond, and CNTs on Si substrate with 1 vol.% CH_4 (DS1%) diamond.

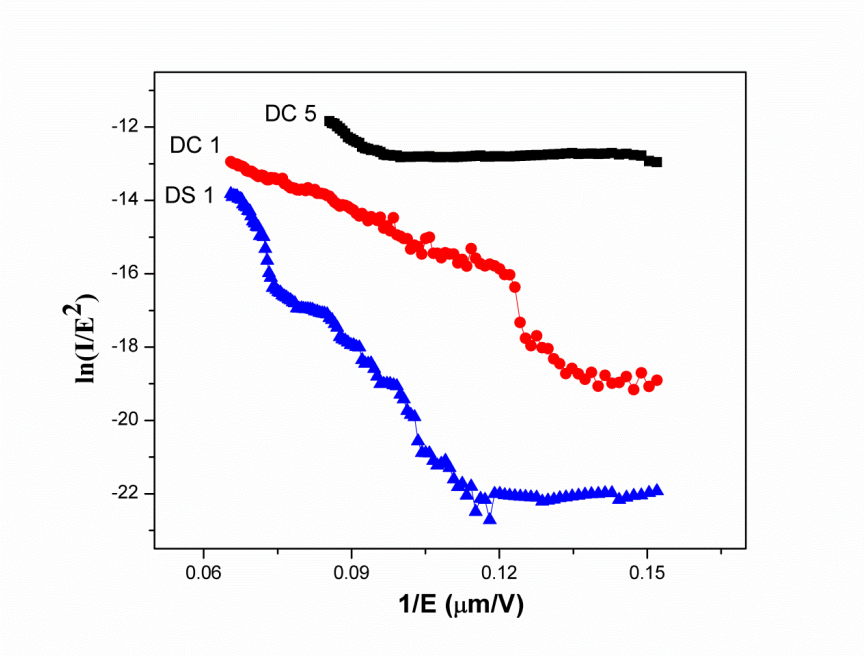

Figure 5.25. FEE F-N plot of CNTs on Cu substrate with 5 vol.% CH_4 (DC 5%) diamond and 1 vol.% CH_4 (DC 1%) diamond, and CNTs on Si substrate with 1 vol.% CH_4 (DS1%) diamond.

Similar to the two barrier model proposed by Zhang *et al.* [13], the process where electrons are transported from the substrate to the CNTs and then emitted into vacuum involves two barriers. First, the electrons cross the barrier between the substrate and the CNTs. Second, they are emitted from the CNTs to vacuum. The band diagram in Figure 5.26 shows the two barriers that electrons need to overcome (Barrier I and Barrier II, respectively).

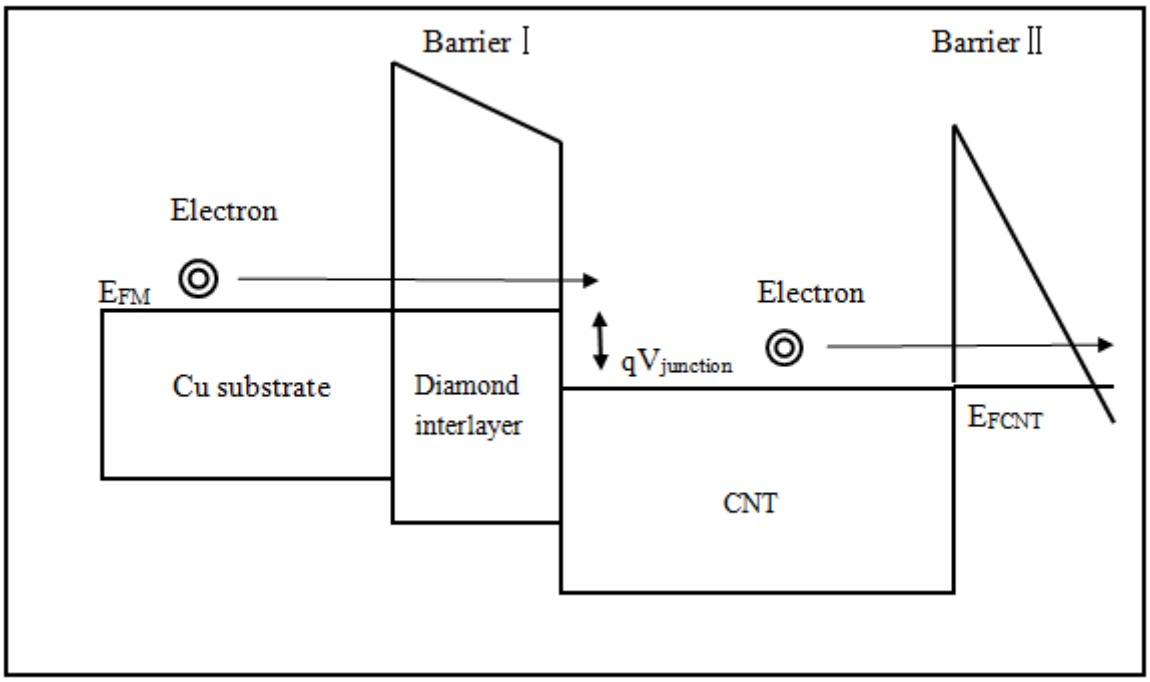

Figure 5.26. Band diagram of CNTs with a diamond interlayer. E_{FM} and E_{FCNT} are the Fermi levels of the substrate and CNT, respectively. $J_{unction}$ is the voltage drop at the diamond interlayer.

Diamond has a low electrical conductivity resulting in high resistance with the substrate and the CNTs. Therefore, it is difficult for electrons to pass Barrier I. But the sp^2 content in the diamond can be a bridge for electron transport. So diamond with a higher sp^2 content could have a reduced barrier effect. The FEE I-E plot in Figure 5.24 shows that the DC 5% sample with the high sp^2 content has a low FEE turn-on field, which may be due to its reduced barriers. In Figure 5.25, a knee was noted on each of the FEE F-N plots. Similar knee structures on F-N plots have also been observed on other CNT-insulator-metal substrates emitters [162]. It is believed that the knee structure is from Barrier I at the interlayer of the emitters. Assuming Φ_0 is Barrier I, V_0 is the external electric field applied, and q is the electric charge, then when $0 < qV_0 < \Phi_0$ most electrons cannot tunnel through Barrier I. The tunneling probability of electrons is therefore quite low and will slightly increase with increasing V_0 [162]. When $qV_0 > \Phi_0$, due to the tilt of the band in the emitter, the effective height of Barrier I will be reduced as V_0 increases, which significantly increases the electron

tunneling probability and results in a knee on the F-N plots. The much lower turn-on field of CNTs with 5% diamond interlayer suggests that the diamond interlayer is the major barrier of the emitters and the existence of the knee structure on the F-N plots indicates the diamond layer acting Barrier I for such structured emitters.

CHAPTER 6

FBHT PROPERTIES OF CNTS WITH A DIAMOND INTERLAYER

In this chapter, the experimental results of FBHT properties of bare Cu, diamond coated Cu, and CNTs with a diamond interlayer are being presented and discussed.

6.1 FBHT Efficiency at Different Mass Fluxes

The FBHT efficiency of CNTs with a diamond interlayer on Cu substrates was measured and compared with diamond on Cu substrates and sandblasted Cu substrates at different mass fluxes. The surface morphology of the sandblasted Cu, diamond thin film coatings, and CNTs with diamond interlayer coatings are shown in Figure 6.1(a-c), respectively. As can be seen from Figure 6.1, the pre-treated Cu surface before deposition is rough, the diamond deposited is continuous and smooth without any cracks, and the CNTs are vertically aligned with catalyst particles on top of the tubes. The continuous diamond thin films with no cracks indicate the relatively high adhesion to the Cu substrate.

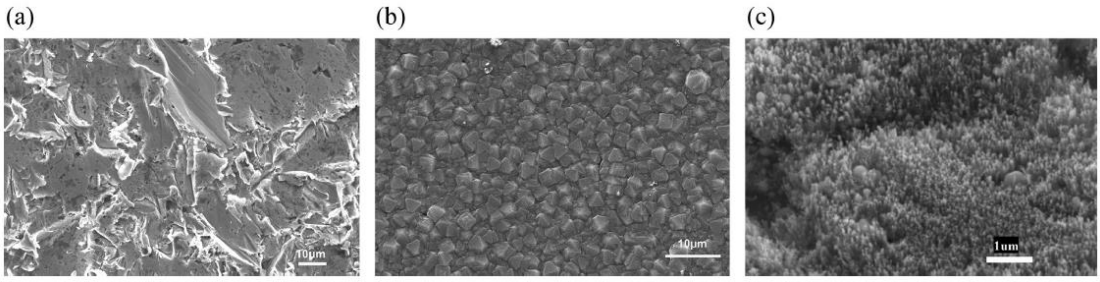

Figure 6.1. SEM images (SEI mode) of (a) sandblasted Cu, (b) diamond coated Cu, and (c) diamond and CNT with diamond interlayer coated Cu.

The bonding and phase states of the coatings were analyzed by Raman spectroscopy and XRD. The Raman spectra of the diamond interlayer and the CNTs on sandblasted Cu substrates are shown in Figure 6.2(a,b), respectively. In Figure 6.2(a), a sharp peak centered at 1330 cm^{-1} is observed, indicating diamond in the coatings. In Figure 6.2(b), peaks centered at 1348 and 1598 cm^{-1} are observed and represent the D and G peaks of MWCNTs, respectively.

The X-ray diffraction patterns of the sandblasted Cu and diamond coated Cu are shown in Figure 6.3. Both diamond and Cu peaks are clearly seen in the pattern of the diamond coated Cu samples, confirming diamond deposition on Cu.

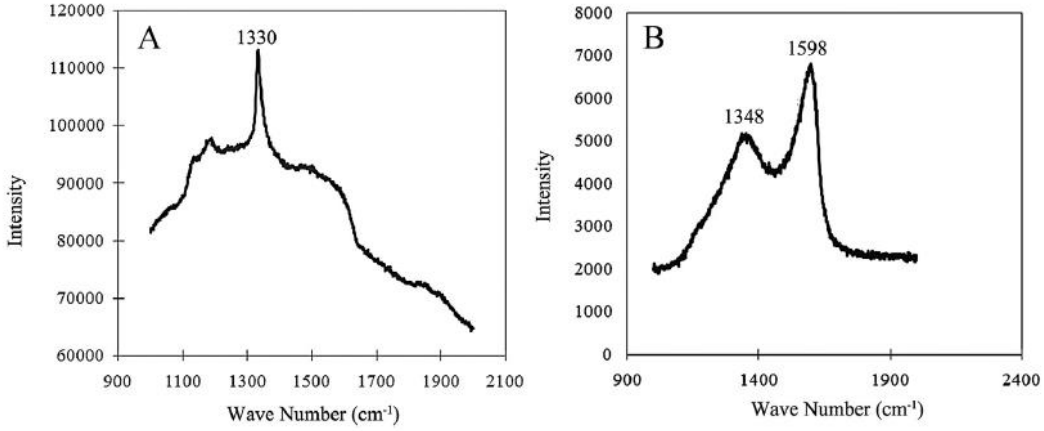

Figure 6.2. Raman spectra of (A) diamond coated Cu and (B) CNTs with diamond interlayer coated Cu.

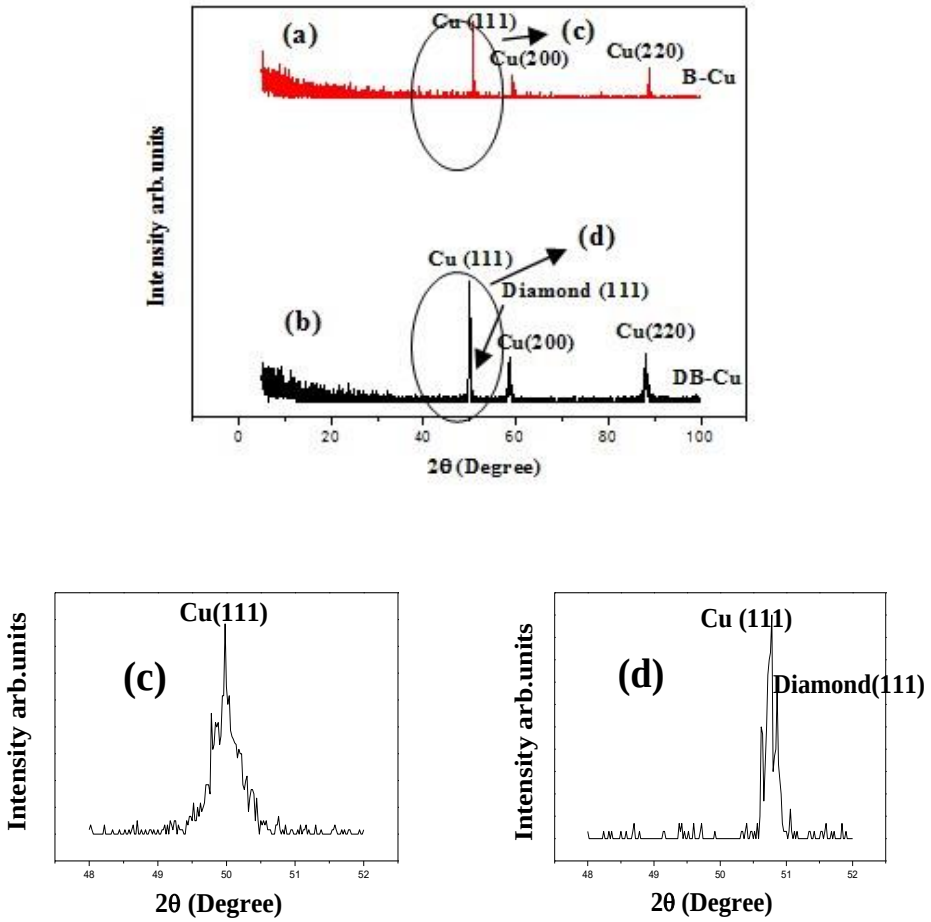

Figure 6.3. XRD pattern of (a) sandblasted Cu substrate and (b) diamond coated sandblasted Cu substrate. As indicated, (c) and (d) are enlarged areas of (a) and (b), respectively.

Flow boiling experiments were conducted for three different mass fluxes (283, 348, and 427 kg/m^{2}s) using demineralized water as the working fluid. The water inlet temperature at the entry of the testing section was maintained at 90 ℃. The flow boiling heat flux data for CNTs with diamond interlayer coated Cu and diamond coated Cu were compared with sandblasted Cu. During the experiment we found that, for all heated surfaces, nucleation commenced in the downstream region of the mini-channel in the form of bubbles and the CHF is triggered by severe vapor backflow. Due to their hydrophobicity surface property, the nucleation density of the CNT coated surface and diamond coated surface are higher compared to the sandblasted Cu surface [163]. Flow patterns obtained for the sandblasted Cu and CNT coated surfaces are different with respect to the increase in heat flux. The transition from bubbly to annular flow over the sandblasted Cu is faster compared to the CNT coated

surface but slower compared to the diamond coated surface. In the case of the diamond thin film coated surface, initial bubble formation is rapid due to its hydrophobicity. With an increase in heat flux, bubble growth is slightly higher than for sandblasted Cu, which leads to a small decrease in the CHF compared with sandblasted Cu. In the case of the CNT coated surface, initial bubble density is higher due to its hydrophobicity. But, thereafter, growth of the formed bubbles slows down due to the vertically aligned CNT fins, which leads to a slow transition from the bubbly to annular flow which increases the CHF. Vertically aligned CNTs can act as the fins, which are perpendicular to the surface. Among the CNTs is some space that can be filled in with water and vapor. So, each vertically aligned CNT should be surrounded by water or water vapor. Due to the high thermal conductivity of CNTs and the low intermediate thermal resistance between the Cu and the CNTs, the CNTs can carry heat from the surface and transfer it to the surrounding fluid, which in turn increases the area for heat transfer [147]. However, a decrease in CHF for the higher flow rates was observed due to bending of the CNTs towards the surface. The decrease in CHF at higher flow rates is also attributable to high wall shear stress. High wall shear stress narrows the boundary layer, which leads to a decrease in nucleation density and growth [128].

The amount of heat flux supplied to the water using the Cu heating block was calculated using equation 3.4. Figure 6.4(a-c) shows subcooled flow boiling curves for three different surfaces (sandblasted Cu surface, diamond thin film coated Cu surface, and CNTs with diamond thin film interlayer coated surface) under mass fluxes of 283, 348, and 427 kg/m^2s, respectively. The data were obtained from the average of different temperature measurements, at three thermocouple locations and an inlet temperature of Tin = 90 ℃. Shapes of the boiling curves for the above surfaces are almost the same, but a leftward temperature shift occurs in the case of the CNT coated surface for the different heat fluxes. The wall superheat is the temperature difference between the surface of the heating wall and the inlet water. Low wall superheat at the same heat flux indicates high heat transfer efficiency [164]. We can infer from the boiling curves that the wall superheat for CNTs with a diamond interlayer coated surface is less than the other two samples under all measured conditions. This anomalous

behavior is due to hydrophobicity, fin action, increasing surface area, and high relative roughness [132, 165]. For the diamond coated samples, there is a reduction in the wall superheat at the low heat flux region, and this effect deteriorates as the heat flux increases. In addition, the wall superheat of the diamond surface is higher than that of the Cu substrate close to the critical heat flux region. In the case of diamond, its hydrophobicity will allow initial bubble nucleation to start immediately with the bubbles growing rapidly. Later, bubbles hinder heat flow from the surface and lead to an increase in the wall temperature.

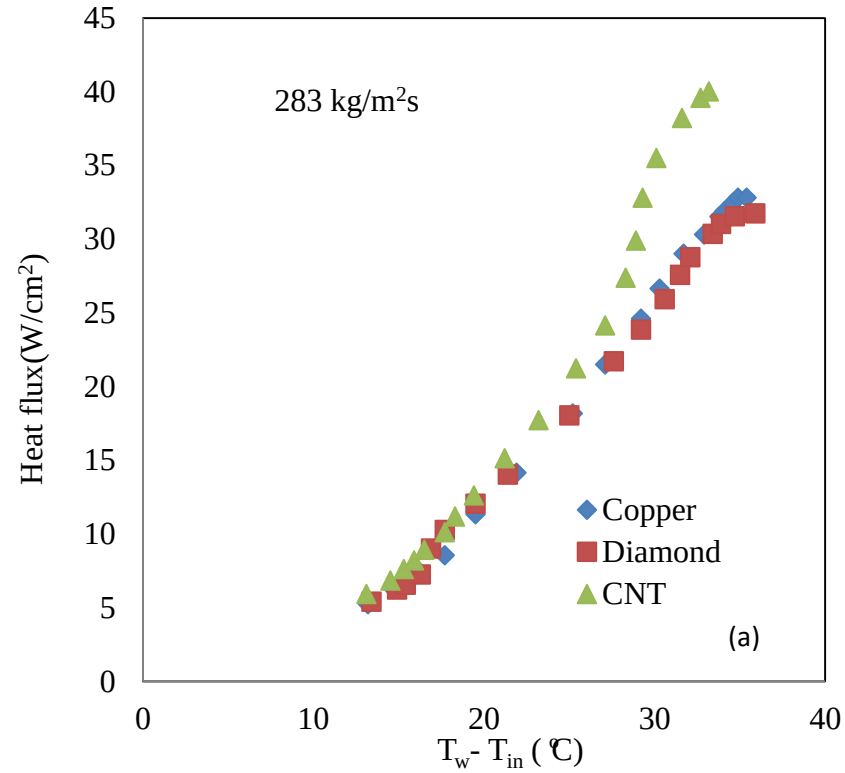
283 kg/m²s
Heat flux(W/cm²)
Tw- Tin (℃)
Copper
Diamond
CNT
(a)
0
5
10
15
20
25
30
35
40
45
0
10
20
30
40

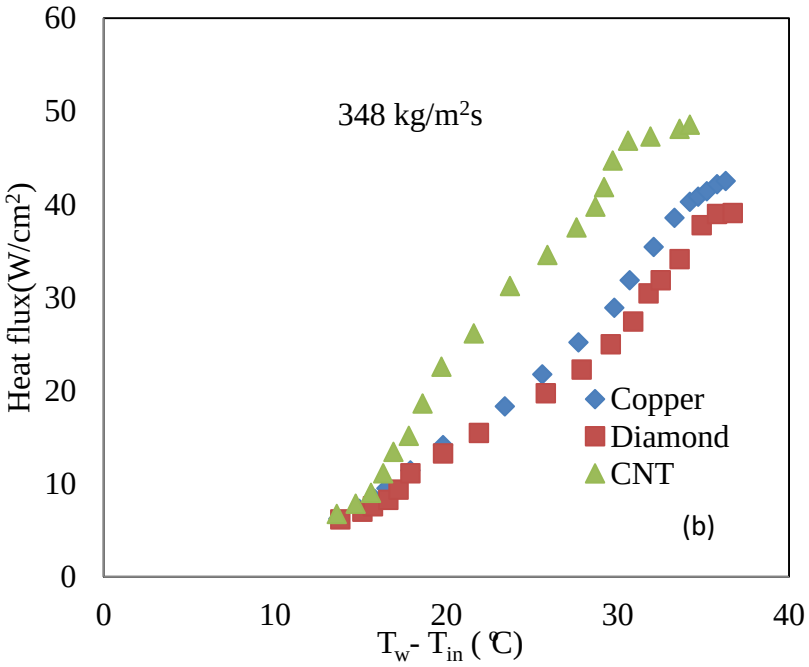
348 kg/m²s
Heat flux(W/cm²)
Tw- Tin (℃)
Copper
Diamond
CNT
(b)
0
10
20
30
40
50
60
0
10
20
30
40

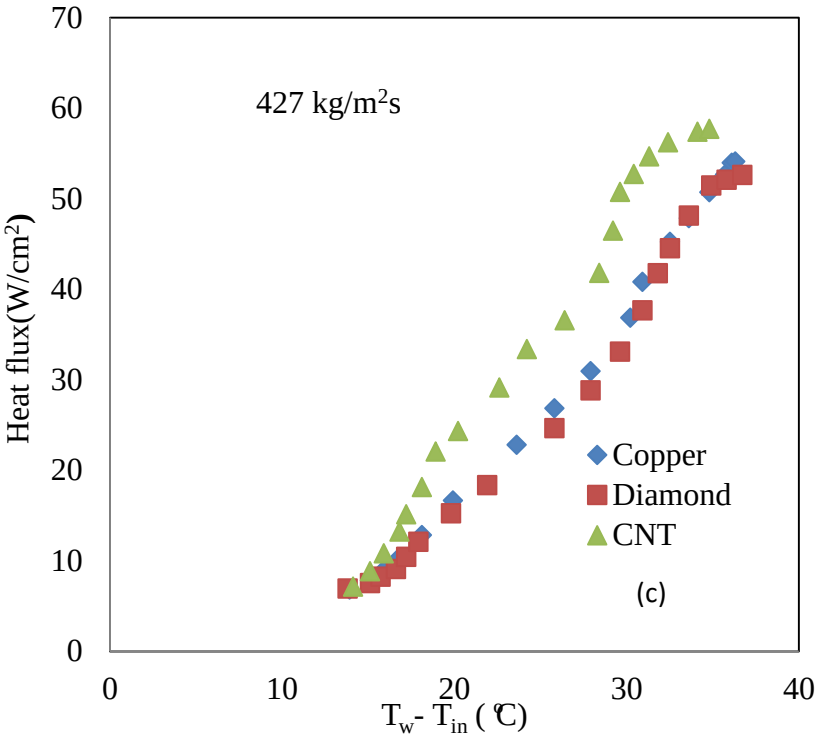

Figure 6.4. Flow boiling curve for fluxes of (a) 283, (b) 348, and (c) 427 kg/m^{2}s.

Figure 6.5 shows the variation in the CHF with mass flux. The measured CHF values from different substrate surfaces are summarized in Table 6.1. The figure shows that the CHF of all of the samples increases with increasing mass flux. At low mass flux, the CNT surface has a much higher CHF than the diamond or Cu surfaces. At high mass flux, the CHF differences are not as significant. At the lowest mass flux of 283 kg/m^{2}s, the CHF of the CNT coated surface is enhanced by 21.9% compared to the Cu surface, while the CHF of the diamond coated surface is reduced by 3.3% compared to the Cu surface. This abnormal behavior is due to the bending of the CNTs towards the surface at higher mass fluxes.

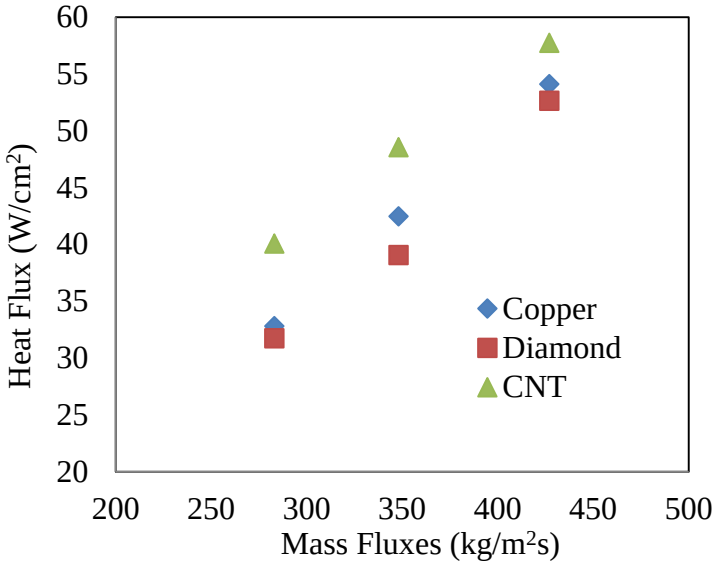

Figure 6.5. Variation of CHFs with mass flux.

Table 6.1. Measured CHF values of tested surfaces.

S1. No	Flow rates Kg/m^{2}s	CNTs	CHF (W/cm^2) Diamond	Sandblasted Cu
1	283	40.01	31.74	32.82
2	348	48.56	39.06	42.49
3	427	57.74	52.64	54.12

Figure 6.6 shows CNTs with a diamond interlayer after a strong flow flush and it is clear that the CNTs have been bent by the flow. The diminishing CHF enhancement is explained in Figure 6.7. At low mass flux, CNTs maintain their vertical direction which in turn increases the wall roughness and turbulence and thereby increases the CHF. At high mass flux, CNTs are bent by the strong flow and have reduced contact in the flow, and thus the heat transfer efficiency of the CNTs is reduced. Therefore, the CNTs with the diamond interlayer have reduced CHF at high mass flux. A similar mechanism was reported by Khanikar *et al.* [14].

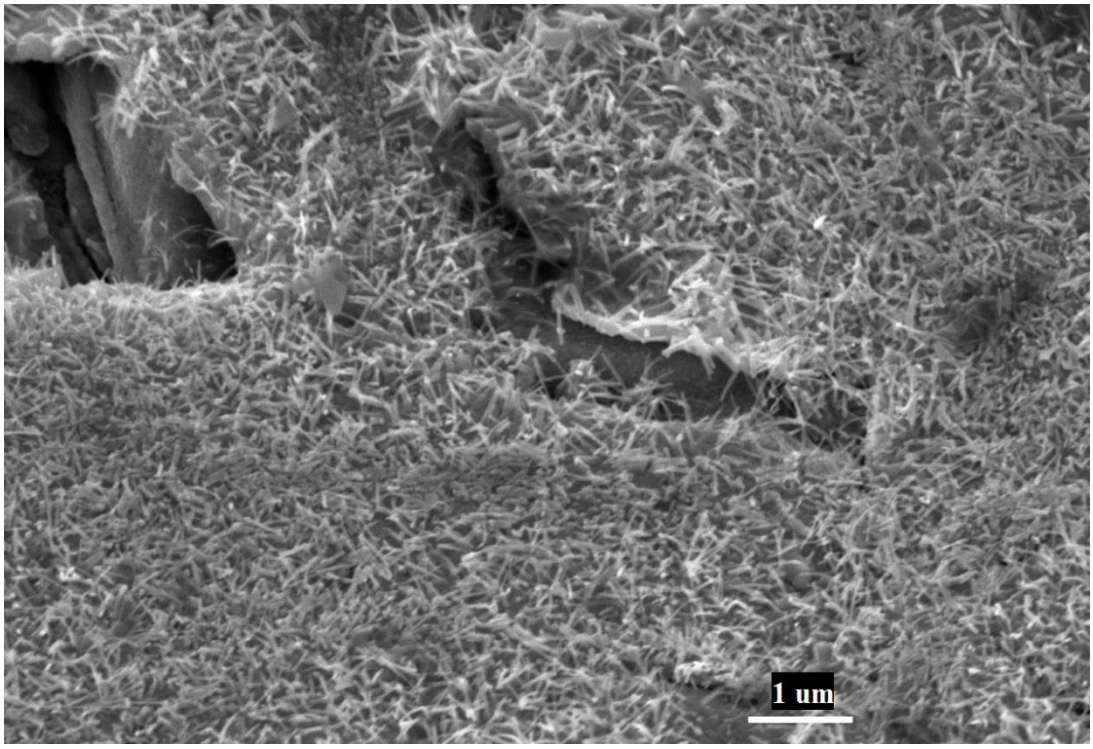

Figure 6.6. SEM image (SEI mode) of CNTs with a diamond interlayer after a strong flow flush.

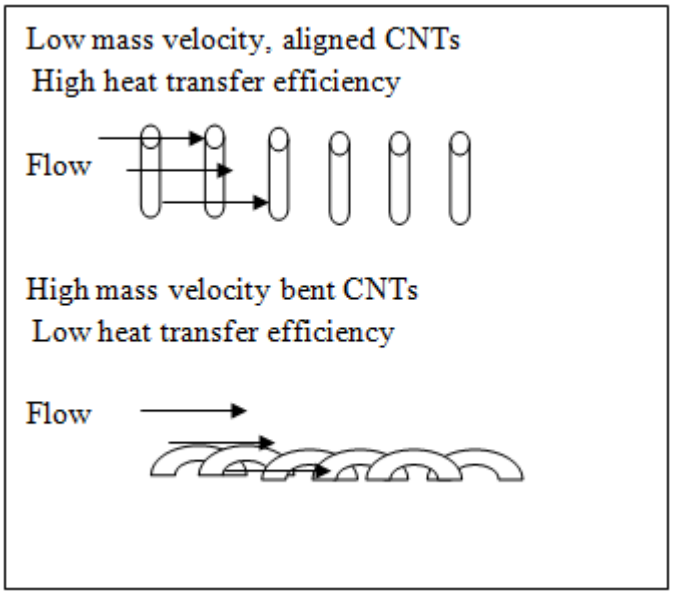

Figure 6.7. Schematic of CNTs with diminishing CHF at high mass flux.

Figure 6.8 presents the variation of the heat transfer coefficient with heat flux for three different samples. The heat transfer coefficient was calculated using equation 3.5. The CNT

coatings show a large enhancement in the heat transfer coefficient compared with the diamond coated samples or bare Cu. With an increase in the heat flux, the heat transfer coefficient of the CNTs increases. A maximum increase of 30.86% in the heat transfer coefficient was obtained for CNT coated surface compared with sandblasted Cu at a mass flow flux of 283 kg/m^2s. There are two factors that have influence on the heat transfer coefficient: bubble generation and flow rate [128, 129]. The CNT hydrophobic surface is ideal for bubble formation and the CNT fine structure helps bubbles escape to the flow. Higher heat transfer coefficients for the CNT coated surface are due to its high surface roughness, high heat transfer area, and fin action. But, for higher flow rates, the percent enhancement in heat transfer is reduced for CNT coated surfaces due to the high aspect ratio of the CNTs, causing them to bow towards the surface. For diamond coated samples, the heat transfer coefficient is higher than for bare Cu in the low heat flux region. This is probably due to early nucleation boiling. Due to its low wettability, more bubbles are produced and this leads to better heat transfer performance at low heat fluxes. In the high heat flux region, the heat transfer coefficient of diamond is less than for Cu, probably due to the abundant generation of large sized bubbles.

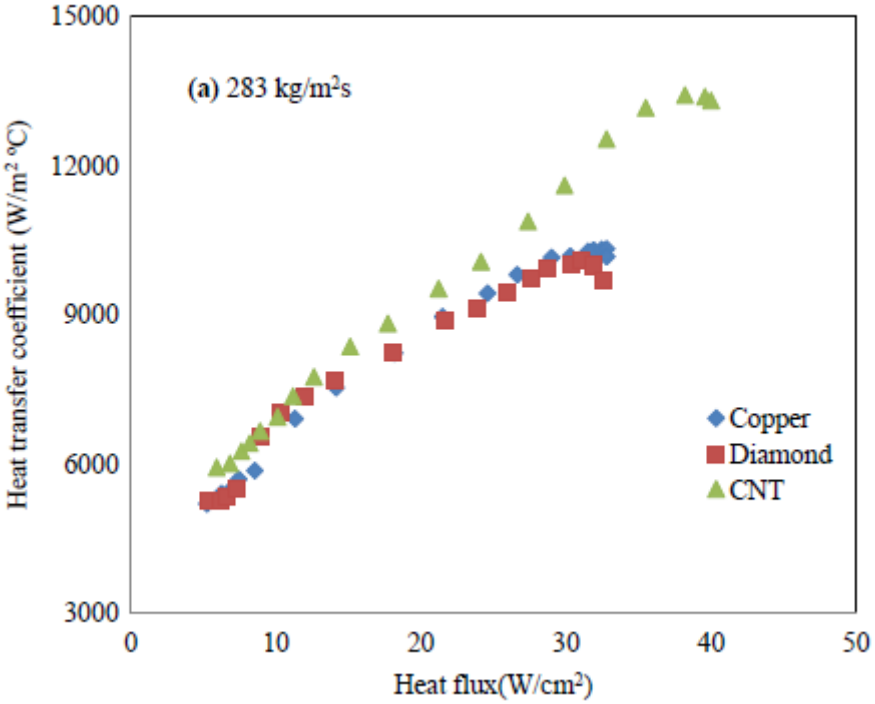
(a) 283 kg/m²s
Heat transfer coefficient (W/m² ℃)
Heat flux(W/cm²)
Copper
Diamond
CNT
15000
12000
9000
6000
3000
0
10
20
30
40
50

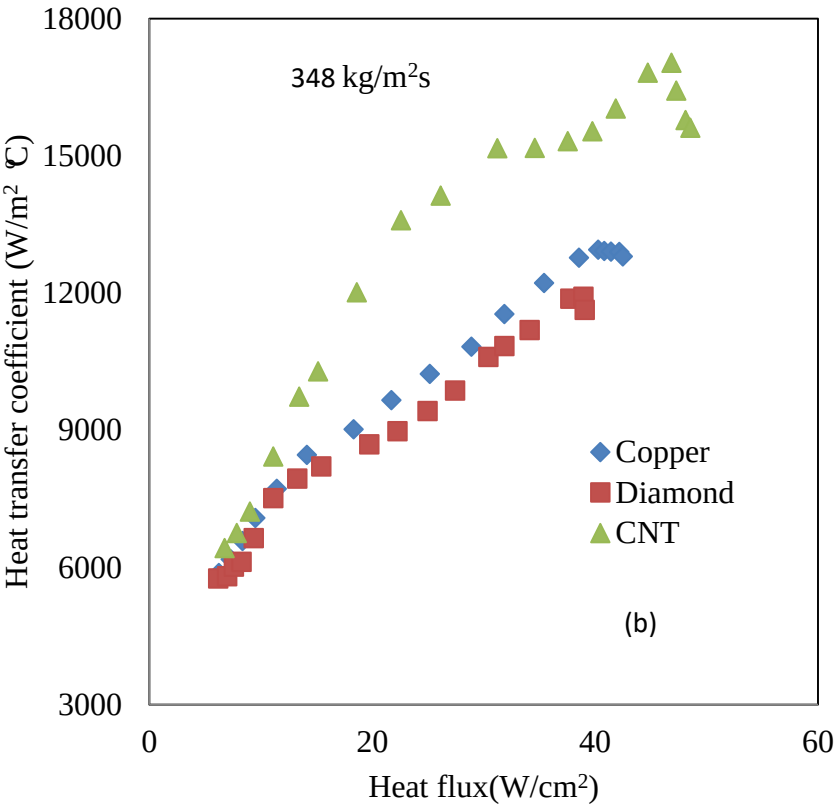
348 kg/m²s
Heat transfer coefficient (W/m² ℃)
Heat flux(W/cm²)
Copper
Diamond
CNT
(b)
18000
15000
12000
9000
6000
3000
0
20
40
60

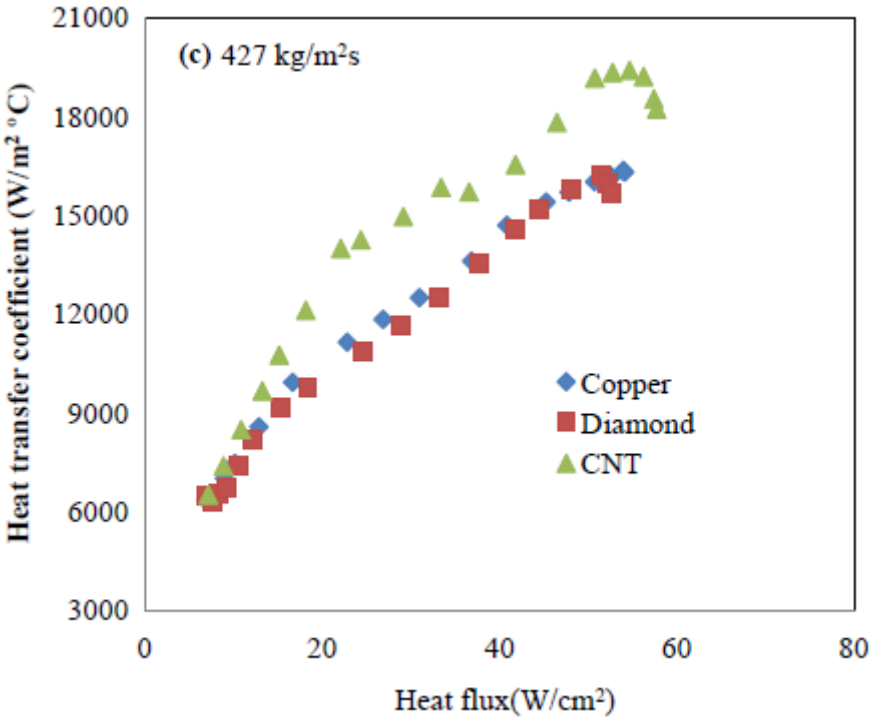

Figure 6.8. Variation of heat transfer coefficient with heat flux for mass flow fluxes of (a) 283, (b) 348, and (c) 427 kg/m^{2}s.

6.2 Wettability and Stability Measurement

The wettability with water of different surfaces was evaluated by measuring the contact angle of water on sample surfaces. Figure 6.9 shows the contact angle on sandblasted Cu, diamond thin films, and CNTs with a diamond interlayer coating. The contact angle of bare Cu is less than 90°, hence it is hydrophilic; for the diamond thin film coatings, the contact angle is around 90°; for the CNT coatings, it is approximately 133°, indicating it is hydrophobic.

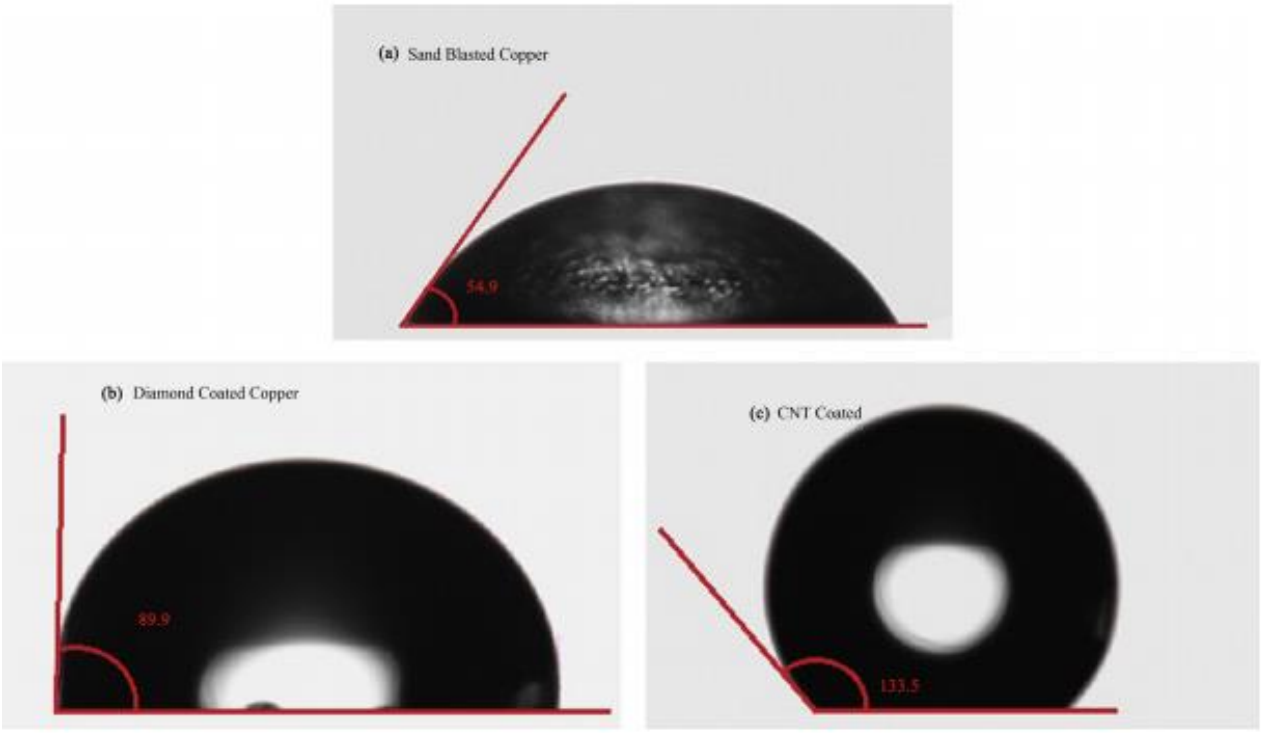

Figure 6.9. Static contact angle of (a) sandblasted Cu, (b) diamond coated Cu, and (c) CNT with diamond interlayer coated Cu substrates.

Surface wettability has a great influence on the flow boiling heat transfer [166]. At low heat flux conditions, hydrophobic surfaces will have low free energy for bubble onset. Bubbles generated by evaporation of liquid near the surface will absorb and transfer heat to the liquid. But, at high heat flux conditions, the bubble generation rate can be overwhelming which results in drying out at the heating surface. The dry out layer could reduce the heating surface contact with the liquid and thus dramatically reduce the heat transfer efficiency. The wettability with water was highest for bare Cu and lowest for the CNT coatings. Boiling will begin earlier for CNT and diamond coated Cu than for the bare Cu due to the early detachment of bubbles from the surfaces. This would enhance the boiling heat transfer performance of diamond and CNT coated surfaces in the low heat flux region. As the heat flux increases, the bubble density increases and reduces the boiling heat transfer performance of diamond but not CNTs Due to the fin action of CNTs hinders the growth of large bubbles. This action of the fins can enhance the flow boiling heat transfer characteristics of CNT

coated surfaces in the high heat flux region.

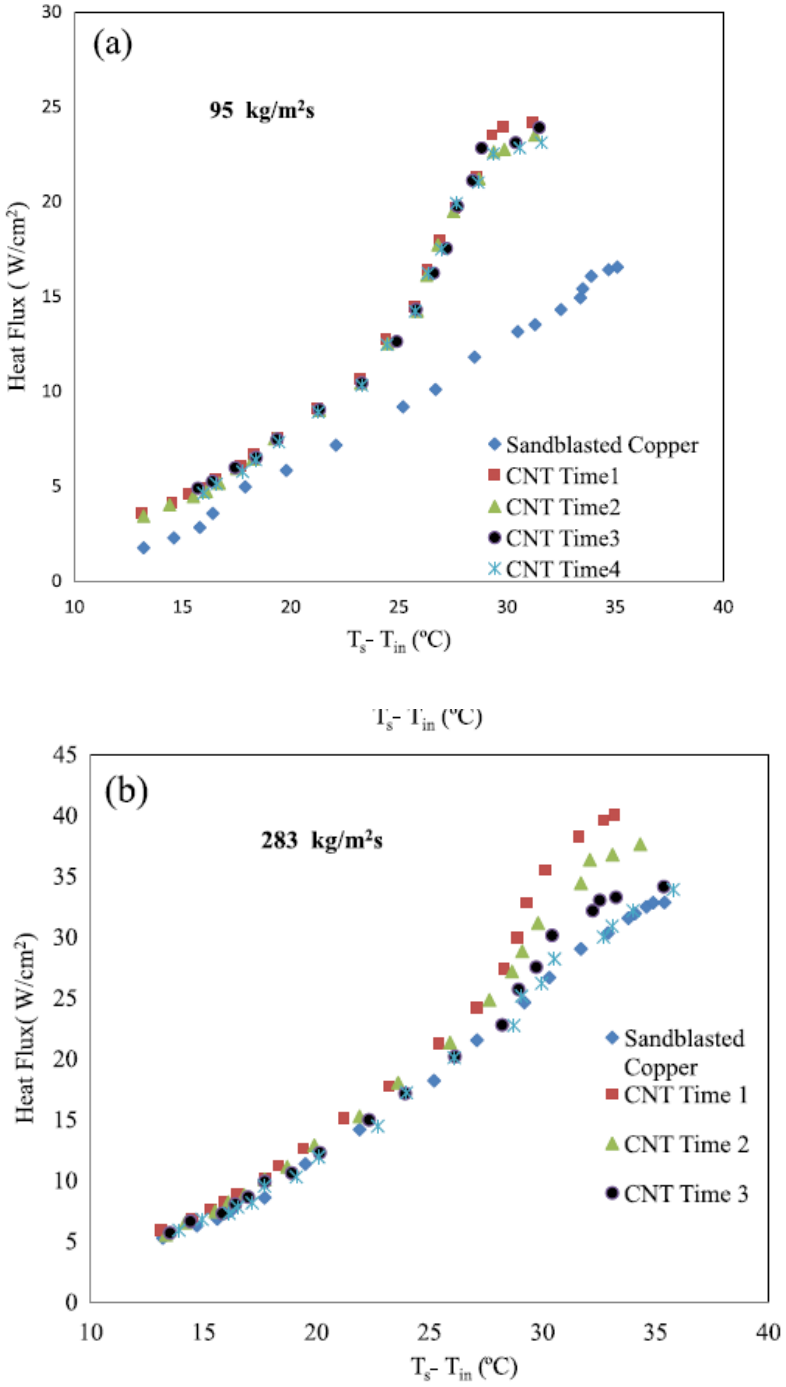

Figure 6.10. Stability analysis for subcooled flow boiling curves measured at (a) 95 and (b) 283 kg/m^{2}s.

Stability analysis of CNTs with a diamond interlayer was conducted for two mass fluxes, 95 and 283 kg/m^{2}s. Four sequential tests were repeated for a time period of 20 hours. Figure

6.10(a) shows the repeatable boiling curves for CNTs with a diamond interlayer surface with respect to time. Figure 6.10(b) shows an appreciable change in the boiling curve for CNTs with a diamond interlayer surface with respect to time. This appreciable change in boiling curve at the higher flow rate is due to the changes in morphology of the CNT surface with respect to time. The gradual decrease in CHF enhancement for the higher flow rate is due to the folding of CNTs towards the surface over time, which in turn reduces the spaces among the CNTs. However, at lower flow rates, this bending of the CNTs would take place slowly, so an appreciable change in CHF with respect to time cannot be observed.

CHAPTER 7

CONCLUSIONS AND SUGGESTIONS FOR FUTURE WORK

7.1 Conclusions

In this thesis, CNTs with a diamond interlayer were synthesized to overcome their limitations in FEE and FBHT applications. Diamond thin films with enhanced adhesion on Cu substrates and CNT emitters with better FEE performance were achieved. The FBHT performance of CNTs with a diamond interlayer was also investigated. The major findings and conclusions are summarized as follows:

(1) Sandblasting and Al modification treatments improved the adhesion of diamond thin films on Cu substrates. Sandblasting treatment improved the diamond thin film adhesion on the Cu substrate by enhancing the diamond nucleation density and mechanical interlocking. Al modification treatment improved the diamond thin film adhesion by forming an intermediate thin layer of alumina that prohibited the formation of graphite between the diamond thin film and the Cu substrate. In comparison with Fe-based substrates, the Cu substrates require a lower critical Al concentration to enhance diamond thin film adhesion.

(2) The adhesion of CNTs on Cu substrates was improved by using a diamond thin film interlayer. The adhesion strength was enhanced by direct C-C bonding between the diamond and the CNTs. This strong C-C bonding was attributed to tip growth CNTs on the diamond thin films generated by catalyst spin-coating treatment.

(3) The CNTs with a diamond interlayer have remarkably enhanced FEE stability (over 5000 minutes) compared with work by other researchers regarding CNT-based FEE emitters. The superior FEE stability was due to enhanced adhesion and contact between the diamond and the CNTs. The effects of substrate, with or without the diamond thin film interlayer, as well as the sp^2 content of the diamond interlayer on CNT FEE stability was investigated. Among them, use of a diamond interlayer plays a key role in enhancing CNT FEE stability.

(4) The effect of CNT density on the FEE turn-on field was investigated. By experimenting with catalyst spin-coating time, CNT emitters can be synthesized with an optimal density to result in a low FEE turn-on field.

(5) The effect of a diamond interlayer on the CNT FEE turn-on field was studied. The FEE turn-on field can be reduced by increasing the sp^2 phase concentration in the diamond interlayer. A band diagram of CNTs with a diamond interlayer was proposed. Based on the results of the work conducted here, the FEE turn-on field of the CNTs was reduced to as low as 5.1 V/μm while outstanding FEE stability was maintained; this is promising for FEE applications.

(6) The FBHT properties of CNTs with a diamond interlayer were studied. CNTs with a diamond interlayer have high heat transfer efficiency and good FBHT stability at low mass flux. But, at high mass flux, CNTs with a diamond interlayer do not have obviously better performance than bare Cu and diamond on Cu. This is due to the bending of the CNTs that occurs at high mass flux.

7.2 Suggestions for Future Work

(1) The CNTs synthesized in this thesis used Fe as the catalyst for CNT growth. This catalyst might be harmful for other applications that require high carbon purity. It has been reported that nanodiamond can serve as the catalyst for CNTs grown using CVD [99]. So, investigating the direct growth of CNTs on nanostructured diamond layers to obtain a pure carbon system without the addition of other elements is recommended.

(2) In this thesis, CNTs with a diamond thin film interlayer showed good FEE stability of over 5000 minutes. However, the FEE performance beyond that time is not known. Stability testing over a longer period of time is recommended.

(3) The FBHT properties of CNTs with a diamond interlayer were studied. However, the research presented in this thesis is limited. A systematic investigation of the effect of CNT properties (including diameter, length, density, and aspect ratio) on heat transfer efficiency is recommended.

(4) The surface of CNTs with a diamond interlayer demonstrated good FBHT efficiency at low mass flux. But, due to the folding of the CNTs, the performance at high mass flux is not ideal. Synthesis of diamond nanocones with better mechanical strength could be a better method to enhance FBHT performance at high mass flux.

REFERENCES

1. Terranova, M.L. Orlanducci, S. Rossi, M. Tamburri, E., Nanodiamonds for field emission: state of the art. Nanoscale, 2015. **7**(12): p. 5094-5114.
2. Xu, N.S. and S.E. Huq, *Novel cold cathode materials and applications.* Materials Science & Engineering R-Reports, 2005. **48**(2-5): p. 47-189.
3. Temple, D., *Recent progress in field emitter array development for high performance applications.* Materials Science & Engineering R-Reports, 1999. **24**(5): p. 185-239.
4. Bocharov, G.S. and A.V. Eletskii, *Theory of carbon nanotube (CNT)-based electron field emitters.* Nanomaterials, 2013. **3**(3): p. 393-442.
5. Zou, R. J. Hu, J. Q. Song, Y. L. Wang, N. Chen, H. H. Chen, H. H. Wu, J. H. Sun, Y. G. Chen, Z. G, *Carbon nanotubes as field emitter.* Journal of Nanoscience and Nanotechnology, 2010. **10**(12): p. 7876-7896.
6. Eletskii, A.V., *Carbon nanotube-based electron field emitters.* Physics-Uspekhi, 2010. **53**(9): p. 863-892.
7. Lim, S. C. Lee, K. Lee, I. H. Lee, Y. H., *Field emission and application of carbon nanotubes.* Nano, 2007. **2**(2): p. 69-89.
8. Saito, Y., *Carbon nanotube field emitter.* Journal of Nanoscience and Nanotechnology, 2003. **3**(1-2): p. 39-50.
9. Donaldson, L., *Diamond nanoparticles improve heat transfer.* Materials Today, 2014. **17**(5): p. 212-212.
10. Murshed, S.M.S. and C.A.N. de Castro, *Superior thermal features of carbon nanotubes-based nanofluids - A review.* Renewable & Sustainable Energy Reviews, 2014. **37**: p. 155-167.
11. Fan, Q.H., J. Gracio, and E. Pereira, *Free-standing diamond film preparation using copper substrate.* Diamond and Related Materials, 1997. **6**(2-4): p. 422-425.
12. Bonard, J. M. Klinke, C. Dean, K. A. Coll, B. F., *Degradation and failure of carbon nanotube field emitters.* Physical Review B, 2003. **67**(11).
13. Zhang, J. H. Wang, X. Yang, W. W. Yu, W. D. Feng, T. Li, Q. Liu, X. H. Yang, C. R., *Interaction between carbon nanotubes and substrate and its implication on field emission mechanism.* Carbon, 2006. **44**(3): p. 418-422.
14. Khanikar, V., I. Mudawar, and T. Fisher, *Effects of carbon nanotube coating on flow boiling in a micro-channel.* International Journal of Heat and Mass Transfer, 2009. **52**(15-16): p. 3805-3817.
15. Ujereh, S., T. Fisher, and I. Mudawar, *Effects of carbon nanotube arrays on nucleate pool boiling.* International Journal of Heat and Mass Transfer, 2007. **50**(19-20): p. 4023-4038.
16. Nilsson, L. Groening, O. Emmenegger, C. Kuettel, O. Schaller, E. Schlapbach, L. Kind, H. Bonard, J. M. Kern, K., *Scanning field emission from patterned carbon nanotube films.* Applied Physics Letters, 2000. **76**(15): p. 2071-2073.
17. Gruen, D.M., *Nanocrystalline diamond films.* Annual Review of Materials Science, 1999. **29**: p. 211-259.

18. Stöhr, J., *NEXAFS Spectroscopy*. Springer series in surface sciences. Vol. 25. 1996: Berlin ; New York : Springer
19. Nazare, M.H., A.J. Neves, *Properties, Growth and Applications of Diamond*. 2001, London, United Kingdom: INSPEC, the Instution of Electrical Engineers
20. Spear, K.E., J.P. Dismukes, *Synthetic Diamond - Emerging CVD Science and Technology*. 1994, NY: Wiley.
21. Werner, M., R. Locher, *Growth and application of undoped and doped diamond films.* Reports on Progress in Physics, 1998. **61**(12): p. 1665-1710.
22. Sussmann, R.S., *CVD diamond for electronic devices and sensors*. 2009, U.K.: Chichester: J. Wiley
23. Pehrsson, P.E., F.G. Celii, J.E. Butler, Chemical mechanisms of diamond CVD, In: *Diamond Films and Coatings, Development, Properties and Applications*, R.F. Davis, ed. 1993, NJ: Noyes, Park Ridge.
24. Kamo, M., Y. Sato, S. Matsumoto, N. Setaka, *Diamond synthesis from gas phase in microwave plasma.* Journal of Crystal Growth, 1983. **62**: p. 642-644
25. Paoletti, A., A. Tucciarone, *The Physics of Diamond*. 1997, Amsterdam, Washington, DC: IOS Press.
26. Yang, Q., W. Chen, C. Xiao, A. Hirose, M. Bradley, *Low temperature synthesis of diamond thin films through graphite etching in a microwave hydrogen plasma.* Carbon, 2005. **43**: p. 2635-2641.
27. Yellampalli, S., *Carbon Nanotubes-Synthesis, Characterization, Applications*. 2011: InTech.
28. Matsumoto, S., Y. Sato, M. Tsutsumi, N. Setaka, *Growth of diamond particles from methane-hydrogen gas.* Journal of Materials Science 1982. **17**: p. 3106-3112.
29. May, P.W., *Diamond thin films: a 21st-century material.* Phil. Trans. R. Soc. Lond, 2000. **358**: p. 473-495.
30. Mittal, K.L., *Adhesion measurement of Thin Films, Thick Films, and Bulk Coatings*. 1978: ASTM International.
31. Graystone, J., R. Kennedy, *Non-destructive measurement of coating adhesion.* Surface Coatings International, 2000. **83**(8): p. 389-398.
32. Bull, S.J., D.S. Rickerby, Evaluation of coatings. In: *Advanced Surface Coatings: A Handbook of Surface Engineering*, D.S. Rickerby and A. Matthews, eds. 1991, New York: Chapman and Hall Inc.
33. Ferro, S., *Synthesis of diamond.* Journal of Materials Chemistry, 2002. **12**(10): p. 2843-2855.
34. Huang, Z. Q. Xiang, B. He, Y. H. Huang, B. Y., *Thermal residual stress analysis of coated diamond grits.* International Journal of Minerals Metallurgy and Materials, 2009. **16**(2): p. 215-219.
35. Artini, C., M.L. Muolo, and A. Passerone, *Diamond-metal interfaces in cutting tools: a review.* Journal of Materials Science, 2012. **47**(7): p. 3252-3264.

36. Haubner, R. and W. Kalss, *Diamond deposition on hardmetal substrates - comparison of substrate pre-treatments and industrial applications.* International Journal of Refractory Metals & Hard Materials, 2010. **28**(4): p. 475-483.
37. Zhang, C. Z. Li, Y. S. Tang, Y. Yang, L. Zhang, L. Sun, Y. Yang, Q. Hirose, A., *Nanocrystalline diamond thin films grown on Ti_6Al_4V alloy.* Thin Solid Films, 2013. **527**: p. 59-64.
38. Liu, H.M. and D.S. Dandy, *Studies on nucleation process in diamond CVD - an overview of recent developments.* Diamond and Related Materials, 1995. **4**(10): p. 1173-1188.
39. Fan, Q.H., E. Pereira, and J. Gracio, *Diamond deposition on copper: studies on nucleation, growth, and adhesion behaviours.* Journal of Materials Science, 1999. **34**(6): p. 1353-1365.
40. Li, Y. S. Yang, L. Tang, Y. Zhang, C. Zhang, L. Onyeka, I. Yang, Q. Feng, R. Hirose, A., *Adherent nanocrystalline diamond coatings deposited on Ti substrate at moderate temperatures.* Surface & Coatings Technology, 2011. **206**(7): p. 1971-1976.
41. Li, X. J. He, L. L. Li, Y. S. Yang, Q. Hirose. A., *TEM interfacial characterization of CVD diamond film grown on Al inter-layered steel substrate.* Diamond and Related Materials, 2014. **50**: p. 103-109.
42. Li, Y. S. Yang, L. Z. Ma, H. T. Feng, R. F. Yang, Q. Hirose, A., *Enhanced diamond deposition on Kovar alloy substrate with Al interlayer.* Materials Research Innovations, 2014. **18**: p. 979-982.
43. Li, X. J. He, L. L. Li, Y. S. Yang, Q. Hirose, A., *Direct coating adherent diamond films on Fe-based alloy substrate: the roles of Al, Cr in enhancing interfacial adhesion and promoting diamond growth.* ACS Applied Materials & Interfaces, 2013. **5**(15): p. 7370-7378.
44. Li, Y. S. Tang, Y. Yang, Q. Xiao, C. Hirose, A., *Al-enhanced low temperature deposition of diamond thin films on hetero-substrates.* Materials Chemistry and Physics, 2009. **116**(2-3): p. 649-653.
45. Lu, F. X. Tang, W. Z. Miao, J. Q. He, L. F. Li, C. M. Chen, G. C., *Novel pretreatment of hard metal substrate for better performance of diamond coated cutting tools.* 14th Congress of International Federation for Heat Treatment and Surface Engineering, Vols 1 and 2, Proceedings, 2004: p. 35-40.
46. Murakawa, M. and S. Takeuchi, *Substrate treatments modifications to improve the adhesion of diamond-coated cutting inserts.* Journal of Adhesion Science and Technology, 1995. **9**(6): p. 695-710.
47. Iijima, S., *Helical microtubules of graphitic carbon.* Nature, 1991. **354**(6348): p. 56-58.
48. Meyyappan, M., *Carbon nanotubes : science and applications*. 2005: Boca Raton, FL : CRC Press.
49. Saito, R. Fujita, M. Dresselhaus, G. Dresselhaus, M. S., *Electronic-structure of chiral graphene tubules.* Applied Physics Letters, 1992. **60**(18): p. 2204-2206.

50. Mintmire, J.W., B.I. Dunlap, and C.T. White, *Are fullerene tubules metallic.* Physical Review Letters, 1992. **68**(5): p. 631-634.
51. Blase, X. Benedict, L. X. Shirley, E. L. Louie, S. G., *Hybridization effects and metallicity in small radius carbon nanotubes.* Physical Review Letters, 1994. **72**(12): p. 1878-1881.
52. Lu, J.P., *Elastic properties of carbon nanotube and nanoropes.* Physical Review Letters, 1997. **79**(7): p. 1297-1300.
53. Garg, A., J. Han, and S.B. Sinnott, *Interactions of carbon-nanotubule proximal probe tips with diamond and graphene.* Physical Review Letters, 1998. **81**(11): p. 2260-2263.
54. Hone, J., M.W., C. Piskoti, and A. Zettl, *Thermal conductivity of single-walled carbon nanotubes.* Physical Review B, 1999. **59**(4): p. R2514-R2516.
55. Yellampalli, S., *Carbon Nanotubes - Polymer Nanocomposites*. 2011: InTech.
56. Meyyappan, M. Delzeit, L. Cassell, A. Hash, D., *Carbon nanotube growth by PECVD: a review.* Plasma Sources Science & Technology, 2003. **12**(2): p. 205-216.
57. Li, Y. M. Kim, W. Zhang, Y. G. Rolandi, M. Wang, D. W. Dai, H. J., *Growth of single-walled carbon nanotubes from discrete catalytic nanoparticles of various sizes.* Journal of Physical Chemistry B, 2001. **105**(46): p. 11424-11431.
58. Prasek, J. Drbohlavova, J. Chomoucka, J. Hubalek, J. Jasek, O. Adam, V. Kizek, R., *Methods for carbon nanotubes synthesis-review.* Journal of Materials Chemistry, 2011. **21**(40): p. 15872-15884.
59. Simate, G. S. Moothi, K. Meyyappan, M. Iyuke, S. E. Ndlovu, S. Falcon, R. Heydenrych, M., *Kinetic model of carbon nanotube production from carbon dioxide in a floating catalytic chemical vapour deposition reactor.* RSC Advances, 2014. **4**(19): p. 9564-9572.
60. Lim, S.H. and J.Y. Lin, *Synthesis of carbon nanotubes.* Carbon Nanotubes and Their Applications, 2012. **1**: p. 31-72.
61. Journet, C., M. Picher, and V. Jourdain, *Carbon nanotube synthesis: from large-scale production to atom-by-atom growth.* Nanotechnology, 2012. **23**(14).
62. Boskovic, B. O. Stolojan, V. Khan, R. U. A. Haq, S. Silva, S. R. P., *Large-area synthesis of carbon nanofibres at room temperature.* Nature Materials, 2002. **1**(3): p. 165-168.
63. Ryu, K. M. Kang, M. Y. Kim, Y. D. Jeon, H. T., *Low-temperature growth of carbon nanotube by plasma-enhanced chemical vapor deposition using nickel catalyst.* Japanese Journal of Applied Physics Part 1-Regular Papers Brief Communications & Review Papers, 2003. **42**(6A): p. 3578-3581.
64. Baker, R. T. K. Harris, P. S. Thomas, R. B. Waite, R. J., *Formation of filamentous carbon from iron, cobalt and chromium catalyzed decomposition of acetylene.* Journal of Catalysis, 1973. **30**(1): p. 86-95.
65. Baker, R.T.K., *Catalytic growth of carbon filaments.* Carbon, 1989. **27**(3): p. 315-323.

66. Baker, R. T. K., M.A. Barber, P. S. Harris, F. S. Feates and R. J. Waitem, *Nucleation and growth of carbon deposits from the nickel catalyzed decomposition of acetylene.* Catalysis, 1972. **26**: p. 51-62.
67. Tibbetts, G.G., *Why are carbon filaments tubular.* Journal of Crystal Growth, 1984. **66**(3): p. 632-638.
68. Tumilty, N. Kasharina, L. Prokhoda, T. Sinelnikov, B. Jackman, R. B.,*Synthesis of carbon nanotubes on single crystal diamond.* Carbon, 2010. **48**(11): p. 3027-3032.
69. Meyyappan, M., *Catalyzed chemical vapor deposition of one-dimensional nanostructures and their applications.* Progress in Crystal Growth and Characterization of Materials, 2009. **55**(1-2): p. 1-21.
70. Wang, Y. Y. Luo, Z. Q. Li, B. Ho, P. S. Yao, Z. Shi, L. Bryan, E. N. Nemanich, R. J., *Comparison study of catalyst nanoparticle formation and carbon nanotube growth: Support effect.* Journal of Applied Physics, 2007. **101**(12).
71. Merkulov, V. I. Melechko, A. V. Guillorn, M. A. Lowndes, D. H. Simpson, M. L., *Alignment mechanism of carbon nanofibers produced by plasma-enhanced chemical-vapor deposition.* Applied Physics Letters, 2001. **79**(18): p. 2970-2972.
72. Lan, Y.C., Y. Wang, and Z.F. Ren, *Physics and applications of aligned carbon nanotubes.* Advances in Physics, 2011. **60**(4): p. 553-678.
73. Kim, M. J. Choi, J. H. Park, J. B. Kim, S. K. Yoo, J. B. Park, C. Y., *Growth characteristics of carbon nanotubes via aluminum nanopore template on Si substrate using PECVD.* Thin Solid Films, 2003. **435**(1-2): p. 312-317.
74. Melechko, A. V. Merkulov, V. I. McKnight, T. E. Guillorn, M. A. Klein, K. L. Lowndes, D. H. Simpson, M. L., *Vertically aligned carbon nanofibers and related structures: Controlled synthesis and directed assembly.* Journal of Applied Physics, 2005. **97**(4).
75. Sui, Y. C. Cui, B. Z. Guardian, R. Acosta, D. R. Martinez, L. Perez, R., *Growth of carbon nanotubes and nanofibres in porous anodic alumina film.* Carbon, 2002. **40**(7): p. 1011-1016.
76. Lee, O. J. Hwang, S. K. Jeong, S. H. Lee, P. S. Lee, K. H., *Synthesis of carbon nanotubes with identical dimensions using an anodic aluminum oxide template on a silicon wafer.* Synthetic Metals, 2005. **148**(3): p. 263-266.
77. Yang, Q., C.X., W. Chen, A.K. Singh, T. Asai, A. Hirose, *Growth mechanism and orientation control of well-aligned carbon nanotubes.* Diamond and Related Materials, 2003. **12**: p. 1482-1487.
78. W. Yi, Q.Y., *Aligned growth and alignment mechanism of carbon nanotubes by hot filament chemical vapor deposition.* Applied Physics A-Materials Science & Processing, 2010. **98**: p. 659-669.
79. Chen, L. H. AuBuchon, J. F. Gapin, A. Daraio, C. Bandaru, P. Jin, S. Kim, D. W. Yoo, I. K. Wang, C. M., *Control of carbon nanotube morphology by change of applied bias field during growth.* Applied Physics Letters, 2004. **85**(22): p. 5373-5375.
80. Chhowalla, M. Teo, K. B. K. Ducati, C. Rupesinghe, N. L. Amaratunga, G. A. J.

Ferrari, A. C. Roy, D. Robertson, J. Milne, W. I., *Growth process conditions of vertically aligned carbon nanotubes using plasma enhanced chemical vapor deposition.* Journal of Applied Physics, 2001. **90**(10): p. 5308-5317.
81. Merkulov, V. I. Lowndes, D. H. Wei, Y. Y. Eres, G. Voelkl, E., *Patterned growth of individual and multiple vertically aligned carbon nanofibers.* Applied Physics Letters, 2000. **76**(24): p. 3555-3557.
82. Merkulov, V. I. Melechko, A. V. Guillorn, M. A. Simpson, M. L. Lowndes, D. H. Whealton, J. H. Raridon, R. J., *Controlled alignment of carbon nanofibers in a large-scale synthesis process.* Applied Physics Letters, 2002. **80**(25): p. 4816-4818.
83. Yang, Q., W.C., C. Xiao, R. Sammynaiken, A. Hirose, *Synthesis of diamond films and nanotips through graphite etching.* Carbon 2005. **43**: p. 748-754.
84. Yang, Q. Q. Yang, S. L. Xiao, C. J. Hirose, A., *transformation of carbon nanotabes to diamond in microwave hydrogen plasma.* Materials Letters, 2007. **61**(11-12): p. 2208-2211.
85. Sun, L. T. Gong, J. L. Zhu, D. Z. Zhu, Z. Y. He, S. X., *Diamond nanorods from carbon nanotubes.* Advanced Materials, 2004. **16**(20): p. 1849-1853.
86. Rakha, S. A. Yu, G. J. Cao, J. Q. He, S. X. Zhou, X. T., *Diamond-graphite nanorods produced by microwave plasma chemical vapor deposition.* Diamond and Related Materials, 2010. **19**(4): p. 284-287.
87. Vlasov, I. L. Lebedev, O. I. Ralchenko, V. G. Goovaerts, E. Bertoni, G. Van Tendeloo, G. Konov, V. I., *Hybrid diamond-graphite nanowires produced by microwave plasma chemical vapor deposition.* Advanced Materials, 2007. **19**(22): p. 4058-+.
88. Cao, W.K.W.A.L.M., *Transformation of carbon nanotubes to diamond at high pressure and high temperature.* Russian Physical Journal, 2001. **44**: p. 178-182.
89. Zhang, F. M. Shen, J. Sun, J. F. Zhu, Y. Q. Wang, G. McCartney, G., *Conversion of carbon nanotubes to diamond by spark plasma sintering.* Carbon, 2005. **43**(6): p. 1254-1258.
90. Sun, L. T. Gong, J. L. Zhu, Z. Y. Zhu, D. Z. He, S. X. Wang, Z. X. Chen, Y. Hu, G., *Nanocrystalline diamond from carbon nanotubes.* Applied Physics Letters, 2004. **84**(15): p. 2901-2903.
91. Banhart, F. and P.M. Ajayan, *Carbon onions as nanoscopic pressure cells for diamond formation.* Nature, 1996. **382**(6590): p. 433-435.
92. Wen, B. Zhao, J. J. Li, T. J. Dong, C. Jin, J. Z., *N-diamond from catalysed carbon nanotubes: synthesis and crystal structure.* Journal of Physics-Condensed Matter, 2005. **17**(48): p. L513-L519.
93. Terranova, M. L. Orlanducci, S. Fiori, A. Tamburri, E. Sessa, V. Rossi, M. Barnard, A. S., *Controlled evolution of carbon nanotubes coated by nanodiamond: the realization of a new class of hybrid nanomaterials.* Chemistry of Materials, 2005. **17**(12): p. 3214-3220.
94. Muniz, A. R. Singh, T. Aydil, E. S. Maroudas, D., *Analysis of diamond nanocrystal formation from multiwalled carbon nanotubes.* Physical Review B, 2009. **80**(14).

95. Barnard, A.S., M.L. Terranova, and M. Rossi, *Density functional study of H-induced defects as nucleation sites in hybrid carbon nanomaterials.* Chemistry of Materials, 2005. **17**(3): p. 527-535.
96. Orlanducci, S. Tamburri, E. Terranova, M. L. Rossi, M., *Nanodiamond-coated carbon nanotubes: Early stage of the CVD growth process.* Chemical Vapor Deposition, 2008. **14**(7-8): p. 241-246.
97. Shankar, N. Glumac, N. G. Yu, M. F. Vanka, S. P., *growth of Nanodiamond/carbon-nanotube composites with hot filament chemical vapor deposition.* Diamond and Related Materials, 2008. **17**(1): p. 79-83.
98. Fernandes, A. J. S. Pinto, M. Neto, M. A. Oliveira, F. J. Silva, R. F. Costa, F. M., *Nano carbon hybrids from the simultaneous synthesis of CNT/NCD by MPCVD.* Diamond and Related Materials, 2009. **18**(2-3): p. 160-163.
99. Takagi, D., Y. Kobayashi, and Y. Hommam, *Carbon nanotube growth from diamond.* Journal of the American Chemical Society, 2009. **131**(20): p. 6922-+.
100. Wang, B., C.Y. Shu, and C.R. Wang, *Metal-free preparation of multi-walled carbon nanotubes based on new-diamond-induced growth mechanism.* Journal of Materials Chemistry, 2010. **20**(34): p. 7104-7106.
101. Shenderova, O.A., D.M. Gruen, *Ultrananocrystalline Diamond*. 2012, Oxford: Elsevier.
102. Horner, D. A. Sternberg, M. Zapol, P. Curtiss, L. A., *Carbon nanotunnels form from single-walled carbon nanotubes interacting with a diamond (100)-(2 x 1) surface.* Diamond and Related Materials, 2011. **20**(8): p. 1103-1109.
103. Lu, X., *Field electron emission from diamond and related films synthesized by plasma enhanced chemical vapor deposition.* Ph.D. Thesis, Physics and Engineering Physics, 2006, University of Saskatchewan: Saskatoon.
104. Richardson, O.W., *On the extraction of electrons from cold conductors in intense electric fields.* Proceedings of the Royal Society of London Series A-Containing Papers of a Mathematical and Physical Character, 1928. **117**(778): p. 719-730.
105. Dushman, S., *Electron emission from metals as a function of temperature.* Physical Review, 1923. **21**(6): p. 0623-0636.
106. Bandic, Z. Z. Bridger, P. M. Piquette, E. C. McGill, T. C. Vaudo, R. P. Phanse, V. M. Redwing, J. M., *High voltage (450 V) GaN schottky rectifiers.* Applied Physics Letters, 1999. **74**(9): p. 1266-1268.
107. Fowler, R.H. and L. Nordheim, *Electron emission in intense electric fields.* Proceedings of the Royal Society of London Series A-Containing Papers of a Mathematical and Physical Character, 1928. **119**(781): p. 173-181.
108. Zhao, G. P. Zhang, J. Zhang, Q. Zhang, H. Zhou, O. Qin, L. C. Tang, J., *Fabrication and characterization of single carbon nanotube emitters as point electron sources.* Applied Physics Letters, 2006. **89**(19).
109. Varshney, D., B.R. Weiner, and G. Morell, *Growth and field emission study of a monolithic carbon nanotube/diamond composite.* Carbon, 2010. **48**(12): p. 3353-3358.

110. Saito, R., G. Dresselhaus, and M.S. Dresselhaus, *Trigonal warping effect of carbon nanotubes.* Physical Review B, 2000. **61**(4): p. 2981-2990.
111. Aygun, G., G.R., T. Erlbacher, M. Wolf, M. Schellenberger, and L. Pfitzner, *Impact of temperature increments on tunneling barrier height and effective electron mass for plasma nitrided thin SiO_2 layer on a large wafer area.* Journal of Applied Physics, 2010. **108**(073304).
112. Lilienfeld, J.E., *A new instrument for measuring X-radiation.* American Journal of Roentgenology, 1922. **9**: p. 192.
113. Cui, J.B., J. Ristein, and L. Ley, *Electron affinity of the bare and hydrogen covered single crystal diamond (111) surface.* Physical Review Letters, 1998. **81**(2): p. 429-432.
114. X. Lu, Q. Yang, C. Xiao, A. Hirose, *Field electron emission characteristics of chemical vapor deposition diamond films with controlled sp^2 phase concentration.* Thin Solid Films, 2008. **516**: p. 4217-4221.
115. Jo, S. H. Tu, Y. Huang, Z. P. Carnahan, D. L. Wang, D. Z. Ren, Z. F., *Effect of length and spacing of vertically aligned carbon nanotubes on field emission properties.* Applied Physics Letters, 2003. **82**(20): p. 3520-3522.
116. Bonard, J. M. Salvetat, J. P. Stockli, T. de Heer, W. A. Forro, L. Chatelain, A., *Field emission from single-wall carbon nanotube films.* Applied Physics Letters, 1998. **73**(7): p. 918-920.
117. Bocharov, G.S. and A.V. Eletskii, *Degradation of a CNT-based field emission cathode due to ion sputtering.* Fullerenes Nanotubes and Carbon Nanostructures, 2012. **20**(4-7): p. 444-450.
118. Wang, Z.L., P. Poncharal, and W.A. de Heer, *Nanomeasurements of individual carbon nanotubes by in situ TEM.* Pure and Applied Chemistry, 2000. **72**(1-2): p. 209-219.
119. Lahiri, I. Seelaboyina, R. Hwang, J. Y. Banerjee, R. Choi, W. B., *Enhanced field emission from multi-walled carbon nanotubes grown on pure copper substrate.* Carbon, 2010. **48**(5): p. 1531-1538.
120. Guglielmotti, V. Chieppa, S. Orlanducci, S. Tamburri, E. Toschi, F. Terranova, M. L. Rossi, M., *Carbon nanotube/nanodiamond structures: An innovative concept for stable and ready-to-start electron emitters.* Applied Physics Letters, 2009. **95**(22).
121. Park, C. K. Kim, J. P. Yun, S. J. Kim, Y. K. Kim, W. Kim, J. U. Park, J. S., *Field-emission properties of carbon nanotubes grown on a submicron-sized tungsten tip in terms of various buffer layers.* Diamond and Related Materials, 2008. **17**(7-10): p. 1826-1830.
122. Srividya, S. Gautam, S. Jha, P. Kumar, P. Kumar, A. Ojha, U. S. Rawat, J. S. B. S. Pal, S. Chaudhary, P. K. Harsh, B. Sinha, R. K., *Titanium buffer layer for improved field emission of CNT based cold cathode.* Applied Surface Science, 2010. **256**(11): p. 3563-3566.

123. Moore, G.E., *Cramming more components onto integrated circuits (Reprinted from Electronics, pg 114-117, April 19, 1965).* Proceedings of the IEEE, 1998. **86**(1): p. 82-85.
124. Kalaiselvam, S. Gugan, M. S. Kuraloviyan, E. Meganathan, R. Niruthiya, P. A. Swaminathan, M. R., *Experimental investigation of anodized/spray pyrolysed nanoporous structure on heat transfer augmentation.* Journal of Thermal Science, 2009. **18**(4): p. 358-363.
125. Qu, W.L. and I. Mudawar, *A systematic methodology for optimal design of two-phase micro-channel heat sinks.* Journal of Electronic Packaging, 2005. **127**(4): p. 381-390.
126. Qu, W.L. and I. Mudawar, *Measurement and correlation of critical heat flux in two-phase micro-channel heat sinks.* International Journal of Heat and Mass Transfer, 2004. **47**(10-11): p. 2045-2059.
127. Qu, W.L. and I. Mudawar, *Transport phenomena in two-phase micro-channel heat sinks.* Journal of Electronic Packaging, 2004. **126**(2): p. 213-224.
128. Qu, W.L. and I. Mudawar, *Glow boiling heat transfer in two-phase micro-channel heat sinks - I. Experimental investigation and assessment of correlation methods.* International Journal of Heat and Mass Transfer, 2003. **46**(15): p. 2755-2771.
129. Singh, N. Sathyamurthy, V. Peterson, W. Arendt, J. Banerjee, D., *Flow boiling enhancement on a horizontal heater using carbon nanotube coatings.* International Journal of Heat and Fluid Flow, 2010. **31**(2): p. 201-207.
130. Sujith Kumar, C.S, S. Suresh, K. Rajiv, *Heat transfer enhancement by nano structured carbon nanotube coating.* International Journal of Scientific and Engineering Research, 2012. **3**: p. 1-5.
131. Tong, T. Zhao, Y. Delzeit, L. Kashani, A. Meyyappan, M. Majumdar, A., *Dense, Vertically aligned multiwalled carbon nanotube arrays as thermal interface materials.* IEEE Transactions on Components and Packaging Technologies, 2007. **30**(1): p. 92-100.
132. Lee, H. Sim, S. Kim, T. Goak, J. Lee, N., *Improvement of field emission characteristics of carbon nanotubes by enhancing physical and electrical contacts.* 2012 25th International Vacuum Nanoelectronics Conference (IVNC), 2012: p. 314-315.
133. Ushiki, T. and T. Fujita, *Backscattered electron imaging - its application to biological specimens stained with heavy-metals.* Archivum Histologicum Japonicum, 1986. **49**(1): p. 139-154.
134. Schrader, B., *Infrared and Raman Spectroscopy, Method and Application*. 1995, Weinheim, New York: VCH Verlagsgesellschaft mbH.
135. Field, J.E. (ed.), *The Properties of Diamond*. 1979, London: Academic Press
136. Morell, G. Gonzalez-Berrios, A. Weiner, B. R. Gupta, S., *Synthesis, structure, and field emission properties of sulfur-doped nanocrystalline diamond.* Journal of Materials Science-Materials in Electronics, 2006. **17**(6): p. 443-451.
137. Hiramatsu, M. Kato, K. Lau, C. H. Foord, J. S. Hori, M., *Measurement of C-2 radical density in microwave methane/hydrogen plasma used for nanocrystalline diamond*

film formation. Diamond and Related Materials, 2003. **12**(3-7): p. 365-368.
138. Watts, B., L. Thomsen, and P.C. Dastoor, *Methods in carbon K-edge NEXAFS: Experiment and analysis.* Journal of Electron Spectroscopy and Related Phenomena, 2006. **151**(2): p. 105-120.
139. Erasmus, R. M. Comins, J. D. Mofokeng, V. Martin, Z., *Application of Raman spectroscopy to determine stress in polycrystalline diamond tools as a function of tool geometry and temperature.* Diamond and Related Materials, 2011. **20**(7): p. 907-911.
140. Kohzaki, M. Higuchi, K. Noda, S. Uchida, K., *Large-area diamond deposition and brazing of the diamond films on steel substrates for tribological applications.* Diamond and Related Materials, 1993. **2**(5-7): p. 612-616.
141. Maeder, G., J.L. Lebrun, and J.M. Sprauel,*Present possibilities for the X-ray-diffraction method of stress measurement.* NDT International, 1981. **14**(5): p. 235-247.
142. Pinheiro, B. Lesage, J. Pasqualino, I. Bemporad, E. Benseddiq, N., *X-ray diffraction study of microstructural changes during fatigue damage initiation in pipe steels: Role of the initial dislocation structure.* Materials Science and Engineering A-Structural Materials Properties Microstructure and Processing, 2013. **580**: p. 1-12
143. Smith, R.L., G.E. Sandland, *An accurate method of determining the hardness of metals, with particular reference to those of a high degree of hardness*. In: *Proceedings of the Institution of Mechanical Engineers*, Vol. I, 1922, p. 623-641.
144. Chandler, H., *Hardness testing, Materials Park*. 1999, OH: ASM International.
145. Y. Mitsuda, Y. Kojima, T. Yoshida, and K. Akashi, *The growth of diamond in microwave plasma under low pressure*. Journal of Materials Science, 1987. **22**: 1557-1562.
146 G. N. Ayre, T. Uchino, B. Mazumder, A. L. Hector, J. L. Hutchison, D. C. Smith, P. Ashburn, and C. H. de. Groot, On the mechanism of carbon nanotube formation: the role of the catalyst. Journal of Physics: Condesed Matter, 2011. 23: 394201.
147. Khanikar, V., I. Mudawar, and T.S. Fisher, *Flow boiling in a micro-channel coated with carbon nanotubes.* IEEE Transactions on Components and Packaging Technologies, 2009. **32**(3): p. 639-649.
148. Morshed, A. K. M. M. Yang, F. H. Ali, M. Y. Khan, J. A. Li, C., *Enhanced flow boiling in a microchannel with integration of nanowires.* Applied Thermal Engineering, 2012. **32**: p. 68-75.
149. Singh, R. K. Gilbert, D. R. FitzGerald, J. Harkness, S. Lee, D. G., *Engineered interfaces for adherent diamond coatings on large thermal-expansion coefficient mismatched substrates.* Science, 1996. **272**(5260): p. 396-398.
150. Li, Y.S. and A. Hirose, *The effects of substrate compositions on adhesion of diamond films deposited on Fe-base alloys.* Surface & Coatings Technology, 2007. **202**(2): p. 280-287.
151. Grabke, H.J., R. Krajak, and J.C.N. Paz, *On the mechanism of catastrophic carburization - metal dusting.* Corrosion Science, 1993. **35**(5-8): p. 1141-1150.
152. Jiang, N. Wang, L. C. Won, J. H. Jeon, M. H. Mori, Y. Hatta, A. Ito, T. Sasaki, T.

Hiraki, A., *Interfacial analysis of CVD diamond on copper substrates.* Diamond and Related Materials, 1997. **6**(5-7): p. 743-746.
153. Munoz, R. and C. Gomez-Aleixandre, *Review of CVD synthesis of graphene.* Chemical Vapor Deposition, 2013. **19**(10-12): p. 297-322.
154. Gruen, D. M. Krauss, A. R. Zuiker, C. D. Csencsits, R. Terminello, L. J. Carlisle, J. A. Jimenez, I. Sutherland, D. G. J. Shuh, D. K. Tong, W. Himpsel, F. J., *Characterization of nanocrystalline diamond films by core-level photoabsorption.* Applied Physics Letters, 1996. **68**(12): p. 1640-1642.
155. Forbes, R.G., *Field emission: New theory for the derivation of emission area from a Fowler-Nordheim plot.* Journal of Vacuum Science & Technology B, 1999. **17**(2): p. 526-533.
156. Kim, J. P. Kim, Y. K. Park, C. K. Choi, H. Y. Kim, J. U. Park, J. S., *Direct growth of carbon nanotubes on a micro-sized cobalt tip and characterization of electron-emission properties.* Thin Solid Films, 2008. **517**(3): p. 1136-1140.
157. Kim, J. P. Kim, Y. K. Park, C. K. Choi, H. Y. Shon, C. H. Kim, J. U. Park, J. S., *Long-term stability of various carbon-nanotube-based micro-tip emitters.* Diamond and Related Materials, 2009. **18**(2-3): p. 486-489.
158. Zou, Y. May, P. W. Vieira, S. M. C. Fox, N. A., *Field emission from diamond-coated multiwalled carbon nanotube "teepee" structures.* Journal of Applied Physics, 2012. **112**(5).
159. Qu, Q. Y. Qiu, W. Q. Zeng, D. C. Liu, Z. W. Dai, M. J. Zhou, K. S., *Effects of deposition parameters on microstructure and thermal conductivity of diamond films deposited by DC arc plasma jet chemical vapor deposition.* Transactions of Nonferrous Metals Society of China, 2009. **19**(1): p. 131-137.
160. Chen, H. C. Sankaran, K. J. Lo, S. C. Lin, L. J. Tai, N. H. Lee, C. Y. Lin, I. N., *Using an Au interlayer to enhance electron field emission properties of ultrananocrystalline diamond films.* Journal of Applied Physics, 2012. **112**(10).
161. Sharma, H., A.K. Shukla, and V.D. Vankar, *Effect of titanium interlayer on the microstructure and electron emission characteristics of multiwalled carbon nanotubes.* Journal of Applied Physics, 2011. **110**(3).
162. Zhang, J. H. Yang, C. R. Yang, W. W. Feng, T. Wang, X. Liu, X. H., *Appearance of a knee on the Fowler-Nordheim plot of carbon nanotubes on a substrate.* Solid State Communications, 2006. **138**(1): p. 13-16.
163. Jo, H. Kim, S. Kim, H. Kim, J. Kim, M. H., *Nucleate boiling performance on nano/microstructures with different wetting surfaces.* Nanoscale Research Letters, 2012. **7**.
164. Patil, C.M. and S.G. Kandlikar, *Review of the manufacturing techniques for porous surfaces used in enhanced pool boiling.* Heat Transfer Engineering, 2014. **35**(10): p. 887-902.
165. Kim, P. Shi, L. Majumdar, A. McEuen, P. L., *Thermal transport measurements of individual multiwalled nanotubes.* Physical Review Letters, 2001. **87**(21).
166. Phan, H. T. Caney, N. Marty, P. Colasson, S. Gavillet, J., *Flow boiling of water on*

titanium and diamond-like carbon coated surfaces in a microchannel. Proceedings of the ASME International Heat Transfer Conference - 2010, Vol 1, 2010: p. 127-132.